

Resonant Spectroscopy on Strongly Correlated Materials

THÈSE N° 4087 (2008)

PRÉSENTÉE LE 12 JUIN 2008

À LA FACULTE SCIENCES DE BASE
LABORATOIRE DE SPECTROSCOPIE ÉLECTRONIQUE
PROGRAMME DOCTORAL EN PHYSIQUE

ÉCOLE POLYTECHNIQUE FÉDÉRALE DE LAUSANNE

POUR L'OBTENTION DU GRADE DE DOCTEUR ÈS SCIENCES

PAR

Xiaoqiang WANG

M.Eng in electrical and computer engineering, National University of Singapore
et de nationalité chinoise

acceptée sur proposition du jury:

Prof. R. Schaller, président du jury
Prof. M. Grioni, directeur de thèse
Prof. G. Ghiringhelli, rapporteur
Prof. H. Ronnow, rapporteur
Dr T. Schmitt, rapporteur



ÉCOLE POLYTECHNIQUE
FÉDÉRALE DE LAUSANNE

Suisse
2008

Abstract

All strongly correlated materials exhibit fascinating physical properties, like Mott insulator transitions, high temperature superconductivity, Kondo and heavy fermion behavior, colossal magnetoresistance, etc. These properties make them attractive for developing novel applications. To achieve this ambitious goal, the nature of the strong electronic correlations must be investigated. Soft x-ray resonant inelastic scattering (RIXS) and resonant inverse photoemission (RIPES) are precious in this context, because they provide detailed information on the fundamental low energy excitations.

The high resolution RIXS experiments which represent the main subject of the present thesis required a lot of experimental work for testing, commissioning and fine-tuning two very sophisticated instruments: the soft x-ray ADDRESS beamline at the Swiss Light Source (SLS) and its dedicated RIXS spectrometer SAXES. Thanks to this work, the design goal of reaching a world-record resolution better than 100 meV below 1k eV has been successfully achieved.

Chapter 3 and 4 present RIXS measurements of NiO, MnO, CuO and other cuprates performed both at the TM L_3 , O K edges. The unprecedented resolving power of SAXES allows us to accurately identify the local electronic excitations at the \sim eV scale as well as new low energy excitations at the \sim 100 meV scale, originated from the magnetic exchange interaction. Chapter 5 is devoted to the RIPES study of the isostructural Kondo systems CeX_9Si_4 ($X=\text{Ni,Co}$), and presents a possible explanation for the remarkable differences in the magnetic and transport properties of these two related compounds.

Abstract

Keywords: Strongly Correlated Materials, Resonant Inelastic X-ray Scattering (RIXS), Resonant Inverse Photoemission Spectroscopy (RIPES), Transition Metal Oxides, Cuprates, Kondo System, Mixed Valence

Résumé

Les systèmes à fortes corrélations électroniques présentent des propriétés physiques fascinantes, telles que la transition métal-isolant de Mott, la supraconductivité à haute température, le comportement Kondo ou de type fermion lourd, la magnéto-résistance géante etc. Ces propriétés les rendent intéressants en vue de possibles applications nouvelles. Pour atteindre ce but ambitieux, il est capital d'étudier la nature des fortes corrélations électroniques. La diffusion résonnante inélastique (RIXS) des rayons x mous, ainsi que la photoémission inverse résonnante (RIPES) sont extrêmement utiles dans ce contexte, puisqu'elle donnent des informations détaillées sur les excitations fondamentales de basse énergie.

Les expériences RIXS à très haute résolution qui forment la partie principale de cette thèse ont demandé un travail considérable de test, de commissioning et d'ajustement fin de deux instruments très sophistiqués: la ligne de lumière pour les rayons x mous ADDRESS de la Swiss Light Source (SLS), et le spectromètre SAXES réservé aux mesures RIXS. Grâce à ce travail, le but initial de pouvoir démontrer une résolution de 100 meV - ce qui constitue un record au niveau mondial - a été atteint.

Les Chapitres 3 et 4 présentent des mesures RIXS de NiO, MnO, CuO et autres cuprates effectuées aux seuils L_3 du métal de transitions ainsi qu'au seuil K de l'oxygène. La résolution très poussée de SAXES nous a permis de mettre en évidence avec précision les excitations électroniques locales à l'échelle de l'eV, mais aussi de nouvelles excitations d'origine magnétique à l'échelle de 100 meV. Le Chapitre 5 présente une étude RIPES des systèmes Kondo CeX_9Si_4 ($X=Ni,Co$), et propose une explication possible pour les différences remarquables des propriétés magnétiques et de transport de

Résumé

ces deux composés qui sont par ailleurs très proches.

Mots clefs: Matériaux à fortes corrélations électroniques, Diffusion Résonnante de Rayons x (RIXS), photoémission inverse résonnante (RIPES), Oxydes de métaux de transition, cuprates, valence intermédiaire

Acknowledgements

I am deeply indebted to my supervisor Prof. Marco Grioni for the possibility to join the international collaborations of SAXES and ADRESS projects, for his stimulating suggestions and encouragement that helped me in all the time of research and writing of this thesis.

Sono molto grato al Prof. Lucio Braicovich, al Prof. Giacomo Ghiringhelli e alla Prof. Claudia Dallera, da cui ho imparato molto, sia in materia di fisica che di tecniche sperimentali.

I owe many thanks to Andrea Piazzalunga: it is a great pleasure to work with him in various levels, mechanics mounting, commissioning SAXES spectrometer and ADRESS beamline, taking data, spectra analysis...

I further thank Dr. Luc Patthey who has made my stay in SLS comfortable. I want to thank Dr. Thorsten Schmitt, Dr. Vladimir Strocov and Dr. Thomas Schmidt, with whom I learned about undulators, beamline concepts and operations. I am thankful to Juraj Krempasky who helped me on various EPICS problems and introduced me to the control group.

I like very much the *short* and agreeable time with Dr. Daniela Pacilé, Marco Papagno, Dr. Mihaela Falub, Luca Moreschini, Slobodan Mitrovic, Dr. Christian Ast. And it was nice to see my *new* colleagues, Emmanouil Frantzeskakis, Peng Xu, Dr. Stéphane Pons out in workshops and meetings.

I enjoy the beam time with Federico Bottegoni, Marco Moretti, Dr. Gheorghe Sorin Chiuzbaian, Dr. Justina Schlappa, Dr. Azzodine Bendounan, having a lot of fun with *babyfoot* play.

I want to stress also the technique support provided by Gilles Grand-

Acknowledgements

jean, Pascal Cattin, Philippe Guex, Martial Doy, José Grandjean in Lausanne and Markus Kropf in Villigen. Thanks for their excellent technical works and tolerance of my poor English-only speaking.

I finally thank my wife to bear my absence of many weekends and nights. I thank my daughter having no complaints while living away from me for 7 months. And I am always grateful to my parents for their understanding and support from far beyond reach.

Contents

Abstract	i
Résumé	iii
Acknowledgements	v
Contents	vii
1 General information	1
1.1 Strong electronic correlations	1
1.1.1 Transition metal oxide	3
1.1.2 Kondo system	4
1.2 How do we study them?	7
1.3 Resonant inelastic x-ray scattering	8
1.3.1 Spectral function	9
1.4 Resonant inverse photoemission	10
1.4.1 Instruments	12
1.5 Theoretical model	14
1.6 Scope	15
2 SAXES and ADRESS	17
2.1 SAXES design basics	19
2.2 SAXES in details	22
2.3 ADRESS beamline	32
2.3.1 Synchrotron radiation	32
2.3.2 Fixed gap undulator	34

Contents

2.3.3	Optical layout	34
2.3.4	Performance	36
2.3.5	Refocusing and spot size	37
2.4	Control system	39
3	High resolution RIXS of NiO	43
3.1	Ni L_3 edge	43
3.1.1	dd excitations	44
3.1.2	Local spin-flip	46
3.1.3	Crystal field model calculations	51
3.1.4	Angle dependence	53
3.2	O K edge	55
3.3	Ni $M_{2,3}$ edge	57
4	Mn and Cu compounds	63
4.1	MnO	63
4.2	CuO and malachite	66
4.3	BSCCO	69
4.3.1	Cu L_3 edge	70
4.3.2	O K edge	73
5	RIPES study of CeX_9Si_4 ($X=Ni,Co$)	79
6	Conclusion	85
	Bibliography	89
	Curriculum Vitae	95

Chapter 1

General information

1.1 Strong electronic correlations

Modern quantum theory of the electronic properties of solids is built on the paradigm of non-interacting, nearly-free particles moving in the periodic background of the positive ions of the lattice [1, 2]. This may appear quite surprising, if one considers that electrons are charged particles interacting with the positive ions and among themselves via the strong Coulomb force. Part of the answer to this paradox is provided by the theory of the pseudopotential [3], which shows that often the nearly-free electron potential is a very good approximation to the real electron's single-particle Hamiltonian. The justification for being able to "sweep under the rug" electron-electron interactions is much more subtle. It is based on the "Fermi liquid" concept introduced by Landau, who showed that it is possible to draw a one-to-one correspondence between a system of independent electrons - a Fermi gas - and the excitations of a real, interacting system, then dubbed a "Fermi liquid" [4, 5]. These *quasiparticle* excitations are complex objects, where an electron (or a hole) is dressed by the interactions with the other particles and with collective excitations (phonon, magnons, plasmons). Notice that the quasiparticles may actually be very different from the "naked" electrons: their masses, for instance, can be much larger than the bare electron's mass. This carries over to the ex-

perimentally observed renormalization of electronic properties like the low-temperature electronic specific heat or the magnetic susceptibility. Still, the complex can be identified by the same quantum numbers (wavevector k , spin) as the non-interacting electrons. Moreover, and most importantly, in many cases the quasiparticles interact only weakly with each other. Therefore, these properties justify the original idea of describing the solid as an assembly of nearly-free entities. This approach opens the way to many useful practical developments, like the Local Density Approximation (LDA) treatment of Density Functional Theory, which now routinely provides very accurate band structures of solids [6].

The assumption of nearly-free particles is strained to its limit - and beyond - in many novel materials of current interest, first and foremost in the high- T_c cuprates, but also in the colossal magnetoresistance manganites and more generally in many $3d$ transition metal oxides, in low-dimensional materials, and in the heavy-fermion and intermediate valence systems containing partially filled $4f$ electronic shells. In all these materials the effects of correlations yield physical properties that are more and more removed from those of a "normal metal". More dramatically, characteristic instabilities like superconductivity, charge- and spin-density waves, metal-insulator (Mott) transitions lead to completely different ground states [7, 8, 9, 10]. Here, the fundamental assumption of the Fermi liquid, i.e. the possibility of connecting adiabatically the ground states of the Fermi gas and of the interacting systems, breaks down. Understanding the nature of the correlated "normal" states, and of the broken-symmetry ground states is probably the major challenge in today's condensed matter physics. It is also a necessary step towards the future exploitation of these extraordinary properties through the design of new materials and of artificial structures with suitable physical properties or performing a specific function.

At a fundamental level, this ambitious goal requires a better understanding of the behavior of interacting electrons. Experimentally, this problem has been attacked by a wide range of solid state techniques. Unlike conventional thermodynamic, magnetic or transport experiments, high-

energy spectroscopies involve a perturbation which is much larger than $k_B T$ or any of the low-energy scales of the system. Nevertheless, the spectra bear information on all characteristic single-particle excitations, from the eV down to the meV scale, and the sudden decoupling of the emitted particles from the excited system enables a simple theoretical analysis of the experiment. High-energy spectroscopies are therefore gaining importance as powerful probes of the electronic structure of complex materials.

In this thesis I present original results obtained by performing *resonant* high-energy spectroscopy experiments on selected compounds which belong to two distinct and important families of strongly interacting materials: the transition metal oxides, and the intermediate-valence Kondo systems.

1.1.1 Transition metal oxide

Transition metal compounds - especially systems containing transition metals of the first row - exhibit a large variety of electronic and magnetic properties and, although they have been investigated over many decades, open questions related to their behavior still exist. At the origin of the complexity and richness of their behavior is the open $3d$ shell. These electrons participate in the formation of covalent bonds with ligand atoms, but are sufficiently localized to retain in part their atomic character. As a consequence a local approach - crystal field, ligand fields, Anderson impurity model - often is an appropriate starting point to understand the electronic structure. Atomic multiplet effects cannot in general be neglected, thus adding to the complexity of the problem.

From simple electron counting considerations these materials should be metals, due to the partially filled $3d$ orbitals. This prediction is clearly contradicted by the observation of insulating compounds, often with a large energy gap. A prototypical and much studied case is that of NiO, which is a transparent antiferromagnetic insulator with a gap exceeding 4 eV. Early attempts by Slater to attribute the insulating character to the AFM order proved to be incompatible with the large gap value, and even

modern band theory based on the LDA approach predicts a gap which is one order of magnitude too small. It was Verwey and Mott who first realized that a strong on-site Coulomb interaction among the $3d$ electrons would strongly suppress charge fluctuations (the "electrons stay at home"). The resulting energy gap then does not have a band character, but is intrinsically determined by correlations. The complex competition of translational bandwidth and (screened) electron-electron interaction is ubiquitous in these systems, and in particular is responsible for the dramatic metal to insulator transitions as a function of temperature, pressure or stoichiometry observed in oxides materials like V_2O_3 .

Transition metal oxides are very much at the focus of attention of physicists, chemists and materials scientists, especially after the discovery of high temperature superconductivity in some layered cuprates. More recently, the colossal magnetoresistance manganites, and the *multiferroic* systems, where electrical and magnetic order parameters can be mutually controlled, have raised enormous interest. The past two decades have witnessed the accumulation of an enormous quantity of experimental results on their electronic properties, and the development of a general theoretical paradigm [11]. High energy spectroscopies have played and continue to play an important role in clarifying the complex interplay of the charge, spin, orbital degrees of freedom of these materials [12]. Some of these aspects will emerge in the following chapters, where the electronic structure of selected strongly correlated materials are probed in an original way by novel spectroscopic techniques.

1.1.2 Kondo system

Another family of materials exhibiting clear signatures of strong correlations is that of the intermediate-valence Kondo systems. Most of these materials are intermetallics containing lanthanide ions, typically Ce and Yb, or uranium. Their physical properties are the result of a competition between strong Coulomb correlations, which tend to localize the partially filled Ce, Yb $4f$ orbitals, and hybridization with the extended conduction

band states.

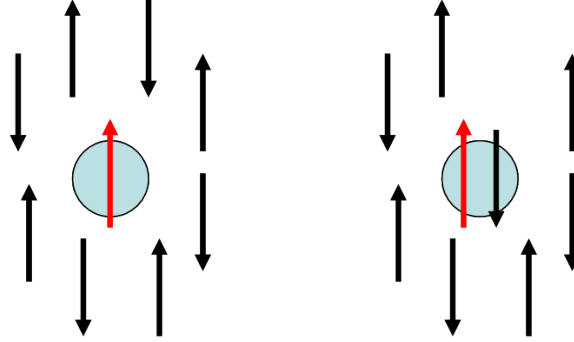


Figure 1.1: Illustration of the Kondo effect. Left panel: at high temperature, the impurity ion (solid circle with red arrow), acts as a strong magnetic scatterer immersed into fermi sea (black arrows). Right panel: at low temperature, the strong interaction between impurity and host electrons forms a singlet state, reducing magnetic scattering and forming a heavy-fermion liquid.

The consequence of this competition is the Kondo effect and the associated complex transport and magnetic behavior. As illustrated in Figure 1.1, when a magnetic impurity (red arrow) is embedded in a Fermi liquid (quasi-particles represented by black arrows), it acts at high temperatures like a strong magnetic scatterer. At low temperatures, a spin singlet state forms with quasi-particles from the Fermi sea. The resulting state is a "heavy Fermi liquid"—a state that obeys Landau's theory, but with a quasi-particle effective mass which - in special cases - may reach up to a thousand times that of the bare electron. The essential features of the complex Kondo behavior are captured by a simple theoretical model, the Anderson impurity model (AIM) [Anderson; see below]. According to the AIM, a single energy scale $\delta = k_B T_K$, exponentially dependent on the $4f$ -band hybridization strength, controls all the low-energy properties. The Kondo temperature T_K marks the crossover from the high-temperature local magnetic moments, to the low-temperature singlet phase.

One well studied case is the peculiar isostructural $\gamma \rightarrow \alpha$ phase transition in cerium metal at a pressure of 8 kbar, accompanied by a huge 17% volume collapse. The magnetic properties are remarkably different in

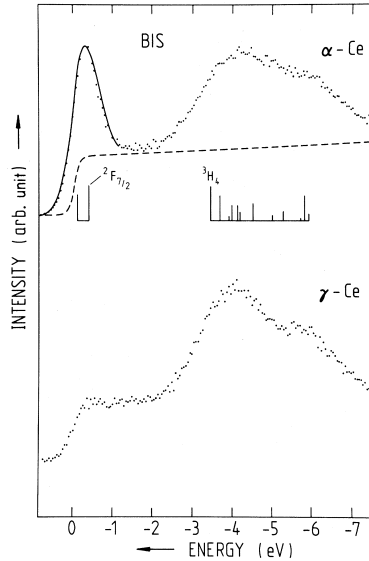


Figure 1.2: Inverse photoemission spectra (BIS) of α - and γ -Ce [13].

these two phases. The γ phase Ce exhibits a magnetic susceptibility following the Curie-Weiss law, where the Ce ion behaves like a local $S=1/2$ impurity with the atomic $^2F_{5/2}$ configuration. The α phase Ce shows no local moments and a temperature-independent Pauli magnetic susceptibility. This transition has been interpreted in terms of a 'Kondo' Ce impurity scenario, where the hybridization between the $4f$ electron and the conduction band - and therefore the Kondo temperature - is assumed to vary with volume between the γ and α phases. $k_B T_k$ increase rapidly (exponentially) with decreasing volume, and therefore drives the volume collapse in α phase. In this scenario, the larger hybridization in the low-T phase is accompanied by a reduction (from ~ 0.95 to ~ 0.7) of the $4f$ occupancy n_f .

This $4f$ electron occupancy variation has been observed by many spectroscopic methods [14, 15]. The clearest spectroscopic fingerprint was obtained by inverse photoemission (IPES) [13] which measures the electron addition spectrum from the hybrid ground state. In Figure 1.2, the sharp structure just above the Fermi level - the so-called Kondo resonance (KR) - is attributed to a $4f^1$ final state, while the higher-lying structure reflects a final state $4f^2$ multiplet. The sharp KR is a many-body feature which

represents a large renormalized density of $4f$ excitations involved in the unusual "Kondo" behavior. Its intensity is related to the $4f^0$ character present in the hybrid ground state. As a consequence, IPES probes the quantity $(1 - n_f)$, which varies greatly at the transition [16]. Indeed the intensity of the KR is much larger in the α phase, reflecting a larger $4f^0$ character in the ground state, and a larger hybridization strength.

1.2 How do we study them?

These systems can be studied by many experimental methods, measuring electronic and magnetic properties, across phase transitions. But the more powerful and direct probes are spectroscopic probes, which directly probe the excitation spectrum. Excitations in solids are fundamental to describe physical properties, such as the response to external perturbations and temperature dependence. Spin excitations are the domain of inelastic neutron scattering which can determine with high accuracy their energy-momentum relations. By contrast, charge excitations have been traditionally investigated by measuring the optical conductivity. However, optical transitions in the infra-red or visible range are restricted to a momentum transfer nearly equal to zero. A popular alternative spectroscopic technique, electron energy loss spectroscopy, can detect the momentum dependence of charge excitations, but it suffers from strong multiple scattering effects.

In this thesis, I concentrate on spectroscopic tools with the following characteristic features:

1. the excitation energy lies in the soft x-ray energy range. This includes the $3d$ transition metal $L_{2,3}$ edges and the rare earth $M_{4,5}$ edges.
2. they involve the excitation of core levels, and therefore acquire a large chemical selectivity.
3. the system is resonantly excited, yielding a strong resonant enhancement of the cross section when the excitation energy is varied across

the excitation threshold.

Depending on the types of incoming and outgoing particles, either photons or electrons, there are three types of resonant spectroscopies:

1. resonant photoemission, photon in - electron out.
2. resonant inverse photoemission (RIPES), electron in - photon out.
3. resonant x-ray emission (RXES), photon in - photon out.

In the present work only resonant inverse photoemission and resonant x-ray emission have been used, and will be considered further. The experimental details and their capabilities will be presented in the following.

1.3 Resonant inelastic x-ray scattering

In a resonant inelastic x-ray scattering (RIXS) process, a core electron is excited to the valence shell by absorbing an incident X-ray photon, and then the excited state radioactively decays by emitting an X-ray photon, see Figure 1.3. This process is described by a coherent second order process. By contrast X-ray photoemission (XPS) and X-ray absorption (XAS) spectra are first order processes which only involve a single photon. One can distinguish two different regimes, with different properties, as a function of the excitation energy. Emission following the excitation of a core electron into the continuum of final states, is usually referred to as normal x-ray emission (NXES). By contrast, when the core state is excited either into a discrete final state or at the threshold of a continuum, the process is dubbed resonant x-ray emission (RXES).

RIXS is a photon in and photon out process, and its probing depth is clearly determined by the penetration depth of the incoming and outgoing photons. At soft x-ray energies in the energy range of 400-1600 eV the resulting probing depth is relatively large (~ 100 nm) compared to electron spectroscopies like photoemission. Therefore RIXS provides bulk information in contrast to XPS and RIPES. Moreover, unlike electron spectroscopies, RIXS can be applied to study materials under magnetic field.

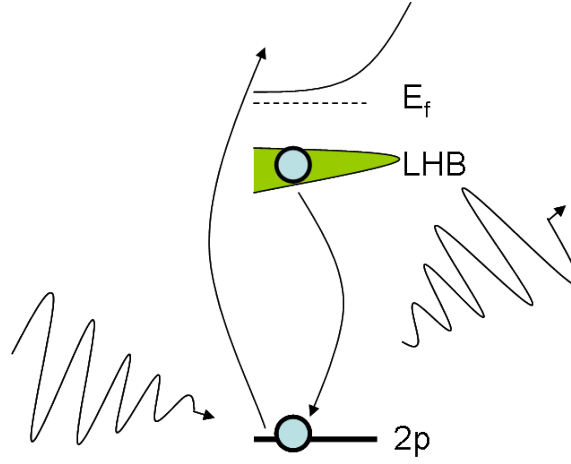


Figure 1.3: RIXS process in a single electron diagram.

1.3.1 Spectral function

Theoretically this second order coherent process is described by the Kramers-Heisenberg formula,

$$I(h\nu_{in}, h\nu_{out}) = \sum_f \left| \sum_i \frac{\langle f | T_e | i \rangle \langle i | T_a | g \rangle}{E_g + h\nu_{in} - E_i - i\Gamma_i} \right|^2 \times \delta(E_g + h\nu_{in} - E_f - h\nu_{out}) \quad (1.1)$$

where $|g\rangle, |i\rangle, |f\rangle$ refer ground, intermediate and final states respectively, and E_g, E_i and E_f are their corresponding energies. Γ_i is the core hole life broadening in the intermediate state. T_a and T_e represent the absorption and emission operators. In the soft x-ray region, the transition is governed by electron dipole transitions and quadrupole transitions which may be important in the hard x-ray region are negligible here. The two steps are not treated as independent because of the resonance condition expressed by the denominator giving the Lorentzian lineshape. The sum is coherent over the intermediate states and the lifetime broadening is not observed.

The resonance may provide a path which would be prohibited in the direct transition from $|g\rangle$ to $|f\rangle$. For example, in the soft x-ray region the excitation and emission processes are dipole transition, since the photon energy is too low to give a quadrupolar contribution. In such a case, with

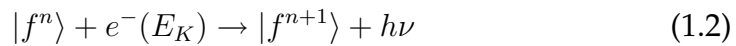
two successive dipole transitions one can reach a final state $|f\rangle$ which cannot be reached directly from $|g\rangle$ via dipole transition. dd excitations in transition metal or ff transitions in rare earth compounds are typical examples of this.

Energy conservation is enforced by Dirac delta function, $h\nu_{in} - h\nu_{out} = E_f - E_g$. When $h\nu_{in} - h\nu_{out} = E_f - E_g = 0$ the scattering is elastic and the final state $|f\rangle$ is the same as ground state $|g\rangle$, otherwise it is inelastic scattering. Both differences express the energy transferred to the solid. Because of the Lorentzian lineshape associated with the intermediate core-hole lifetime, the emission process takes place also for incident energy below the resonance threshold.

1.4 Resonant inverse photoemission

Inverse photoemission spectroscopy (IPES) is an electron in - photon out technique. It has been an important technique to investigate the unoccupied density of states in solids, giving complementary information to the more traditional and widespread photoemission spectroscopy about the DOS of materials. IPES has been performed according to two experimental schemes: the Bremsstrahlung isochromat spectroscopy (BIS) mode and tunable photon energy (TPE) or spectroscopy mode. In BIS mode, the excitation energy is scanned and the emitted photons are detected at a fixed energy by using a band-pass filter realized by a crystal Bragg monochromator in the x-ray region, or by an iodine-filled Geiger-Müller detector, for the UV. In the technically more challenging spectroscopy mode, a spectrograph is used to record the entire emitted photon spectra for a given primary excitation energy. Schematic pictures of the two modes are shown in Fig. 1.4,

IPES probes the electron addition spectrum of a solid. For a rare earth ion with n electrons in the $4f$ shell, the normal $4f$ addition process is, schematically:



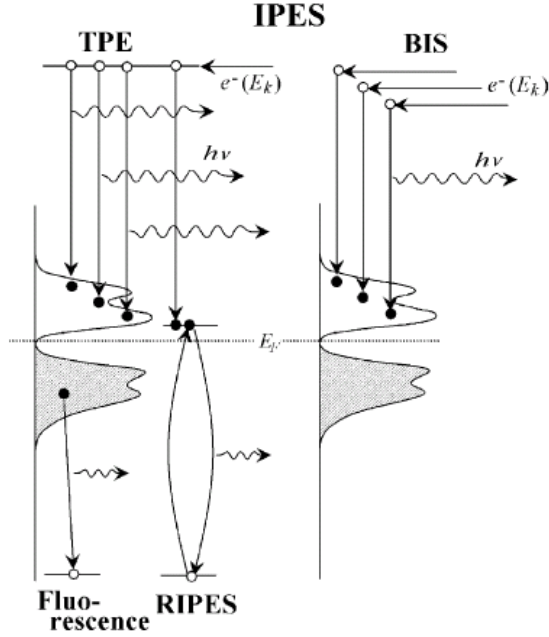


Figure 1.4: Energy diagram of IPES [17]. At low energy excitation, only IPES process is observed. If the excitation is higher than absorption edge, core hole is created. The core hole decays with fluorescence. Near absorption edge, RIPES process can take place.

where e^- denotes an incoming electron with kinetic energy E_K . Here the electron is captured by the ion and falls in the f shell with the emission of a photon of energy equal to the electron's kinetic energy. If the primary electron energy exceeds the binding energy of a core state, e.g. the $3d$ state of Ce at ~ 880 eV, the core electron can be excited into a discrete final state or into the continuum. The highly excited core hole state will then decay radioactively (fluorescence process) or non-radioactively (Auger process). At the threshold, for a $3d \rightarrow 4f$ transition in a rare earth, the second order process excitation-deexcitation process will take place as following,

$$|f^n\rangle + e^- \rightarrow |c f^{n+2}\rangle \rightarrow |f^{n+1}\rangle + h\nu \quad (1.3)$$

where c denotes a $3d$ core hole. It is the time-reversed process of Auger emission. The direct and indirect IPES processes have the same initial and

final states, and therefore can interfere in a quantum-mechanical sense, i.e. their probability amplitudes, rather than their intensities are coherently added. As a result, a large resonant enhancement of the IPES cross section as resonance effect is observed.

The concept of resonant IPES, or RIPES mechanism had already been proposed in the 70's by pioneering works [18, 19, 20]. However, only two decades later the process was exploited as a spectroscopic technique by Weibel and coworkers [21, 22] who developed a RIPES spectrometer of novel design. They performed resonant IPES (RIPES) near the Ce $3d$ (M_5) absorption edge (about 880 eV) in Ce-based Kondo systems and reported a strong resonance effect and a clear dependence of the spectral function on the Kondo temperature. Afterwards, Kanai *et al* succeeded in observing resonant IPES at the Ce $4d$ ($N_{4,5}$) edge (about 120 eV) with a grating spectrometer [23]. While at $N_{4,5}$ edge, the on-resonance intensity does not show a strong enhancement as at M_5 edge. Moreover the cross-section is rather low, making the observation of RIPES rather difficult. On the other hand, the extracted information about $4f$ electronic states are rather complementary in both edges.

1.4.1 Instruments

In inverse photoemission the excitation source is an electron gun which is operated under very strict conditions, due to the requirements of energy and current stability. Moreover, the thermal energy spread of the primary electron beam contributes largely to the overall resolution. In order to minimize this contribution, modern IPES guns utilize BaO cathodes with a very low work function which provides a sufficient thermionic emission at low temperatures of the order of 700 °C. Moreover the cathode is indirectly heated to avoid any ohmic drop which would broaden the energy distribution of the thermoelectrons. In normal operating conditions, the thermal spread is $\sim 0.2-0.3$ eV.

The energy of the emitted photons is analyzed by a spectrometer for sequential detection, or by a spectrograph for parallel acquisition . At the

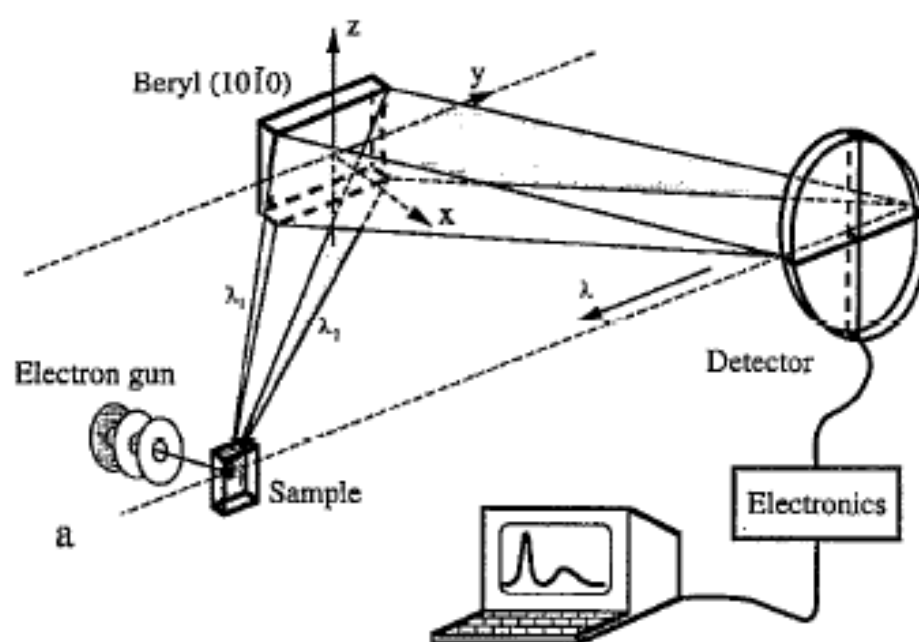


Figure 1.5: General layout of RIPES equipment.

rare earth $N_{4,5}$ edge the energy analysis is necessarily performed by a grating spectrometer, [24]. At the $M_{4,5}$ edge, on the other hand, a Bragg crystal spectrometer can be used. In our experimental setup, described in [21] a Beryl ($10\bar{1}0$) crystal is used. The experiment setup is shown as diagram in Figure 1.5. The instrument control and acquisition software had been originally written in Pascal for a now obsolete platform. It was therefore completely re-written during my thesis using LabVIEW [25], to provide a direct control of all interfaces to the spectrometer's motors, and to the acquisition detector's counters.

One important aspect of RIPES, and in principle of all spectroscopies involving electrons, is its surface sensitivity. The probing depth is limited by the mean free path of the incoming electrons, a few atomic layers normally. What makes the situation worse is that the high energy electrons accelerate the deterioration/contamination of the surface layer. This requires the *in situ* periodic regeneration of the surface, with intervals of the order of one hour or less in our ultra-high-vacuum conditions for reactive surfaces like those of the Ce compounds. This operation was achieved by in-situ scraping with a diamond file.

1.5 Theoretical model

The Anderson impurity model (AIM) introduced above, is also widely used to interpret core level spectroscopies of systems with partially localized electrons like the $3d$ electrons of $3d$ transition metals or the $4f$ electrons of the Ce and Yb Kondo systems. It was originally proposed by Anderson [26] to account for the existence of magnetic moment of a $3d$ transition element impurity in nonmagnetic host metals. Its successful application to core level spectroscopy was later developed by several groups in parallel [27, 28, 29].

This model considers a single atom with open d or f shells, and at the same time the other itinerate electrons in the conduction band are taken into account. The Hamiltonian of the model is varied between the specific methods used, but conceptually can be written as, for transition metal $3d$

states for instance,

$$H = H^{host} + H^{imp} + H^{hybr} \quad (1.4)$$

$$H^{host} = \sum_{k\sigma} \epsilon_k a_{k\sigma}^\dagger a_{k\sigma} \quad (1.5)$$

$$H^{imp} = \epsilon_d \sum_{\sigma} d_{\sigma}^\dagger d_{\sigma} + U_{dd} \sum_{\sigma > \sigma'} d_{\sigma}^\dagger d_{\sigma} d_{\sigma'}^\dagger d_{\sigma'} - U_{dc} \sum_{\sigma} d_{\sigma}^\dagger d_{\sigma} (1 - c^\dagger c) \quad (1.6)$$

$$H^{hybr} = V \sum_{k\sigma} (d_{\sigma}^\dagger a_{k\sigma} + a_{k\sigma}^\dagger d_{\sigma}) \quad (1.7)$$

where ϵ_k, ϵ_d are the one-electron energies of valence band and transition metal $3d$ level, respectively. The index k denotes the energy levels in the valence band and σ the indices for $3d$ state quantum numbers. The interaction term, V, U_{dc}, U_{dd} are the hybridization between $3d$ and valence band states, the core hole potential felt by $3d$ electrons, and the Coulomb repulsion between $3d$ electrons respectively. Thus d_{σ}^\dagger is a creation operator of the impurity $3d$ orbital with quantum number σ and $a_{k\sigma}^\dagger$ is a creation operator of a conduction electron of the host metal with wave number k and corresponding quantum number σ .

The ground state of this Hamiltonian is, due to the hybridization, the superposition of states with different electronic configurations. Of course, the complexity of the calculation rapidly grows with the number of configurations, and rapidly becomes unmanageable. A typical minimal set [28] is $d^n, d^{n+1}\underline{L}, d^{n+2}\underline{L}^2$, where \underline{L} denotes a ligand hole in the valence band, see Figure 1.6. The parameters entering the calculation are V, U_{dd}, U_{dc} and the charge transfer energy, $\Delta = E(d^{n+1}\underline{L}) - E(d^n)$.

1.6 Scope

The motivation of this thesis is to investigate the strong electronic correlation exhibited in transition metal compounds and Ce based Kondo systems by resonant spectroscopic methods.

This work was performed by taking advantage of two unique instruments. The Resonant Inelastic x-ray Scattering (RIXS) experiments were

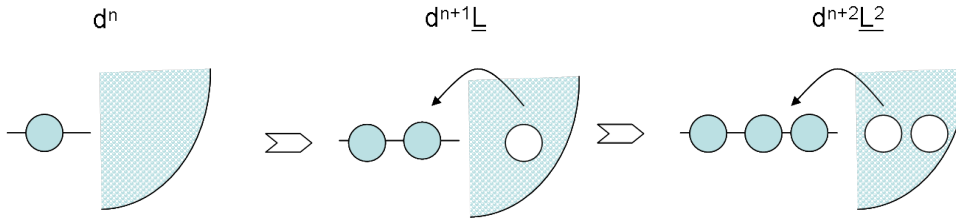


Figure 1.6: Schematic explanation of $3d$ electron and ligand valence hybridization, showing a case of $n=1$. In each part, the conduction states are on the right and $3d$ level to the left.

performed at the SAXES dedicated end station of the ADRESS beamline of the Swiss Light Source (SLS). During the past two years I have been directly involved in the test, commissioning and fine-tuning of this sophisticated instrument, which is the result of an international collaboration between the spectroscopy group of Politecnico di Milano, the SLS and EPFL. For the Resonant Inverse Photoemission (RIPES) measurements I have utilized a dispersive Bragg spectrometer developed by Weibel et al [21] and now installed at IPN-EPFL.

The thesis work develops along three main lines of research, i) design, construction and commissioning of the high resolution SAXES RIXS instrument at the SLS ADRESS beamline; ii) experimental work at the SAXES facility; iii) RIPES experiment on mixed valence compounds. Chapter 2 will elaborate the optical design and performance test of the SAXES spectrometer and ADRESS beamline. Chapter 3 presents the study of the prototypical strongly correlated transition metal oxide NiO by means of complementary RIXS experiments performed both at the L_3 and $M_{2,3}$ edges. In chapter 4, we explore a range of compounds with different d shell occupancy and crystal structures. Chapter 5 is devoted to the RIPES study of the Kondo systems CeX_9Si_4 ($X=Ni,Co$), and presents a possible explanation for the remarkable differences in the magnetic and transport properties of these two related compounds.

Chapter 2

SAXES and ADDRESS

The availability of third generation synchrotron radiation sources is giving access to unprecedented energy resolution in photon-based spectroscopies, namely in inelastic x-ray scattering spectroscopy. The progress of x-ray sources has to be accompanied by consistent advancements of the instrumentation, in order to maximize the future impact of these techniques onto physics, chemistry, and materials sciences. In this context the soft x-ray range is of particular importance for resonant spectroscopies due to the presence of the absorption edges of silicon, carbon, nitrogen, oxygen, $3d$ transition metals, and lanthanides. Particularly x-ray emission spectroscopy (XES) and resonant inelastic x-ray scattering (RIXS) can benefit from the strong resonant enhancements at the O K edge, $3d$ TM $L_{2,3}$ edges, and rare earth $M_{4,5}$ edges in the 400 to 1600 eV range. These experiments require a synchrotron radiation beamline delivering a highly monochromatic x-ray beam onto a small area of the sample and a high-resolution spectrometer capable of measuring the emission spectrum, at fixed incident photon energy, usually with a parallel acquisition over a convenient energy window. Considerable efforts have to be devoted to the improvement of spectrometer performances in terms of energy resolving power and detection efficiency.

In this field an important project is based at the Swiss Light Source (SLS) where a new beamline called ADDRESS (ADvanced RESonant Spec-



Figure 2.1: Photo of SAXES spectrometer installed at SLS ADRESS beamline.

troscopies) has been commissioned to be dedicated particularly to RIXS and to high energy angular resolved photoemission in the 400 to 1600 eV energy range. In RIXS the goals of having very high energy resolution and of exploring the scattering angle dependence have been achieved by the SAXES (Super Advanced X-ray Emission Spectrometer) instrument. This is a collaborated work between Politecnico di Milano, Ecole Polytechnique Fédérale de Lausanne and Swiss Light Source. This project started in 2003 and after 3 years of design, construction, and commissioning, it has produced the first results, which show a considerable improved energy resolution over all existing RIXS spectrometer operated at synchrotron radiation laboratories. Figure 2.1 shows SAXES is installed at the ADRESS beamline. In this chapter, I will highlight the design goal and characteristic performance of SAXES and ADRESS.

2.1 SAXES design basics

The design of the SAXES spectrometer is based on a single optical element, an advanced spherical variable line spacing (VLS) diffraction grating. The groove density(a) of the grating is not constant, instead it has a high order of dependence over local position w along the light propagation direction ($a(w) = a_0 + a_1w + a_2w^2$). This option was chosen for its simplicity, the desire to reduce reflection losses, and the possibility to minimize high order aberrations. As shown in detail in the appendix [30], this design offers a great flexibility of operation and, in principle, presents a large parameter space. Nonetheless, some of the parameter values are predetermined by external requirements or technological limitations such as source size ($S_1=8 \mu\text{m}$), spacial resolution($S_2=28 \mu\text{m}$), grating groove density($a_0=3200 \text{mm}^{-1}$), maximum platform length ($L=5\text{m}$), and energy range (400-1600 eV). Thus the only really free parameter is the included angle of scattering $2\theta_0$ after the decision to optimize the performance at energy 900 eV, which emphasize the importance of high T_c superconducting cuprates. This parameter determines the incidence angle α on the grating, which can not be lower than $\sim 88^\circ$. This lower limit is set in part by the reflectivity of the platinum coating of the grating. At smaller angles the efficiency starts to drop also because of other effects like the shadowing of the incoming beam by the grating's grooves.

θ_0	α	r_1	R	a_1	a_2
86.00	87.81	1111	51	0.874	-1.85×10^{-4}
86.15	88.03	1033	55	0.888	-1.77×10^{-4}
86.30	88.26	947	61	0.903	-1.70×10^{-4}
86.45	88.49	850	67	0.920	-1.63×10^{-4}
86.55	88.65	779	73	0.932	-1.58×10^{-4}

Table 2.1: Initial parameters. r_1 is the entrance arm, and R is the radius of grating surface curvature.

Based on this consideration, we choose three possible values of θ_0 and tabulate the calculated values of the other parameters in Table 2.1. By

requiring incident angle $\alpha > 88^\circ$, we choose the case where $\theta_0 = 86.30^\circ$ to do the optimization.

Extensive ray tracing was performed to verify the analytical results, using the SHADOW program [31]. The source is simulated by a $100 \times 10 \mu\text{m}^2$ rectangular source with a vertical divergence of 2 mrad. The result of a simulation for photons of two close energies, 900 and 900.08 eV is shown in Figure 2.2. The two energy lines are clearly separated on the detector.

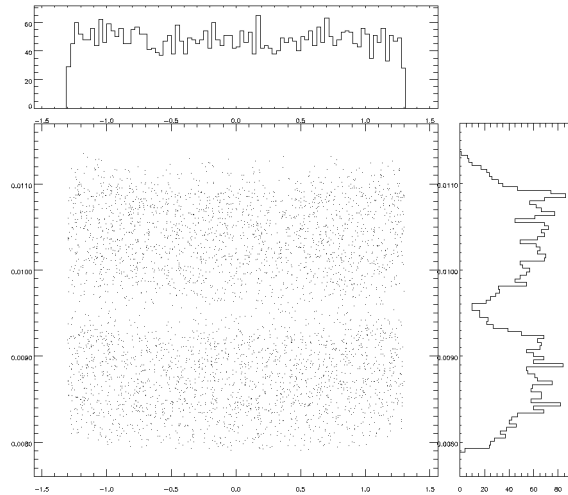


Figure 2.2: Ray tracing result for two photon energies 900 and 900.8 eV.

An important parameter of the VLS grating is a_2 , which is essential to cancel the coma aberration. To illustrate the coma effect, ray tracing is done by recording spectra diffracted from different parts of the grating. In Figure 2.3a, the spectrum from the center part (black) of the grating has the best line shape, and the other two have tails coming out from the left side. This calculation shows that the footprint would have to be reduced to 1/3 of the grating active area to prevent a loss of resolution, but at the expense of a corresponding flux reduction. To cancel this effect, the value of a_2 must be optimized based on the analytical results by ray tracing. In Figure 2.3b, the three spectra fulfill the criteria to cancel the coma and are superimposed.

The performance has been tested experimentally with the K_α fluorescence emission line of Al and Mg, 1486.7 and 1253.7 eV respectively, gen-

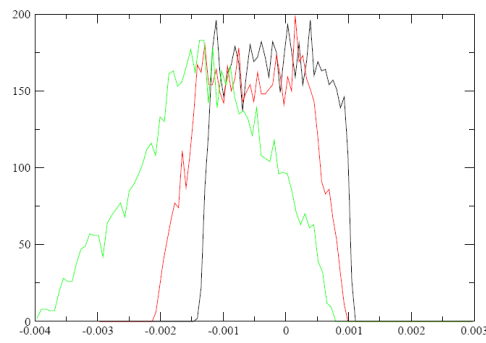
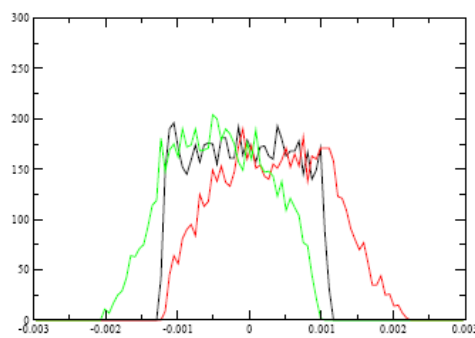
(a) Without a_2 correction(b) Optimum a_2 correction

Figure 2.3: The effect of a_2 . The black spectrum is diffraction from the central part of the grating, while the red and green are from the near and far ends respectively.

erated from a conventional x-ray tube. This test is crucial because it gives a measurement of the SAXES resolution that is independent of the beamline performance. Because these lines are at the upper limit of SAXES operation, these tests are really severe and crucial. Using the tabulated reference values of the - partially resolved - spin-orbit split Al $K_{\alpha 1}$ and $K_{\alpha 2}$ components [32], it was possible to estimate a resolving power exceeding 7000 at 1486 eV. For Mg the spin-orbit separation is smaller, and cannot be resolved, and the lineshape asymmetry was used as the main criterium as illustrated in Figure 2.4. From the comparison, a resolving power is deduced as 10,000 without much ambiguity.

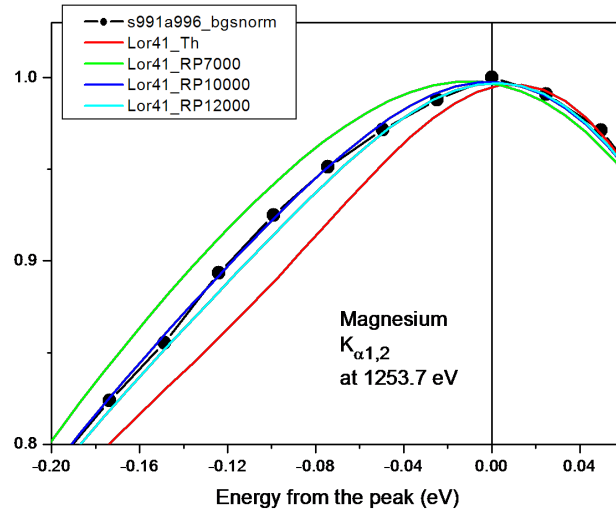


Figure 2.4: Mg K_{α} spectra (solid circles) compared with simulated spectra of different resolving power, obtained by a Gaussian broadening of the ideal spectrum (red).

2.2 SAXES in details

In this section, the SAXES spectrometer has been elaborated from the following aspects: optics concepts, parameters choices, expected resolution, components descriptions, and performance tests, providing technical insights of this sophisticated instrument. In summary the targeted resolving power has been reached independently and further beamline matching would make it a unique tool for studying strong electron correlation.

SAXES, a high resolution spectrometer for resonant x-ray emission in the 400–1600 eV energy range

G. Ghiringhelli, A. Piazzalunga, C. Dallera, G. Trezzi, and L. Braicovich
Dipartimento di Fisica, Politecnico di Milano, Piazza Leonardo da Vinci 32, I-20133 Milano, Italy

T. Schmitt, V. N. Strocov, R. Betemps, and L. Patthey
Swiss Light Source, Paul Scherrer Institut, CH-5232 Villigen PSI, Switzerland

X. Wang and M. Grioni
Institut de Physique des Nanostructures, Ecole Polytechnique Fédérale de Lausanne, CH-1015 Lausanne, Switzerland

(Received 26 July 2006; accepted 2 October 2006; published online 14 November 2006)

We present a 5 m long spectrometer for soft x rays to be used at a synchrotron radiation beamline for resonant x-ray emission spectroscopy and resonant inelastic x-ray scattering in the 400–1600 eV energy range. It is based on a variable line spacing spherical grating (average groove density of 3200 mm^{-1} , $R=58.55 \text{ m}$) and a charge coupled device two dimensional detector. With an x-ray spot on the sample of $10 \mu\text{m}$, the targeted resolving power is higher than 10 000 at all energies below 1100 eV and better than 7000 at 1500 eV. The off-line tests made with Al and Mg $K\alpha_{1,2}$ fluorescence emissions indicate that the spectrometer can actually work at 12 000 and 17 000 resolving power at the L_3 edges of Cu (930 eV) and of Ti (470 eV), respectively. SAXES (superadvanced x-ray emission spectrometer) is mounted on a rotating platform allowing to vary the scattering angle from 25° to 130° . The spectrometer will be operational at the ADDRESS (advanced resonant spectroscopies) beamline of the Swiss Light Source from 2007. © 2006 American Institute of Physics. [DOI: 10.1063/1.2372731]

I. INTRODUCTION

The availability of third generation synchrotron radiation sources and of even better sources in the coming years (diffraction limited storage rings and free electron lasers) is opening the access to unprecedented energy resolution in inelastic x-ray scattering spectroscopy. The progress of x-ray sources has to be accompanied by consistent advancements of the instrumentation, in order to maximize the future impact of these techniques onto physics, chemistry, and materials sciences. In this context the soft x-ray range (below $\sim 1700 \text{ eV}$ photon energy) is of particular importance for resonant spectroscopies due to the presence of absorption edges of silicon, carbon, nitrogen, oxygen, $3d$ transition metals ($3d\text{TMs}$), and lanthanides. Moreover x-ray emission spectroscopy (XES) and resonant inelastic x-ray scattering (RIXS) can benefit from the particularly strong resonant enhancements at the O K edge, $3d\text{TM}$ $L_{2,3}$ edges, and rare earth $M_{4,5}$ edges in the 400–1600 eV range.^{1–3} These experiments require a synchrotron radiation beamline delivering a highly monochromatic x-ray beam onto a small area of the sample and a spectrometer capable of measuring the emission spectrum, at fixed incident photon energy, usually with a parallel acquisition over a convenient energy window. Considerable efforts have to be devoted to the improvement of spectrometer performances in terms of energy resolving power and detection efficiency. In fact, at these energies the scattering cross sections are always very small and the signal is further reduced by the necessity of using grazing incidence gratings in the spectrometers, which drastically reduce the instrument

angular acceptance. After the pioneering works by Callcott *et al.*⁴ and by Nordgren *et al.*⁵ whose instrument, also commercially available, has been widely used in these years, other groups have developed spectrometers following a similar layout.^{6–11} The effort for getting narrower spectral linewidth (LW) has been pursued both in the very soft x-ray range (typically up to 100 eV covering the M edges of the $3d\text{TMs}$) and at higher energies (e.g., the L edges of $3d\text{TMs}$ and the $M_{4,5}$ resonances of lanthanides from about 450 to 1600 eV) where the goal is more difficult: a ten times higher resolving power is required to get the same linewidth. On the other hand L edges usually have stronger resonances and better defined intermediate states in the scattering process, and interesting perspectives are given by the scattering angle dependence: the photon momentum is not negligible and the transferred momentum versus transferred energy behavior can be studied.

In this field an important project is based at the Swiss Light Source (SLS) where a new beamline called ADDRESS (advanced resonant spectroscopies) has been designed to be dedicated particularly to RIXS and to high energy angular resolved photoemission in the 400–1600 eV energy range. In RIXS the goals of achieving very high energy resolution and of exploring scattering angle dependence have required to jointly design the beamline and the spectrometer. In this article we present SAXES (superadvanced x-ray emission spectrometer), the high resolution instrument that is being installed at the ADDRESS beamline. SAXES has already been tested off line with conventional x-ray sources. We present

here its novelties with respect to previous instruments. The instrument is an evolution of AXES (advanced x-ray emission spectrometer),^{7,12} built by some of us and working since 1995 at the beamline ID08 of the ESRF in Grenoble.¹³ Our goal was now to reach 12 000 resolving power at the L_3 edge of Cu (930 eV), meaning ~ 80 meV LW, in consideration of the great importance of high T_c superconducting cuprates. More in general we targeted a resolving power higher than 10 000 over the whole energy range. With a beamline monochromator having roughly the same resolving power or slightly better, this would give a combined LW around 100 meV full width at half maximum (FWHM), i.e., considerably better than any published RIXS measurements at the Cu L_3 edge.^{14,15} As shown below the spectrometer has reached this goal. On the other side the beamline monochromator has been designed to reach 30 000 resolving power over the whole energy range.

One important experimental parameter in XES and RIXS is the signal intensity that has often limited the actual working resolution which had to be reduced in order to get sufficient statistical quality in the spectra. In our case when passing from AXES at the ESRF to SAXES at the SLS, we should obtain comparable intensities on the detector. In fact, the optical layout is very similar and a factor of about 3 should be lost because of the reduction of the horizontal angular acceptance due to the longer distance of the detector from the sample (5 m instead of 2.2 m). Another loss should come from the grating efficiency (higher groove density in SAXES than in AXES), partially compensated by a better quality of the groove profile in the new grating. On the other hand a gain should come from a much better optical matching between the beamline and the spectrometer and, at least at low energies, from higher intensity delivered by the ADDRESS beamline with respect to ID08. These estimates make us confident about the actual feasibility of the high resolution RIXS spectra using SAXES at the ADDRESS beamline.

II. THE OPTICS OF SAXES

A. Concepts on the layout

Up to now the spectrometers for XES and RIXS in the soft x-ray range, where Bragg crystals cannot be employed, have been designed according to two schemes. Some systems are based on one single optical element, a grazing incidence concave diffraction grating dispersing and focusing the radiation onto a position sensitive detector to be positioned in the appropriate place depending on the energy of the spectrum. Other systems combine a concave mirror with a plane grating in order to separate the dispersion and focusing actions. The latter should provide greater angular acceptance (typically a factor of 2–3), but it is obviously more complicated to build and to operate.

In our project we opted for the single optical element scheme. This choice was done not only to privilege simplicity but also to have a system where the minimization of all the higher order optical aberrations is easily obtained over the whole energy range. When using variable line spacing (VLS) gratings with fixed radius of curvature and fixed po-

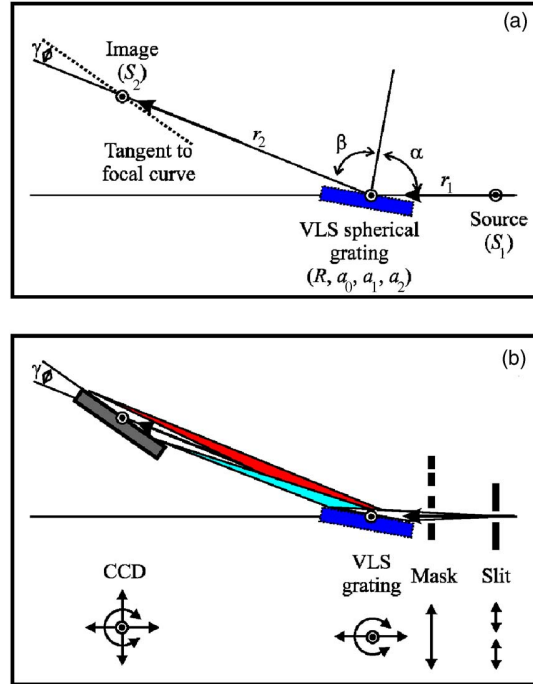


FIG. 1. (Color online) The schematic layout of the SAXES spectrometer, which is based on a VLS spherical grating and a two dimensional position sensitive CCD detector. Panel (A): the main optical parameter symbols are defined. Panel (B): the main mechanical components are sketched together with their degrees of freedom. The entrance slit width can be regulated with a $1 \mu\text{m}$ accuracy. The grating can be moved along the entrance arm and can be rotated to change r_1 and α , respectively. The CCD detector can be displaced to follow the focusing curve and can be rotated to change the incidence angle γ . A mask with a set of apertures of different vertical widths is placed just before the grating to allow a regulation of the illuminated footprint on the grating, in order to have a full control of optical aberrations.

sition, it is not possible to cancel the coma aberration at more than one energy. That is why in SAXES the grating can be repositioned (in terms of distance from the source and incidence angle) for minimizing the LW broadening due to the high order optical aberrations. The same procedure is possible also in the two optical element systems, but it seems to us more difficult to implement.

The layout of SAXES is shown in Fig. 1 (b) (schematic side view). Panel (A) shows the parameters to be considered in the optical design (entrance and exit arm lengths r_1 and r_2 , incidence and diffraction angles α and β , source size S_1 , detector effective spatial resolution S_2 , angle of glancing incidence on the focal curve around a given energy γ , and VLS grating parameters R, a_0, a_1 , and a_2). In panel (B) we show the main available degrees of freedom provided by our mechanics: the entrance slit width, the longitudinal grating position, the grating pitch angle, the vertical and horizontal detector positions, and its pitch angle. In addition a set of apertures in a vertically movable mask can be used to change the length of the grating illuminated area (in order to further control optical aberrations). For any photon energy the grating has to be put at the right position and angle; the first internal order diffracted beam can be collected by the detector located in the corresponding focal position and oriented to be tangential to the focal curve. Owing to the use of a two dimensional detector, a whole spectrum can then be recorded

in parallel, i.e., nothing needs to be scanned during the spectrum acquisition. The spectrometer is installed on a rotating girder platform, which provides additional degrees of freedom (roll, yaw, as well as transverse and vertical movements) essential for the alignment of the spectrometer to the sample and incident x-ray beam.

B. Choice of the parameters

The choice of the optical parameters is dictated by both optical and mechanical boundary conditions. As explained above the grating position and orientation have to be adjustable to allow the minimization of the optical aberrations. The minimum source size S_1 is given either by the width of the entrance slit or by the height of the illuminated spot on the sample: a good refocusing after the exit slit of the beamline is vital in order to maximize the detection efficiency even when using a very narrow entrance slit. Moreover, if the spot height is sufficiently small it will be possible, at least in some occasions, to use SAXES without input slit in order to get the maximum efficiency. A spot size down to $9\ \mu\text{m}$ (FWHM) should be feasible at the ADRESS beamline due to an ellipsoidal mirror refocusing with a theoretical demagnification of about 5.5. In the design we have assumed $S_1 = 5\text{--}10\ \mu\text{m}$. If in the future smaller sizes will be attained, this will increase mostly the luminosity and only to some extent the resolution which will be in that case limited by the spatial resolution of the detector.

The spatial resolution of the charge couples device (CCD) detector determines the spectrometer virtual exit slit. Modern CCD detectors for soft x rays are back illuminated and thinned to reduce the surface dead layer; their detection efficiency is probably above 80% in our energy range. They are very user friendly and their effective spatial resolution is around $25\ \mu\text{m}$, irrespective of the pixel size, as a consequence of split events, as shown below. The only way to gain in spatial resolution is thus to mount the CCD at grazing incidence: in our case we chose $\gamma = 20^\circ$ (see Fig. 1 that is not to scale) so that the effective exit slit width is $S_2 = 8\text{--}9\ \mu\text{m}$, of the same order as S_1 . This means that, in the optimal layout, the magnification by the grating is around unity at the first order.

The optimal use of the CCD mounted at grazing incidence implies that the spectrum is dispersed on a focal locus well approximated by the surface of the CCD. The control of this parameter (the angle γ) is obtained through the appropriate choice of the VLS parameters as proposed by Osborn and Callcott in Ref. 16. One has also to fix the total length of the spectrometer: a longer instrument can reach higher resolving power but the horizontal angular acceptance, determined by the size of the detector, is then reduced. For SAXES we established a maximum length of around 5 m, i.e., more than two times the length of AXES at the ESRF; this is also the maximum space available for the end station at the ADRESS beamline. The loss in angular acceptance should be counterbalanced by a better optical matching between beamline and spectrometer, as well as by a larger photon flux of the ADRESS beamline. Another important consideration concerns the average ruling density and the VLS parameters. The present manufacturing technology allowed

us to safely reach $a_0 = 3200\ \text{mm}^{-1}$ and a maximum variation of the local density along the grating of 10%.

The actual optical design went first through a search for the first approximation parameters using the analytical expressions for VLS gratings,^{16–18} and then checked and optimized with ray tracing using the SHADOW code.¹⁹ The two methods give coincident results except for the cancellation of coma and other higher order aberrations. Moreover, some discrepancies in the equations on the coma aberrations can be found between Refs. 16, 18, and 20. It is not our purpose to solve here those discrepancies (see also the Appendix). The ultimate values are those given by the ray tracing. The logical procedure that we used is the following.

First we assign the E_0 central energy ($E_0 = 900\ \text{eV}$) where the instrument is optimized. For E_0 we assign the total length L , the included angle $\theta_0 = (\alpha_0 + \beta_0)/2$, the incidence angle on the detector γ , the average ruling density a_0 , the reference source size S_1 , the effective spatial resolution of the detector S_2 , and the diffraction order k (in our case first internal order, $k = +1$). We define the local ruling density as $a(w) = a_0 + a_1 w + a_2 w^2 + \dots$, where w is the local coordinate along the grating, oriented in the direction of the light propagation, and equal to zero at the center of the grating ruled surface. The grating equation gives the α_0 and β_0 for E_0 . We can then equalize the contribution to the LW coming from the source size and the detector resolution. By also imposing the condition on the total length, we get thus the entrance and exit arms r_1 and r_2 at E_0 . By then imposing the condition of focalization and the incidence angle on the detector, we obtain the radius of curvature R and the linear VLS parameter a_1 . Finally we can estimate a_2 by using one of the expressions found in the literature for the cancellation of the coma aberration. In our case we found that the optimal a_2 value obtained with the ray tracing is rather different from the one of analytical formulations, probably because in the ray tracing also all the other higher order optical aberrations are intrinsically included, so that a_2 is used to minimize the contributions from all of them. All the used equations are given in the Appendix.

The optimized parameters are $a_0 = 3200\ \text{mm}^{-1}$, $a_1 = 0.9\ \text{mm}^{-2}$, $a_2 = 1.2 \times 10^{-4}\ \text{mm}^3$, and $a_3 = a_4 = 0$, $R = 58.55\ \text{m}$ (radius measured on the actual substrate before the ruling procedure). The a_2 parameter is optimized at given r_1 and α for only one energy, but for a given a_2 it is possible to cancel the coma aberration by choosing other values of α and r_1 . The set of convenient α and r_1 is given in Fig. 2 for different photon energies (bottom panel). The horizontal lines indicate the accessible r_1 range for SAXES: clearly for all the energies it is possible to cancel the coma aberration in more than one way. This explains in a more quantitative way our choice of having precise movements for α and r_1 . The results of Fig. 2 also make clear that the a_2 parameter is by no means critical and could be set to zero. Nevertheless we adopted the above tiny value with marginal benefits pointed out by extensive ray-tracing work. It must also be noted that Fig. 2 was obtained using the analytical expressions, because the results are very close to those given by the ray tracing (data not shown but obtained for many cases).

This design corresponds to a complete compensation of

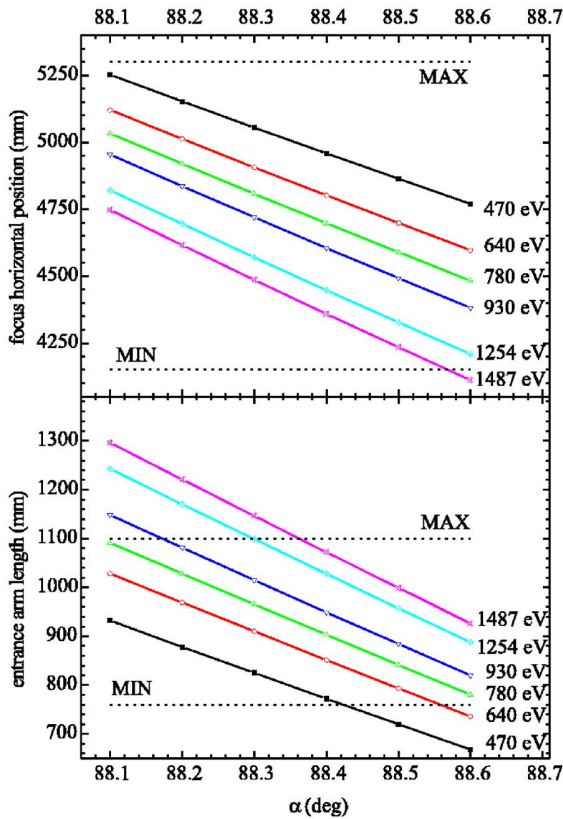


FIG. 2. (Color online) The set of optical parameters minimizing the coma aberration contribution over the whole SAXES energy range. Lower panel: incidence angle on the grating (α) and entrance arm length r_1 . The MIN and MAX lines indicate the limits of r_1 allowed by the actual SAXES mechanics. Top panel: the corresponding values of the total horizontal length of SAXES.

all the aberrations with a vertical opening of 2 mrad. In this case the line shape simulated by ray tracing is symmetric within 3%. Moreover, the resolving power is slightly dependent on the working point at the minimum coma and this is a further degree of freedom. In the working conditions of Fig. 2, the magnification is always around 1 as desired.

III. THE SAXES COMPONENTS AND THE EXPERIMENTAL SETUP

An overview of the instrument is given in Fig. 3, where some of the mechanisms holding the vacuum chambers and bellows are not shown for clarity. It must be noted that all the movements and structural parts are independent of the vacuum chambers, in order to maximize the stability of the system. In the drawing we show also the 5 m long girder on which the spectrometer is installed; this ensures the rigidity necessary to move the spectrometer on the beamline floor (air cushion system) without losing the delicate internal optical alignment. Some technical questions deserve to be briefly discussed. We list them following the path of the light neglecting all the trivial information on conventional techniques (vacuum, slide mechanics, and data reduction).

A. Input slit

The input slit protrudes into the sample chamber and it is mounted onto a slide mechanism to be possibly placed very close to the sample (minimum of 5 mm) in order to optimize the optical matching. The whole slit mechanics has been designed and built in house. It is operated by an accurate ($0.1 \mu\text{m}$) actuator in air through a leverage and a bellow with antagonist springs. The schematic leverage system adopted to ensure a parallel opening of the two blades is

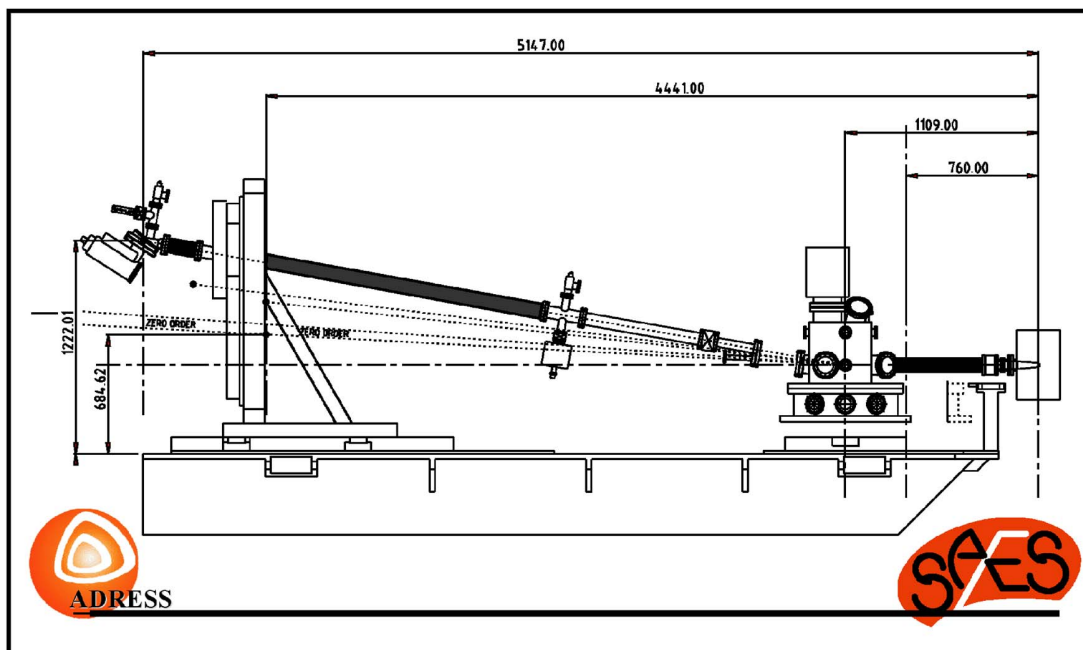


FIG. 3. (Color online) The mechanical simplified construction draft of SAXES. The sample is at the right side. The big grating chamber (600 mm internal diameter) houses the motorized in vacuum mechanics with four degrees of freedom. The whole spectrometer is supported by a single steel girder allowing fine regulation of the vertical position. The girder can rotate around a vertical axis passing on the sample, thanks to an air cushion device; this will allow the study of transferred photon momentum dependent RIXS spectra.

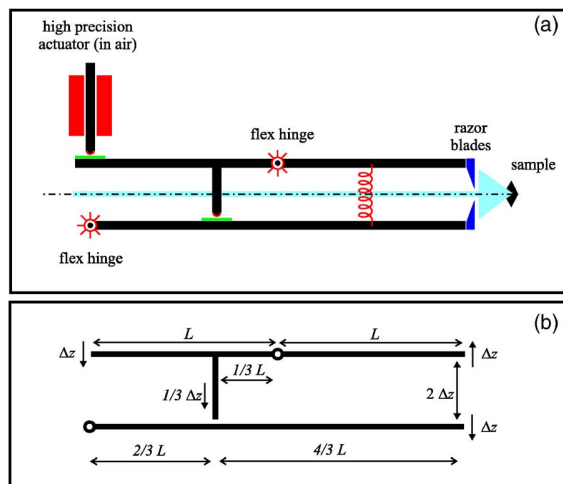


FIG. 4. (Color online) The schematic entrance slit mechanical layout. The two blades open symmetrically, thanks to the choice of the lever arms. One single high precision actuator acts, from the air side, in the leverage. The rotation is provided by two metallic flexible hinges. The long arms are needed to place the actuator along the entrance arm, away from the sample vacuum chamber. Panel (A): The beam proceeds, inside the slit mechanics, from the sample towards the grating after having been selected by the slit. A couple of in vacuum springs are used to counterbalance the actuator. Panel (B): The simple leverage ratios that bring to a 1:2 opening of the slit with respect to the actuator movement ($L=140$ mm).

shown in Fig. 4. The slit can be opened to a large value (about 1 mm) when slitless operation is desired. In such a case the source for the grating is directly the spot on the sample. The whole slit mechanism is within a metallic protection to prevent stray visible light to enter the spectrometer and to reduce drastically the coupling of the vacuum in the input arm and in the sample chamber.

B. Mask

A mask, having several apertures of different vertical openings and placed just before the grating, is used to define the vertical aperture, i.e., the illuminated area on the grating surface (see Fig. 1). The vertical movement of the mask is motorized and computer controlled.

C. Grating

The grating (substrate in Pyrex, reflective coating in platinum) manufactured by Horiba Jobin Yvon is holographically made by ion etching of the laminar profile grooves.²¹ The holography approximates very well the polynomial density law given above (the theoretical maximum error on the local groove density is $0.006/3200=2 \times 10^{-6}$). This high accuracy is possible because the corrections to the constant density are rather modest. The grating dimensions are $20 \times 130 \times 15$ mm³. The efficiency estimated by the manufacturer ranges between 3% and 4% over the whole range at 88.3° incidence angle.

D. Grating mechanics

The regulation of the input arm length is obtained by displacing longitudinally the entire vacuum chamber housing the grating with a computer controlled slide mechanism. All

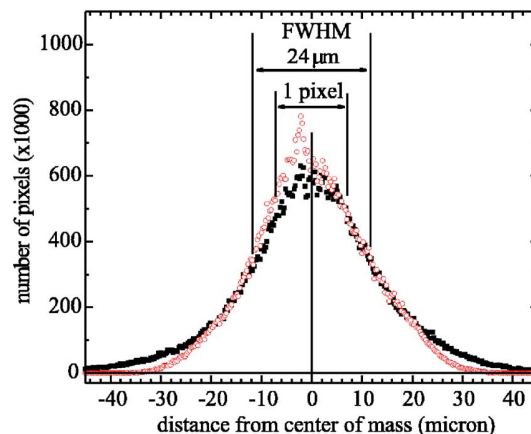


FIG. 5. (Color online) The histogram of the charge cloud distribution on the CCD detector in the event of a single photon detection. The pixel lateral size is $13.5 \mu\text{m}$. In both directions of the CCD array (full black squares perpendicular to energy dispersion direction, open red circles along the dispersion direction), the full width at half maximum of the curve is around $24 \mu\text{m}$, i.e., almost twice the pixel size. See text for details on the procedure used to construct this histogram.

the other movements of the grating (pitch for changing α , rolling, vertical positioning, and horizontal transverse movement to allow the use of a second, easily selectable grating) are high precision in vacuum motorized movements manufactured by Micos GmbH.

E. CCD detector

The CCD detector is a special delivery by Princeton Instruments (Roper Scientific Inc.)²² and is based on a thinned and back-illuminated wafer 27.6×27.6 mm² with 2048×2048 pixels ($13.5 \times 13.5 \mu\text{m}^2$). It is mounted on a CF 150DN flange in such a way to protrude into the vacuum chamber by about 22 mm. In this way the flange can be mounted inclined so that γ is about 20° (see Fig. 1) without shadowing the wafer. The angle γ can be adjusted by rotating the camber of the detector from 10° to 30° . With a mounting of this type it is impossible to use a Peltier cooling to sufficiently reduce the dark current. Thus the detector is cooled with a liquid nitrogen cryostat. The electronically controlled operating temperature is -100°C and the dark current is practically zero (1 electron/h pixel), so that the system adds to the statistical fluctuation only the readout noise (5.5 electrons/pixel at 100 kHz).

The spatial resolution of the detector is a crucial parameter and it has been measured in a special experiment whose results are summarized in Fig. 5. We have illuminated the detector with a uniform and weak flux of x rays from a traditional source (Cu anode, 930 eV energy) for a short time (around 1 s) at a distance of 2 m. The low exposure ensures that the vast majority of the photons appears in the image as isolated spots over the dark background (no double events). Due to the photon absorption and charge release mechanisms in the CCD wafer, a single photon results in a charge cloud shared by a number of neighboring pixels (split events), and only seldom the whole charge is in a single pixel. This fact implies that the effective spatial resolution of the CCD is worse than the pixel size, and it has been shown that it is

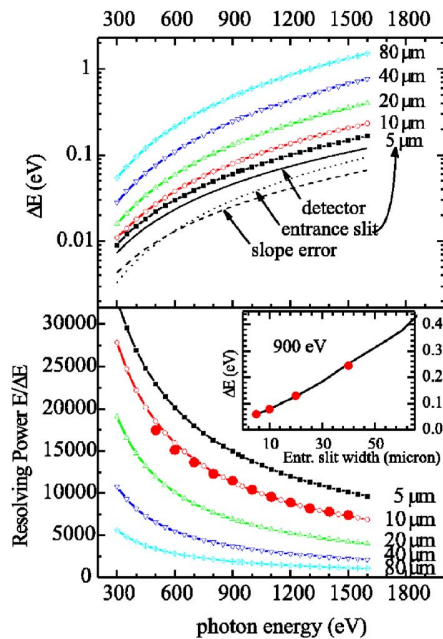


FIG. 6. (Color online) The expected resolution performances of SAXES. Top panel: The expected linewidth (LW) vs photon energy for various openings of the entrance slit (small symbols). For the minimum slit ($5 \mu\text{m}$), the slit contributions compared to the expected contributions from the grating slope error and CCD spatial resolution (with $\gamma=20^\circ$). Bottom panel: The corresponding values of the resolving power $E/\Delta E$. The big red circles indicate the resolving power estimated by ray tracing; all the other values are estimated by analytical expressions. In the inset the LW dependence on the slit opening at the important case of 900 eV .

almost independent of it.²³ We have statistically analyzed this phenomenon over thousands of those spots; the results are shown in Fig. 5, where the histogram of the charge spatial distribution is given for the two dimensions of the detector. For each spot we have determined the center of mass of the charge accumulated in the various pixels, along rows and columns, with an accuracy of $1 \mu\text{m}$ in the CCD space; then we have attributed the weight of each pixel of that spot to the corresponding distance from the center of mass; and repeating this procedure for thousands of spots results in the smooth and highly resolved histogram of Fig. 5. In the specific case of our CCD, the FWHM of the histogram is about $24 \mu\text{m}$. It is important to remark that the average charge cloud is the same in the two directions, despite the grazing incidence. This fact further supports the use of CCD detectors at grazing incidence.

IV. THE PERFORMANCES OF SAXES

The typical theoretical average resolving power with various openings of the input slit over the whole working energy range is given in Fig. 6 showing values fully consistent with the general goals of the project. In this evaluation the coma contribution is neglected in the analytical evaluation of the LW (small symbols in both panels), whereas the requested slope error ($0.97 \mu\text{rad}$) is taken into account. From the top panel it appears clearly that the slope error contribution is negligible already with $S_1=5 \mu\text{m}$. The measured slope error is $0.67 \mu\text{rad}$, better than the requested $0.97 \mu\text{rad}$, so in the ray tracing we neglected the grating slope error. The

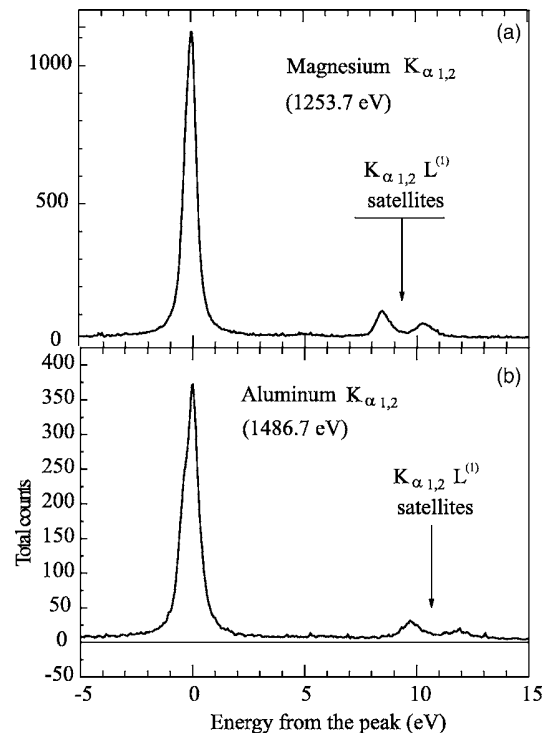


FIG. 7. The Mg and Al $K_{\alpha 1,2}$ emission spectra measured with SAXES. The $K_{\alpha 1,2}L^1$ satellites are used to calibrate in a precise way the energy scale by comparison with published spectra. The calibration is in good agreement with the expected one. The main peak in both cases is asymmetric due to the $2p$ level spin-orbit splitting. The spectra were measured with a $10 \mu\text{m}$ entrance slit and an accumulation time of about 20 min. See text for details.

ray-tracing results for $S_1=10 \mu\text{m}$ are shown in the bottom panel by the big circles; the agreement with the analytical results is excellent. In consideration of the expected spot size on the sample ($9 \mu\text{m}$), we consider as ultimate performances of SAXES those obtained with $S_1=10 \mu\text{m}$, also because the main contribution to the LW comes already from the CCD spatial resolution.

The SAXES performances have been tested with the fluorescence emission lines Al $K_{\alpha 1,2}$ and Mg $K_{\alpha 1,2}$ that are the only easily accessible options with a conventional x-ray tube. This has the advantage of providing a test independent from the performances of the beamline where the instrument will be installed. Another advantage is that these lines (1486.7 and 1253.7 eV) are at the upper energy side of the SAXES range so that the test is very severe and really significant. Due to the spin-orbit splittings of the $2p$ shallow levels, the K_{α} emissions of Al and Mg are the superposition of two transitions to the K -shell hole from the $2p_{1/2}$ and $2p_{3/2}$ levels, respectively, giving two contributions with intensities in the ratio of 1:2. The parameters (i.e., spin orbit and lifetime broadening) are known from the literature and, in particular, from the NIST benchmark work,²⁴ where the two emission spectra were measured with a crystal spectrometer, much more effective at these energies both in resolving power and angular acceptance.

The raw data measured with $10 \mu\text{m}$ input slit and a mask reducing the vertical acceptance to 1 mrad are given in Fig. 7 in a 20 eV wide energy interval, i.e., from 5 eV below the peak to 15 eV above the peak. In this energy range also

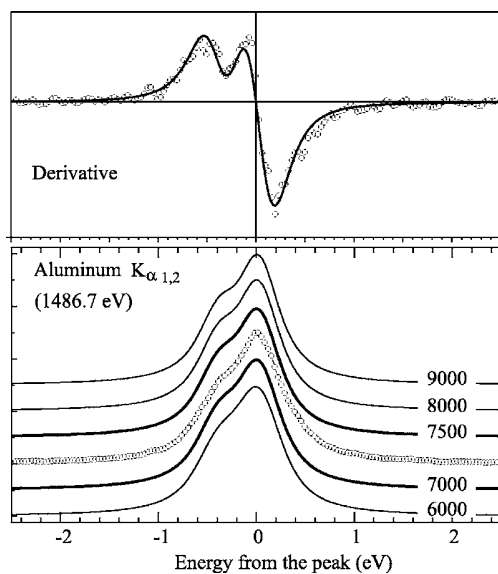


FIG. 8. To determine the actual resolving power of SAXES in the case of the Al spectrum of Fig. 6, we compare the experimental data to the simulated spectra obtained by a Gaussian broadening of the ideal spectrum measured with infinite resolving power. It must be noted that the Lorentzian lifetime broadening is unavoidable in the fluorescence emission lines. In the top panel the comparison is made using the derivatives of the measured and simulated spectra. At 1486.7 eV SAXES can clearly work with a resolving power better than 7000.

the $K\alpha L$ satellites due to fluorescence emission in the presence of multiple ionization are clearly seen. Since the satellite energy is known from the literature,²⁵ it is used to check the calibration of the spectra. A good point is that only a very weak scattered radiation background is present in the measured spectra, and this is particularly important in consideration of the bremsstrahlung contribution from the electron excited source (electron energy around 5–6 keV). Already in this scale of the drawing, the Lorentzian tails of the peaks due to finite lifetime are apparent. Moreover, it is seen that the Al line is clearly not a single peak. This is very crucial in the analysis of the resolution as shown in Fig. 8 where the peak is presented in an expanded scale (open points in lower panel). The experimental spectrum is compared with the theoretical spectra expected with various resolving powers. It is seen at a glance that the resolving power is greater than 6000 since the shoulder from the $2p_{1/2}$ transition is better seen in the experiment. On the other hand the resolving power is lower than 9000. Within the accuracy of the analysis, the measured spectrum is rather well compared with the spectra having 7000 and 7500 resolving powers given by heavy solid lines sandwiching the experimental spectrum. One can thus conclude that the resolving power is typically between 7000 and 7500 at 1486.7 eV, i.e., at the upper side of the SAXES working range in excellent agreement with the expectations summarized in Fig. 6. This evaluation has rather small uncertainty since the parameters used in the simulated spectra are rather well known from Ref. 24; the spin-orbit energy splitting is 0.413 eV with an accuracy of ± 1 meV and it does not introduce ambiguity. The Lorentzian parameter $\Gamma = 0.45$ eV (FWHM) is in the numerical range given in the NIST paper²⁴ and is obtained by fitting the tails of the mea-

sured spectrum in perfect agreement with our fitting of the NIST spectrum itself. In fact, the lifetime parameter determines completely the tails when the resolving power is above about 5000–6000 so that Γ is obtained safely from the data without making any assumption on the resolution. A further confirmation of the above resolution analysis is given by the derivative of the spectra having the advantage of enhancing the fingerprints of the doublet nature of the peak. This is given in the upper panel of Fig. 8 where the open dots are the experiment and the solid line is the theoretical spectrum expected with a resolving power of 7250. The general agreement is excellent. The transition from positive to negative derivative across the peak is perhaps sharper in the experiment, suggesting a resolving power slightly above the value estimated above. However, the noise makes this refinement of the analysis rather difficult. This is not done because it is beyond the scope of the present work.

A similar analysis has been done also with the Mg spectrum. As it is apparent from Fig. 8 and from Ref. 24 the Mg peak is narrower than in Al. This is due to a smaller spin orbit (0.251 eV) and to the narrower instrumental linewidth expected at this energy that is 233 eV lower. However, the analysis of the type done in Al has greater uncertainties in Mg because the Lorentzian broadening masks substantially the shoulder due to the smaller spin-orbit splitting as it is apparent also from the benchmark case. The result is a resolving power between 8000 and 10 000 which is in any case a further support to the good performances of SAXES. In fact, this value is consistent with the theoretical trend given in Fig. 6, confirming the successful performance of the instrument presented here.

Based on these tests we can safely predict that SAXES will be able to reach the targeted resolving power (higher than 10 000) for the whole 400–1100 eV range. The extreme resolution performances, the optimized optical matching to the dedicated ADDRESS beamline, and the possibility of changing the scattering angle make SAXES a rather unique tool for future RIXS spectroscopy on strongly correlated electron systems.

ACKNOWLEDGMENTS

The authors are indebted to F. van der Veen for encouragement and precious supervision of the project. The authors thank N. B. Brookes for his wise scientific and technical suggestions and F. Romanato for the willing support in the search for high quality blades for the SAXES entrance slit. They also acknowledge the excellent technical support provided by C. Farioli and A. Moroni. SAXES is a joint project of the Paul Scherrer Institut (PSI) and of the Politecnico di Milano. The SAXES spectrometer is property of the Swiss Light Source at the PSI.

APPENDIX

We summarize here the procedure we followed to determine the main optical parameters of SAXES. The used equations are taken from Refs. 16 and 18. The list of symbols is the following:

$$\alpha = \text{incidence angle on the grating,}$$

β = diffracted beam angle, positive sign,

$a(w) = a_0 + a_1 w + a_2 w^2 + a_3 w^3 + \dots$ = local groove density on the grating (in mm^{-1}),

r_1 = entrance arm,

r_2 = exit arm,

R = radius of curvature of the grating surface,

E_0 = reference photon energy,

$L = r_1 + r_2$ = total length at E_0 ,

S_1 = source size (in the dispersion direction),

S_2 = CCD spatial resolution,

γ = grazing incidence angle on the CCD,

$\theta = (\alpha + \beta)/2$,

$k = +1$ = diffraction order (first internal),

$K = 1.239842$

$\times 10^{-3} \text{ mm eV}$ = energy to wavelength conversion,

$s' = 0.2 \text{ arc sec}$

$= 0.96 \mu\text{rad}$ = grating surface slope error.

Some of the parameter values are predetermined by external requirements or technological limitations ($S_1 = 8 \mu\text{m}$, $S_2 = 28 \mu\text{m}$, $a_0 = 3200 \text{ mm}^{-1}$, and $L = 5 \text{ m}$) and others are chosen for scientific reasons (energy range of 400–1600 eV, $E_0 = 900 \text{ eV}$). Thus, given E_0 , θ_0 , a_0 , and k , from the grating equation we get

$$\varphi_0 = \frac{\alpha - \beta}{2} = \arcsin \frac{a_0 k K}{2 \cos \theta_0 E_0},$$

$$\alpha = \theta_0 - \varphi_0,$$

$$\beta_0 = \theta_0 + \varphi_0.$$

Considering $(S_2 \sin \gamma)$ the effective spatial resolution of the detector at grazing incidence, the contributions to LW coming from S_1 and S_2 are

$$\Delta E_1 = S_1 \frac{\cos \alpha}{r_1 a_0 k K} E^2,$$

$$\Delta E_2 = S_2 \sin \gamma \frac{\cos \beta}{r_2 a_0 k K} E^2,$$

By requiring $\Delta E_1 = \Delta E_2$ and $r_1 + r_2 = L$, we find

$$r_{2,0} = \frac{S_2 \cos \beta_0}{S_1 \cos \alpha + S_2 \cos \beta_0} L,$$

$$r_1 = L - r_{2,0}.$$

We can now impose that the system be on focus,

$$\frac{\cos^2 \alpha}{r_1} + \frac{\cos^2 \beta_0}{r_{2,0}} = \frac{\cos \alpha + \cos \beta_0}{R} + \frac{kK}{E_0} a_1,$$

and that the focal curve be tangent to the CCD detector,

$$\frac{1}{r_2} \frac{\cos \beta_0}{\tan \gamma} + \frac{\tan \beta_0}{R} + \frac{a_1}{a_0} = \frac{2 \sin \beta_0}{r_{2,0}},$$

and we can obtain R and a_1 :

$$R = \frac{(E_0/kK)(\cos \alpha + \cos \beta_0) - a_0 \tan \beta_0}{(E_0/kK)[(\cos^2 \alpha)/r_1 + (\cos^2 \beta_0)/r_2] - (a_0/r_{2,0})[2 \sin \beta_0 - (\cos \beta_0)/(\tan \gamma)]},$$

$$a_1 = \frac{E_0}{kK} \left(\frac{\cos^2 \alpha}{r_1} + \frac{\cos^2 \beta_0}{r_{2,0}} - \frac{\cos \alpha + \cos \beta_0}{R} \right).$$

Finally we find a_2 with the following equation, obtained by modifying the ones given in Ref. 16 or in Ref. 18 (which, incidentally, do not coincide) and “optimized” empirically by comparing the results with ray tracing:

$$a_2 = \frac{3 E_0}{8 k K} \left[\left(\frac{1}{R} - \frac{\cos \alpha}{r_1} \right) \frac{\sin 2\alpha}{r_1} - \left(\frac{1}{R} - \frac{\cos \beta_0}{r_{2,0}} \right) \frac{\sin 2\beta_0}{r_{2,0}} \right].$$

For E_0 we know now r_1 , r_2 , α , and β_0 and we have assigned the grating parameters R , a_0 , a_1 , and a_2 . For any E we can thus calculate β , r_2 , and γ , having decided in advance what α and r_1 one wants to use (see Fig. 2),

$$\beta = \arcsin \left(\sin \alpha - \frac{kK}{E} a_0 \right),$$

$$r_2 = \frac{\cos^2 \beta}{(\cos \alpha + \cos \beta)/R - (\cos^2 \alpha)/r_1 + (kK/E)a_1},$$

$$\gamma = \arctan \frac{\cos \beta}{2 \sin \beta - r_2 [(\tan \beta)/R + a_1/a_0]}.$$

The contributions to the LW from the finite size of the source, the spatial resolution of the CCD, and the grating surface slope error are then

$$\Delta E_1 = S_1 \frac{\cos \alpha}{r_1 a_0 k K} E^2,$$

$$\Delta E_2 = S_2 \sin \gamma \frac{\cos \beta}{r_2 a_0 k K} E^2,$$

$$\Delta E_{SE} = \frac{2s'}{\tan(\alpha - \beta)} E.$$

It is very difficult to give a reliable estimate of the ΔE coming from the coma aberration, because the analytical expressions given in the literature are not unanimous and because the effects of coma are not symmetric on the energy peak and are quadratic with the footprint length on the grating. We limit ourselves to consider it small because we know that for every energy it is possible to minimize it more or less empirically. In the calculations of LW and resolving power, we have quadratically summed the three contributions. As already mentioned in Sec. II all the parameters were checked by ray tracing and the best value of a_2 was also found by simulations; it must be considered that other higher order aberrations can give a contribution, so the optimized value of a_2 can be different from the calculated one because it is utilized to reduce also types of aberrations other than coma.

¹ A. Kotani and S. Shin, *Rev. Mod. Phys.* **73**, 203 (2001).

² J. Nordgren, *J. Electron Spectrosc. Relat. Phenom.* **110–111**, ix (2000).

³ A. Kotani, *Eur. Phys. J. B* **47**, 3 (2005).

⁴ T. A. Callcott, K. L. Tsang, C. H. Zhang, D. L. Ederer, and E. T. Arakawa, *Rev. Sci. Instrum.* **57**, 2680 (1986).

⁵ J. Nordgren, J. Bray, S. Gramm, R. Nyholm, J.-E. Rubensson, and N. Wassdahl, *Rev. Sci. Instrum.* **60**, 1690 (1989).

⁶ S. Shin, A. Agui, M. Fujisawa, Y. Tezuka, and T. Ishii, *Rev. Sci. Instrum.* **66**, 1584 (1995).

⁷ C. Dallera, E. Puppini, A. Fasana, G. Trezzi, N. Incorvaia, L. Braicovich,

N. B. Brookes, and J. B. Goedkoop, *J. Synchrotron Radiat.* **3**, 231 (1996).

⁸ D. Cocco, M. Matteucci, K. C. Prince, and M. Zangrando, *Proc. SPIE* **4506**, 46 (2001); D. Cocco *et al.*, *AIP Conf. Proc.* **705**, 873 (2004).

⁹ C. F. Hague, J. H. Underwood, A. Avila, R. Delaunay, H. Ringuenet, M. Marsi, and M. Sacchi, *Rev. Sci. Instrum.* **76**, 023110 (2005).

¹⁰ Y. Chuang, J. Pepper, W. McKinney, Z. Hussain, E. Gullikson, P. Batson, D. Qian, and M. Z. Hasan, *J. Phys. Chem. Solids* **66**, 2173 (2006).

¹¹ T. Tokushima, Y. Harada, H. Ohashi, Y. Senba, and S. Shin, *Rev. Sci. Instrum.* **77**, 063107 (2006).

¹² G. Ghiringhelli, A. Tagliaferri, L. Braicovich, and N. B. Brookes, *Rev. Sci. Instrum.* **69**, 1610 (1998).

¹³ J. Chavanne, P. Van Vaerenbergh, P. Elleaume, and T. Gunzel, *Proceedings of EPAC 2000*, Vienna, Austria, 2000, p. 2346.

¹⁴ G. Ghiringhelli *et al.*, *Phys. Rev. Lett.* **92**, 117406 (2004).

¹⁵ J.-M. Mariot, M. Sacchi, L. Journel, J.-J. Gallet, M. McElfresh, and C. F. Hague, *Nucl. Instrum. Methods Phys. Res. B* **246**, 176 (2006).

¹⁶ K. D. Osborn and T. A. Callcott, *Rev. Sci. Instrum.* **66**, 3131 (1995).

¹⁷ W. R. McKinney, *Rev. Sci. Instrum.* **63**, 1410 (1992).

¹⁸ M. R. Howells, in *X-ray Data Booklet*, edited by A. Thompson *et al.* (Lawrence Berkeley National Laboratory, Berkeley, 2001), <http://xdb.lbl.gov/>

¹⁹ The original SHADOW package is available at <http://www.nanotech.wisc.edu/CNTLABS/shadow.html> and the graphical user interfaces for personal computer at <http://www.esrf.fr/computing/scientific/xop/>

²⁰ H. Noda, T. Tamioka, and N. Seya, *J. Opt. Soc. Am.* **64**, 1031 (1974).

²¹ http://www.jobinyvon.com/usadivisions/VUV/variable_line.htm

²² <http://www.piacon.com/products/pisx/>

²³ E. Dinardo *et al.*, *Nucl. Instrum. Methods Phys. Res. A* (in press).

²⁴ J. Schweppe, R. D. Delattes, T. Mooney, and C. J. Powell, *J. Electron Spectrosc. Relat. Phenom.* **67**, 463 (1994).

²⁵ O. Mauron, J.-Cl. Dousse, J. Hoszowska, J. P. Marques, F. Parente, and M. Polasik, *Phys. Rev. A* **62**, 062508 (2000).

2.3 ADRESS beamline

The Swiss Light Source (SLS) at the Paul Scherrer Institut (PSI) is a third-generation synchrotron light source. With an energy of 2.4 GeV, it delivers a very large spectrum of synchrotron light ranging from infrared light to hard X-rays. It features top-up injection current at 400mA, producing a constant beam intensity for experiments. The high brightness photon beams are used for research in materials science, biology and chemistry. Along the 288m storage ring, it has a mixture of straight sections (short, medium and long), allowing an optimal use of a variety of undulators. The ADvanced RESonant Spectroscopies (ADRESS) beamline is located at a medium straight section of the storage ring, numbered 3M in Figure 2.5. As its name suggests, it is aiming to be a high resolution beamline in the soft x-ray range. It is specially designed for RIXS experiments, providing photons with high resolution as well as high flux. The parameters can be summarized in Table 2.2.

2.3.1 Synchrotron radiation

It is a well-known result of classical electromagnetism that any charged particles will radiate when accelerated [33]. However when charge particles are accelerated near the speed of light, due to the relativistic Lorentz contraction the radiation pattern is distorted from the isotropic dipole pattern expected from non-relativistic theory into an extremely forward-pointing cone of radiation. This makes synchrotron radiation sources the brightest sources of X-rays.

At the SLS, the electrons are first accelerated by a booster synchrotron to a velocity close to the speed of light. Then electrons are injected into the storage ring where they circulate for hours. In the storage ring, dipole bending magnets are installed to force electrons into a circular path. As the electron path bends, light is emitted tangentially to the curved path and streams down pipes called beamlines and is then monochromatized and made available to the experiments.

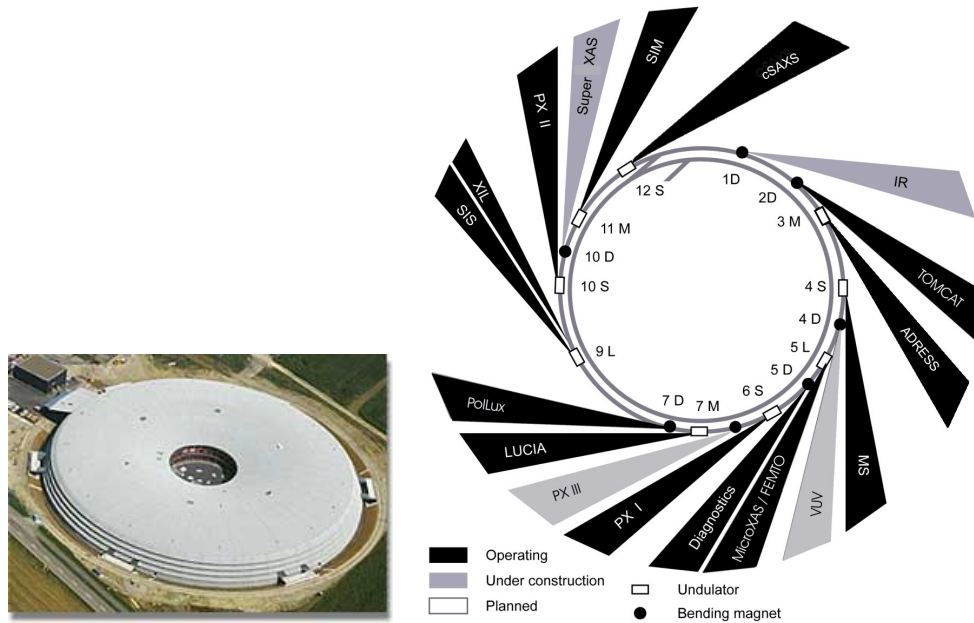


Figure 2.5: Left: Bird view of Swiss Light Source building. Right: Layout and status of beamlines in 2007.

Table 2.2: ADRESS parameters

Energy Range	400-1800 eV
Energy Resolution	up to 30,000 at 1000 eV
Polarization	circular and 0-180° variable linear polarization
Flux on sample	10^{13} photon/s/0.01%BW/0.4 A
Spot size on sample	$8.5 \times 100 \mu m^2$

Additional special magnetic structures known as insertion devices, generate specially shaped magnetic fields that drive electrons into an oscillating trajectory for linearly polarized light or sometimes a spiral trajectory for circularly polarized light. Each bend acts like a source radiating along the axis of the insertion device and the (partially) coherent superposition of the emission from the individual sources yields a high brightness beam [34].

2.3.2 Fixed gap undulator

Due to its high demanding requirements for flux and energy resolution, ADDRESS beamline uses an undulator as its insertion device. The undulator was implemented after the idea of R. Carr [35] by Thomas Schmidt [36]. Its an APPLE II type permanent magnet undulator with fixed gap opening. Although the concept was proposed very early, but this is the first time it actually implemented. The four magnet rows are mounted on a C-like frame, mechanically rigid construction, shown in Figure 2.6



Figure 2.6: Top view of UE44 undulator installed at ADDRESS.

In addition to the conventional linear horizontal, vertical and circular polarization, it features full linear rotation angles from 0° to 180° . In such a design, the energy change is done not by opening the gap as usual in an APPLE II undulator but by shifting the top two magnet rows relative to the bottom ones. All the four magnet rows have only longitude movements controlled by motors. This working principle is pictured in Figure 2.7

2.3.3 Optical layout

The optical scheme of the beamline adopts the concept [37] of the Plane Grating Monochromator (PGM) operated with collimated light, pictured

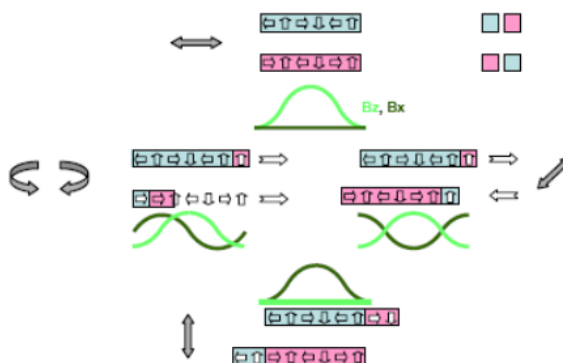


Figure 2.7: Working principle of the fixed gap undulator. The energy are changed through shifting upper and lower magnets relatively. Starting from a pure vertical field B_z (top), giving horizontal polarization, the shifts couple part of the field into the horizontal direction B_x . Shifting two diagonal arrays in the same direction produces horizontal fields with a quarter period phase shift, a shift in the opposite direction produces half a period phase shift between the field components. Depending on the phase, circular polarized light will be produced (middle, left side), or variable linear polarization (right side) from 0° to 180° . At a shift of half a period the vertical field vanishes, resulting in vertical polarization (bottom).

in Figure 2.8. This scheme benefits from wide energy range, and convenient optimization between resolution, flux and high-order suppression by tuning one single parameter, the so-called fixed-focus constant C_{ff} , defined as $C_{ff} = \cos\alpha/\cos\beta$, where α and β are the incidence and diffraction angles. Three exchangeable gratings are used to provide optimal coverage of the flux and resolution: a blazed 800 1/mm grating for maximal flux, and lamellar 2000 and 4200 1/mm gratings for maximal resolution. The beam coming from the undulator is vertically collimated and horizontally focused by a toroidal mirror. The collimated light gets monochromatized by grating diffraction. The cylinder shaped focusing mirror focuses vertically the beam onto the exit slit, and refocusing mirrors, toroidal and ellipsoidal shaped for ARPES and RIXS endstation, respectively, refocus the beam to the sample position.

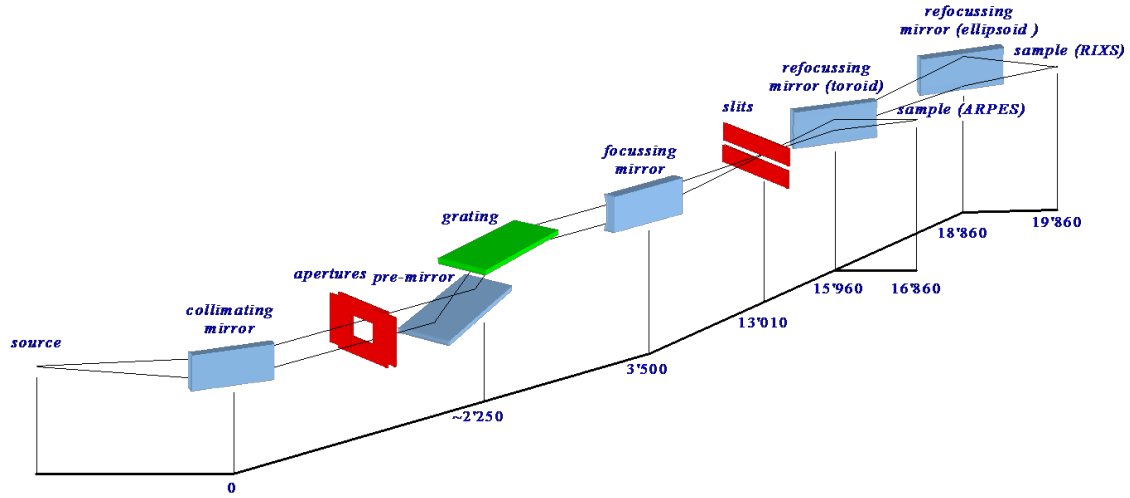


Figure 2.8: Schematic representation of ADDRESS (X03MA) beamline optics layout. The distance of every element is relative to the first optics, i.e. collimating mirror.

2.3.4 Performance

In order to characterize the spectral resolution and to demonstrate the performance of the beamline, photoionization spectra measurements of various atoms and molecules in the gas phase are normally adopted. For its availability and simplicity for judgement, nitrogen gas is used. During the measurements, the pressure inside the gas cell is kept constant at 1×10^{-2} mbar with a potential difference of up to 100V applied to the two electrodes. The recorded spectra are shown in Figure 2.9, using the 800 l/mm groove density grating and the typical C_{ff} value of 2.25. To characterize the spectral resolution, we determine the Q ratio of the first minimum to the third maximum which has been introduced by C.T. Chen [38]. With increasing resolving power, the value of Q decreases. In Figure 2.9, the blue curve shows a Q value of 0.727 at normal operation conditions, which balances between photon flux and resolving power. Closing down the frontend horizontal slit reduces the radiation cone seen from the beamline and improving resolution. Exit slit is effective to improve the resolution but too small values would only kill photon flux without improving

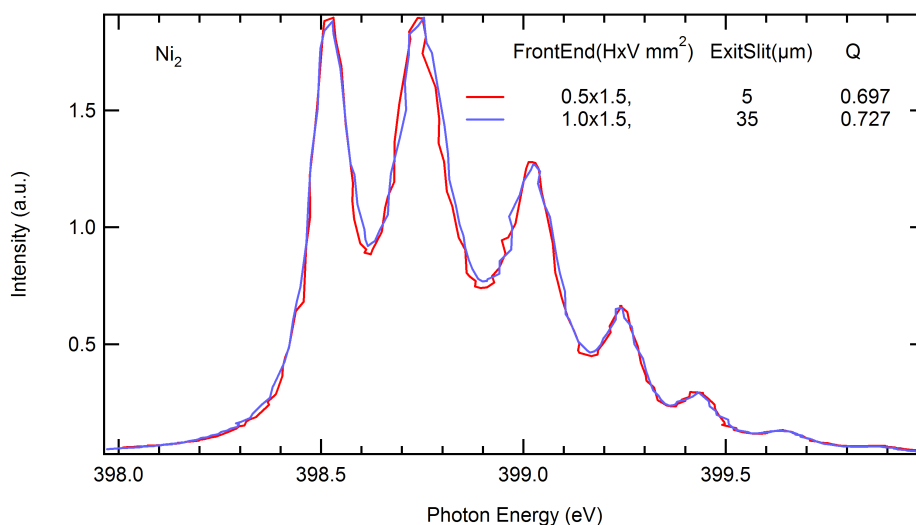


Figure 2.9: Photoionization spectrum of molecular nitrogen taken in the region of the $N_2 1s^{-1}\pi^*$ excitation measured with different frontend and exit slit opening tabulated inset.

resolution once beyond the beam vibration limit. A stable value of 0.697 is achieved when using a 0.5 mm horizontal frontend opening and 5 μm exit slit, which corresponds to a resolving power over 10,000.

2.3.5 Refocusing and spot size

The spot size is another important aspect to determine the overall performance. Achieving a sufficiently small vertical spot size will allow the SAXES spectrometer to operate with a fully open entrance slit, thus maximizing the acceptance of the instrument in the vertical (dispersive) direction. The vertical size of the beam at the monochromator exit slit is about 30 μm , so before reaching the sample, the beam has to be refocused by an ellipsoidal mirror. The mirror, fixed with its vacuum housing, is installed on a hexapod mount as in Figure 2.10. This system delivers sub-micrometer precision and repeatability in six degrees of freedom. The refocusing is done by fine tuning the ellipsoidal refocusing mirror, acting essentially on two parameters: the pitch (rotation around the y axis) gives the correct incidence angle and the yaw (rotation around the z axis)

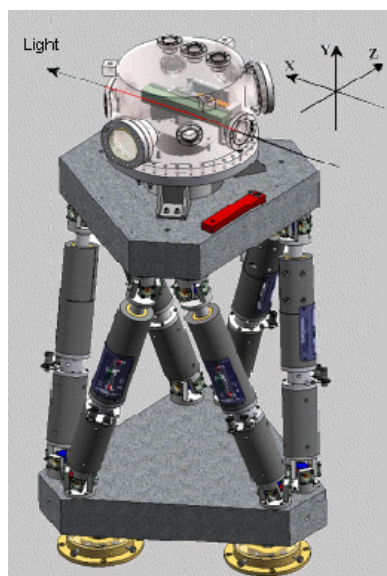


Figure 2.10: Refocusing mirror movements controlled by a hexapod support. Coordination system is specified inset, where x axis is along the beam, y and z are in the perpendicular plane.

matches the beam to the optical axis. To measure such small spot, we used the SAXES spectrometer in the zero order reflection mode, whereby the grating acts simply as a mirror. In that condition, SAXES can be used as a telescope yielding on the detector a polychromatic image of the beam spot on the sample. The result of one such test measurement is shown in Figure 2.11. The 2D image acquired by SAXES shows one very sharp horizontal line. Its width is estimated by further analysis at around 5.9 detector pixels. Taking into account the known magnification factor, this is corresponding to a $9 \mu\text{m}$ vertical spot size on the sample. The x-ray spot on the sample acts as the effective slit of SAXES in the vertical (dispersive) direction. Notice that the line which is actually horizontal in the laboratory reference frame, appears tilted due to a small misalignment of the CCD camera around its axis. This can be easily compensated by software.

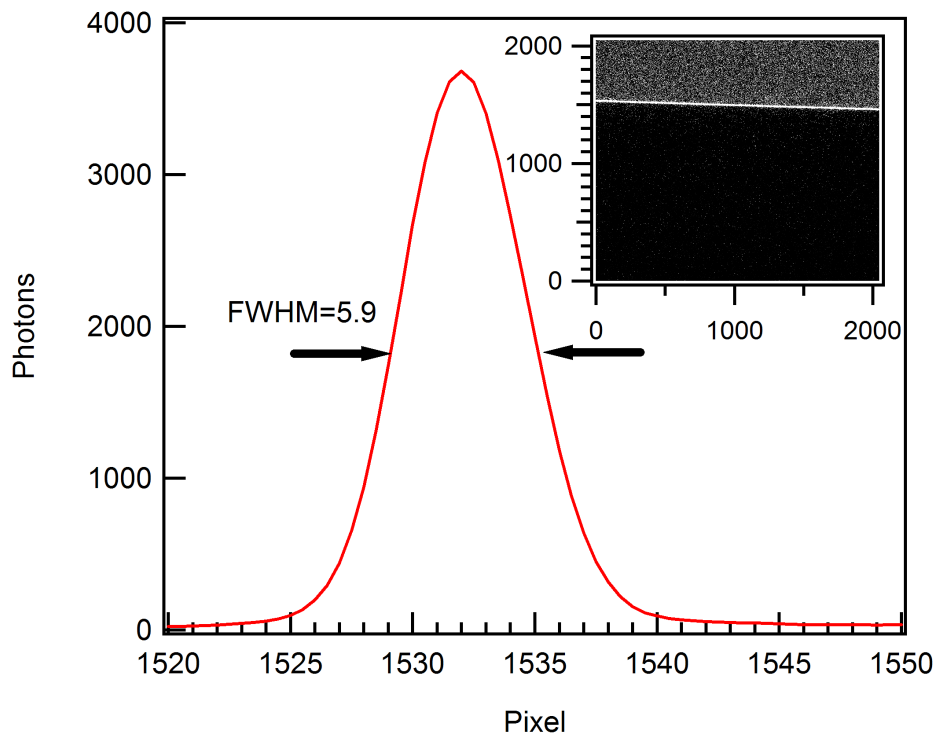


Figure 2.11: Spot size measurement. Zero order spectrum shows a FWHM of 5.9 pixels indicating a vertical spot size of $\sim 9 \mu\text{m}$. Inset is the corresponding 2D image.

2.4 Control system

A control system is required to control all beamline parameters, acquire data, and control motors. Ideally the control system would allow real-time data acquisition, status logging, as well as data visualization and analysis.

It was decided to use EPICS [39] as a control system. Not only does it deliver the requested functionality, but since it is in use at SLS a wide range of software and hardware as well as expertise was already available in-house. In principle EPICS is a TCP/IP based networking protocol (Channel Access), an extensive set of I/O device drivers and a database that allows values to be read, set or calculated either directly through simple commands issued by the user on a remote terminal or automatically as predefined.

SAXES CCD camera has its own dedicated software WinSpec/32 [40] for data acquisition and no direct driver available in EPICS. An intermediate layer is applied, i.e. CCD record from the synApps package [41]. It creates an EPICS server which provides the necessary CA records to control the CCD via the COM interface of WinSpec/32. This set up is sketched in Figure 2.12.

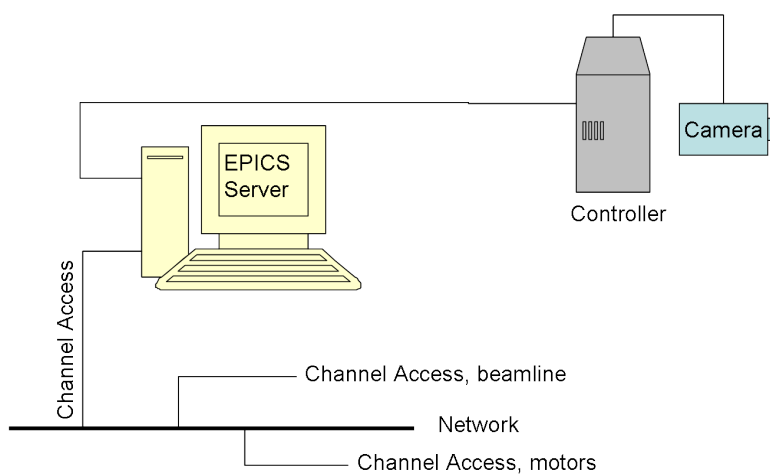


Figure 2.12: SAXES CCD camera integrated into EPICS system.

The data acquisition software is written in Python language [42] with extension support of EPICS CA communication [43]. It features a macro based design, i.e. beamline parameters, motors' movements, data acquisition are all controlled through corresponding commands. This allows users to program a sequence of cumulative measurements as soon as the best conditions have been found. The users are released from tedious waiting and can concentrate on data analysis while accumulating spectra. More important, the possibility of scheduling long sequences of data acquisition, with full control over the energy and polarization of the primary photon beam is a crucial condition for an efficient use of the beam, which is provided on a "round the clock" basis. The software also provides an intuitive graphical interface to edit, load, run macros, see Figure 2.13. The program is based on the cross platform toolkit Qt and its python binding PyQt [44].

2.4. Control system

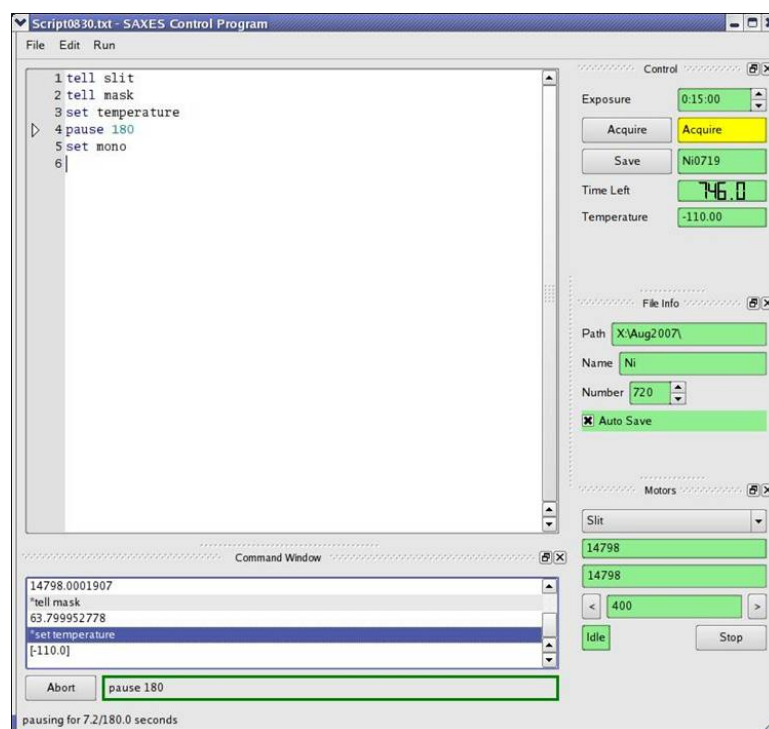


Figure 2.13: SAXES control program running a sequence of commands.

The online data visualization is done by a separate program to isolate data acquisition and visualization thus reduce crash risks. It features a simple click-and-view usage and a clean layout to show all functionalities. Thanks to the excellent third party libraries [45, 46], it provides modern controls to graph plots, e.g. zooming, comparison and fitting, see Figure 2.14.

The data analysis is done through an Igor Pro procedure. Thanks to Igor Pro's excellent programming capability, the procedure provides three easy-to-use panels to load and sum RIXS spectra, and convert pixels to energy loss scales, see Figure 2.15.

Chapter 2. SAXES and ADRESS

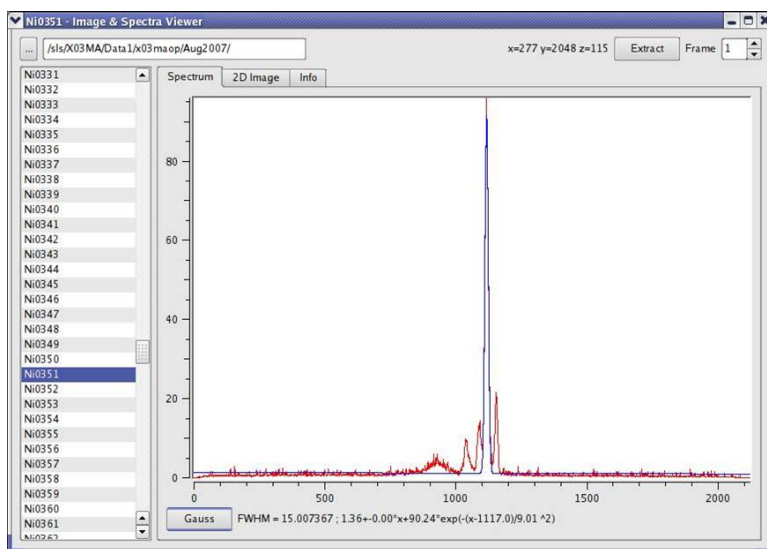


Figure 2.14: RIXS spectra viewer, providing 3 panels for spectra, 2D image and information.

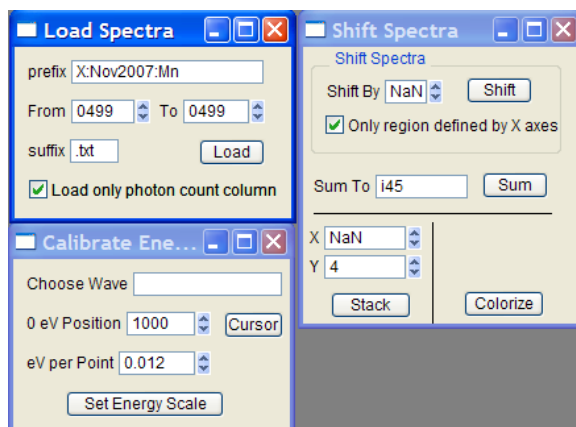


Figure 2.15: Igor Pro procedure to analyze the RIXS spectra.

Chapter 3

High resolution RIXS of NiO

Among all $3d$ transition metal monooxides, NiO has been considered to be a prototypical Mott insulator¹ and therefore its electronic properties have been extensively studied by many different techniques. This chapter presents original high resolution RIXS results on NiO - and of another insulating Ni compound, NiCl₂ - measured at the Ni L_3 , $M_{2,3}$ edges and at the O K edge. These provide a new experimental perspective on the local properties of the Ni $3d$ electrons in NiO, namely on the low energy spin excitations.

3.1 Ni L_3 edge

The measurements were performed at room temperature on a single crystal of NiO and on the layered compound NiCl₂. The NiO sample was simply cut in air showing a macroscopically smooth surface. Samples of NiCl₂ either cleaved in air or not yielded identical RIXS spectra. The polarization of the incoming beam was set to either linear horizontal (LH) or linear vertical (LV) polarized, corresponding respectively to a wave vector lying within or perpendicular to the horizontal scattering plane which contains the normal \vec{n} to the sample surface. The scattering angle was 90°,

¹More precisely, a “charge transfer insulator” as proposed by Zaanen, Sawatzky and Allen [11]

and the scattered beam made an angle of 20° with \vec{n} . The combined resolution reached during the experiment was 120 meV at Ni L_3 edge (853 eV), meaning a resolving power ($E/\Delta E$) better than 7000. It was determined from the FWHM of the elastic peak measured on a carbon tape sample.

3.1.1 *dd* excitations

Figure 3.1 shows a set of spectra taken across the Ni L_3 ($2p_{3/2} \rightarrow 3d$) edge measured with LH and LV polarized light. The upper panel shows the L_3 absorption spectrum measured in total electron yield; the marks indicate the excitation energies for the RIXS spectra. Two excitation energies are specially noted, i.e. "Peak" and "Satellite", corresponding to the maximum of the white line and, respectively, to a multiplet satellite at ~ 2 eV higher energy. These spectra are consistent with previous measurements (550 meV resolution) [47] but provide more detailed spectral structure thanks to the better experimental resolution of the ADRESS/SAXES instrument. The features within 4 eV of the elastic line appear at fixed positions on the spectra, i.e. at constant energy losses. Their relative intensities change as the excitation energy is swept across the XAS profile. Namely, the intensity of the feature identified at 4 eV increases in correspondence of the satellite excitation. At still higher excitation energies the low energy tail become pronounced and disperses towards higher energy losses. This transition from Raman- to fluorescence-like emission has been observed and discussed extensively by Ishii *et al* [48].

The spectral features from 4 to 0 eV can be identified by a simple crystal field model for a single Ni^{2+} (d^8) ion in octahedral coordination [49]. The $3d$ orbitals are split by the crystal field into the t_{2g} and e_g manifolds. The lowest-energy configuration is $t_{2g}^6 e_g^2$, and the ground state is the triplet ($S=1$) ${}^3A_{2g}$ state, with unpaired electrons in the $d_{x^2-y^2}$ and d_{z^2} orbitals. The level scheme is shown in Figure 3.2 as a function of the strength of the crystal field, expressed by the parameter $10Dq$ (Tanabe-Sugano diagram). The first excited state has ${}^3T_{2g}$ symmetry and $t_{2g}^5 e_g^3$ configuration, and it is separated by an energy equal to $10Dq$ from the ground state. In fact,

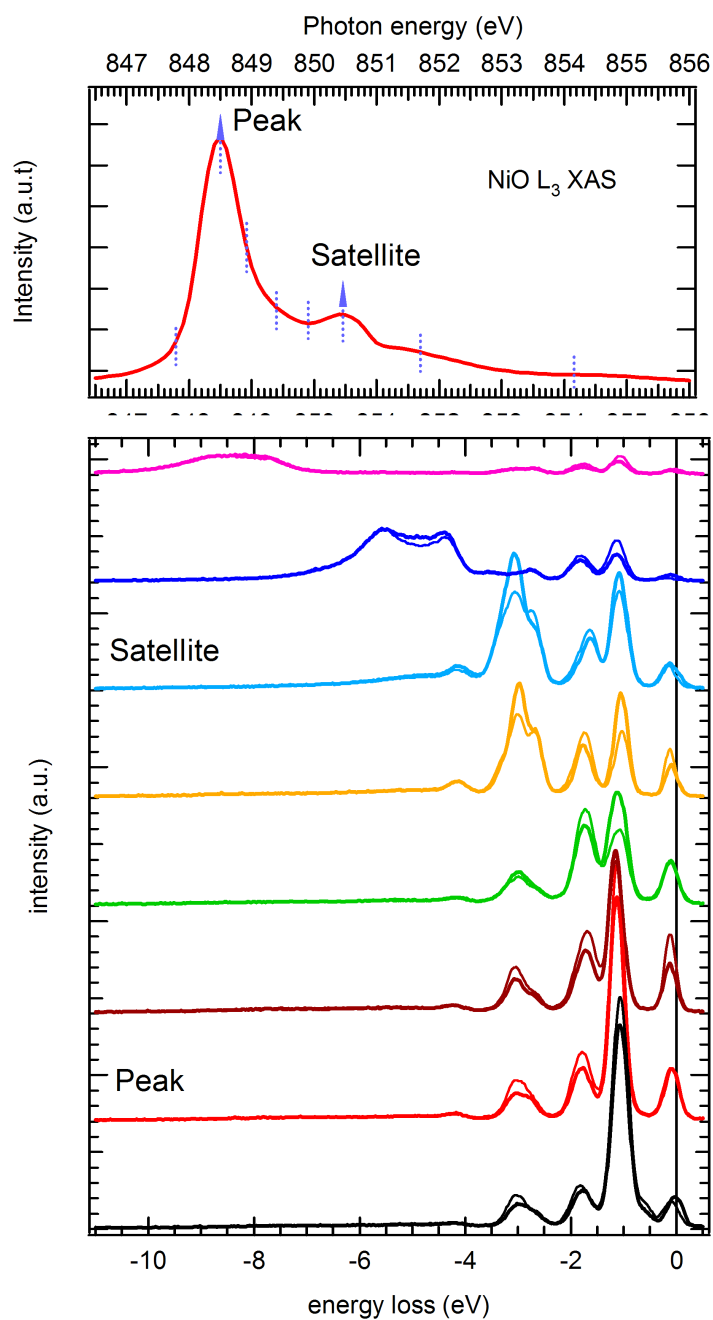


Figure 3.1: Top panel: XAS spectrum at Ni L_3 edge with indications of excitation energies. Bottom panel: RIXS spectra of NiO, ordered by excitation energies from the bottom up. At each excitation energy, the thin line and thick line correspond to LH and LV polarized incoming beam, respectively.

it corresponds to the promotion of one electron from a t_{2g} to an e_g state. A $10Dq$ value of 1.05 eV, indicated by red line in Figure 3.2, yields a very good agreement between the calculated energies of the excited states and the experimental energy positions. This is particularly clear from the first loss, which corresponds exactly to the dd excitation ${}^3A_{2g} \rightarrow {}^3T_{2g}$. Signatures of the ${}^3T_{2g}$ and 1E_g excited states can be found around 1.6 eV energy loss, while at higher energies the contributions from all other $3d^8$ multiplet states appear. It must be stressed that these dd transitions are dipole forbidden ($\Delta l=0$) and are indeed extremely weak in the optical spectra, where they become weakly allowed due to the coupling with lattice vibrations. Moreover, transitions to singlet ($S=0$) final states are doubly optically forbidden due to the change in the spin state. They can be observed in the optical spectra due to spin-orbit coupling in the $3d$ shell, but their intensities are extremely low. By contrast, all these final states are easily accessible by RIXS. In fact RIXS is a second-order process involving two optical transitions, thus enabling transitions with $\Delta L=0,1$ or 2. Moreover, transitions to different spin states become possible due to the strong spin-orbit interaction in the intermediate $2p^53d^9$ state.

3.1.2 Local spin-flip

The main interest in our measurement concerned the ${}^3A_{2g}$ state which, in the AFM phase of NiO, is split by superexchange into $m_s=-1,0,1$ Zeeman states, see the middle panel of Figure 3.2. Detailed RIXS calculations for an isolated Ni^{2+} ion in O_h symmetry have been presented in a seminal paper by deGroot, Kuiper and Sawatzky [50]. The interatomic exchange was treated by introducing an effective or "molecular" exchange field. The results are illustrated in Figure 3.3.

According to that theory, for an excitation energy in correspondence of the L_3 edge the transition to the ${}^3A_{2g}$ ($m_s=-1$) states should dominate. When the excitation energy is set above the L_3 edge, the transition to the $m_s=0, +1$ states should be visible, respectively separated in energy by one time and two times the "effective" exchange interaction J^* . In particular,

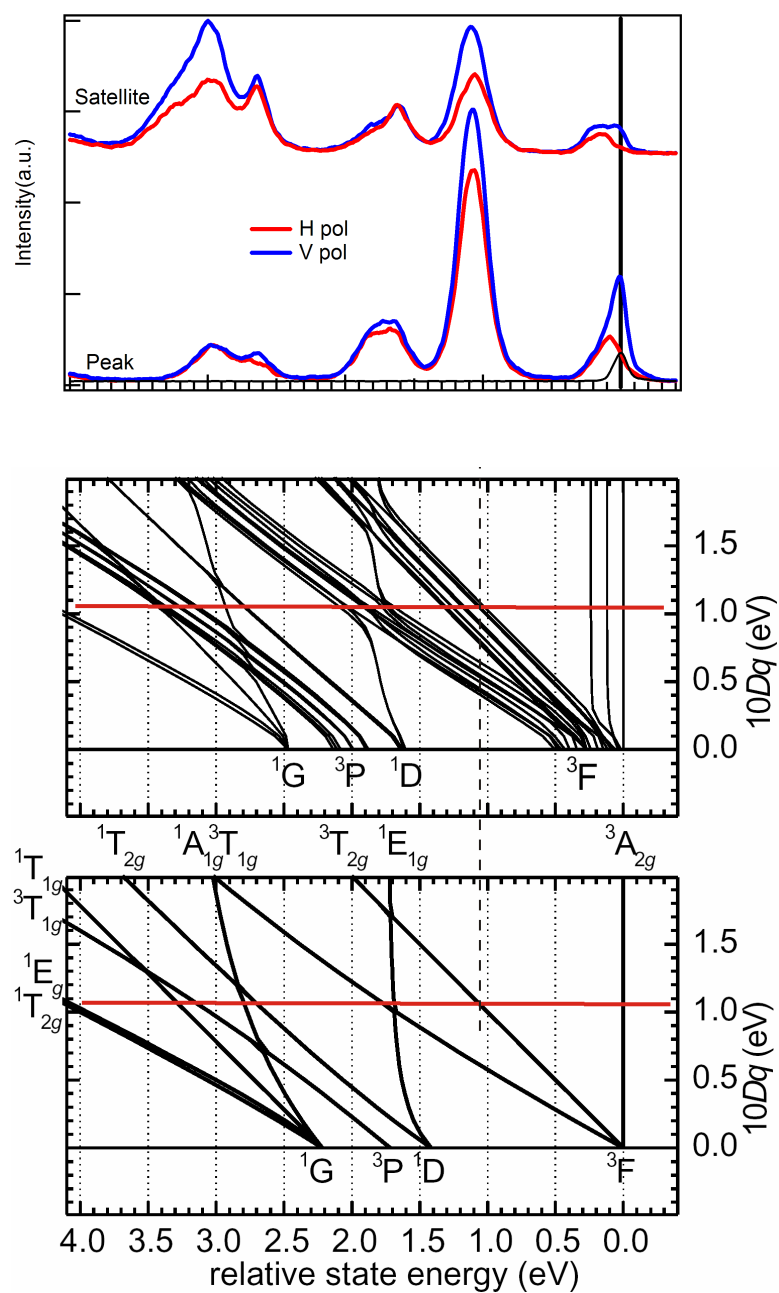


Figure 3.2: Top panel: NiO RIXS spectra measured at peak and satellite excitations for LH and LV polarized light. Middle and bottom panels are Sugano-Tanabe diagrams calculated with and without exchange field. The horizontal red line indicates $10Dq$ value of NiO.

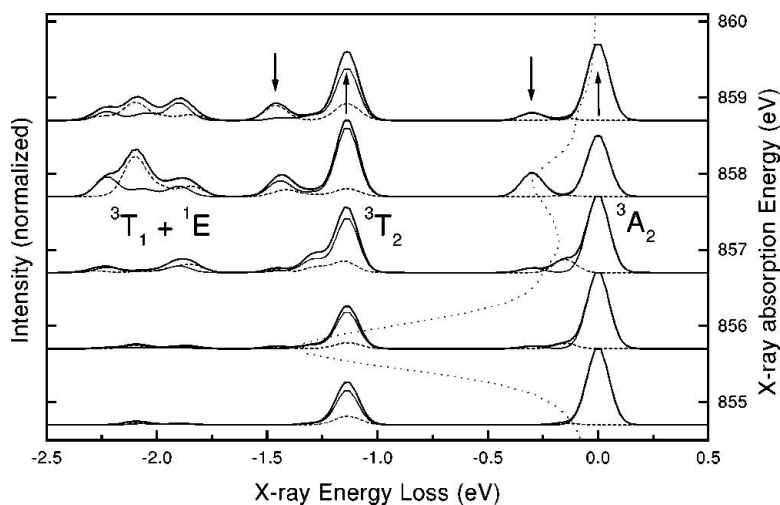


Figure 3.3: Calculated Ni L_3 edge RIXS spectra with 150 meV exchange field by de Groot [50]. The thin solid and dashed lines correspond to LV and LH polarization of the incident light, respectively, whereas the dot line indicates the x-ray absorption spectrum. The m_s substates are indicated at the top for spin up (\uparrow) and spin down (\downarrow).

when the excitation energy is chosen at the XAS satellite the direct spin flip peak to the $m_s=0$ state should be clearly observed. This has been confirmed with an atomic model calculation while considering only the spin excitations [51]. The results are summarized in Figure 3.4.

Our experimental measurements are quite consistent with the theory. At the L_3 edge the ${}^3A_{2g}$ ($m_s=-1$) state is strongly enhanced with respect to the $m_s=0, +1$ states. However an evident asymmetry is already found in the elastic peak. In correspondence of the satellite the transitions to the $m_s=0, +1$ states of the ${}^3A_{2g}$ symmetry become very pronounced and comparable with the elastic peak. The spin flip features are more evident for linear horizontal polarization of the incident light, due to the strong suppression of the elastic peak.

In order to verify the origin of the spin flip features the same measurements were also performed on NiCl_2 . In this compound the crystal field at the Ni site has the same O_h symmetry, but the hybridization with the Cl ligands is weaker, and the Ni-ligand distances are larger. Main differences from NiO are the distances and charges of the ligands with respect to the

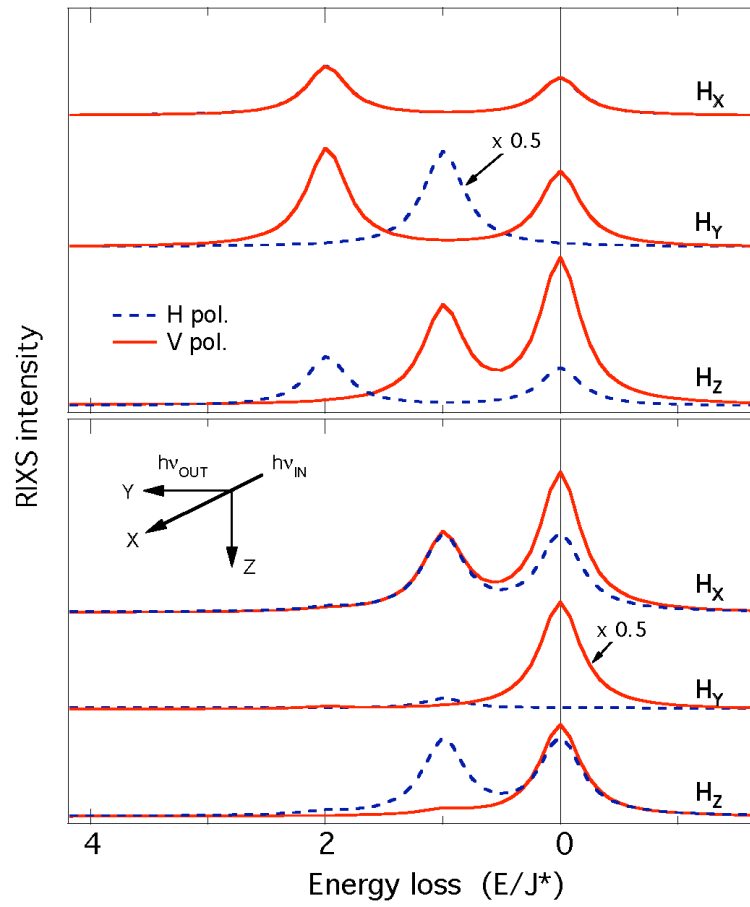


Figure 3.4: Calculated local spin flip RIXS spectra. Lower and upper panels correspond to peak and satellite excitations. $H_{x,y,z}$ are the magnetic momentum applied along the octahedron axes.

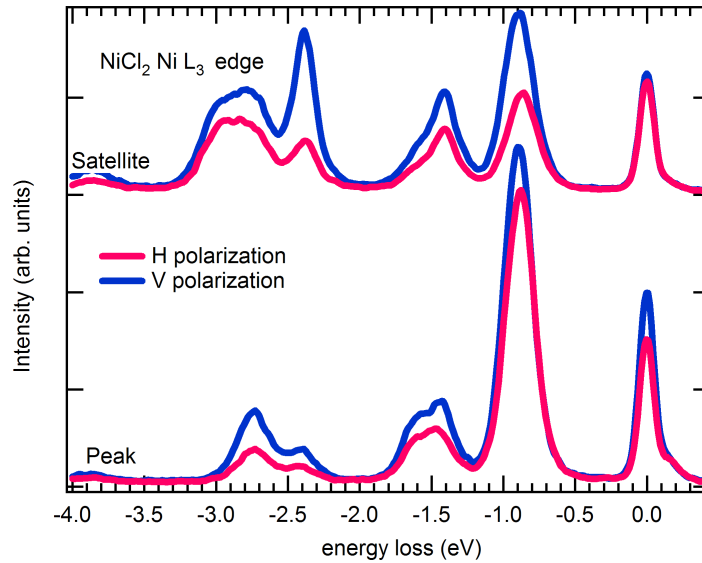


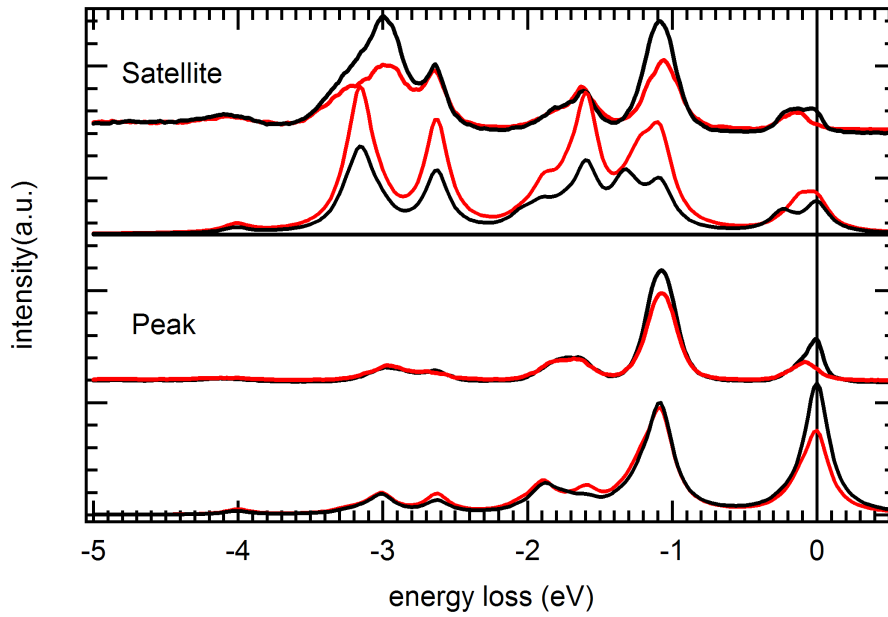
Figure 3.5: RIXS spectra of NiCl_2 measured at peak and satellite excitations.

central atom. Within a crystal field model, this translates into a smaller crystal field parameter. The smaller metal-ligand overlap leads to smaller superexchange interactions in NiCl_2 . As a consequence, NiCl_2 and NiO have quite different Néel temperatures of 52 K and 523 K respectively. In NiCl_2 the effective inter-atomic exchange has been estimated by inelastic neutron scattering measurements to ~ 13 meV [52], a value that is much smaller than our experimental resolution. Therefore NiCl_2 represents a crucial test for the confirmation of the spin flip nature of the observed low-energy losses, which we have tentatively assigned in NiO to the transition to $m_s=0, +1$ states of the ${}^3A_{2g}$ symmetry. If the peak has the same origin, in NiCl_2 it should be found in correspondence of a few meV energy loss, and it could not be experimentally separated from the elastic peak. That is indeed what happens in our experimental measurements which are reproduced in Figure 3.5. Apart from a small tail on the high-energy side, which is due to a small amount of scattered radiation inside the spectrometer, the elastic peak is symmetric for both excitation energies and polarizations, with no hint of satellites as in NiO .

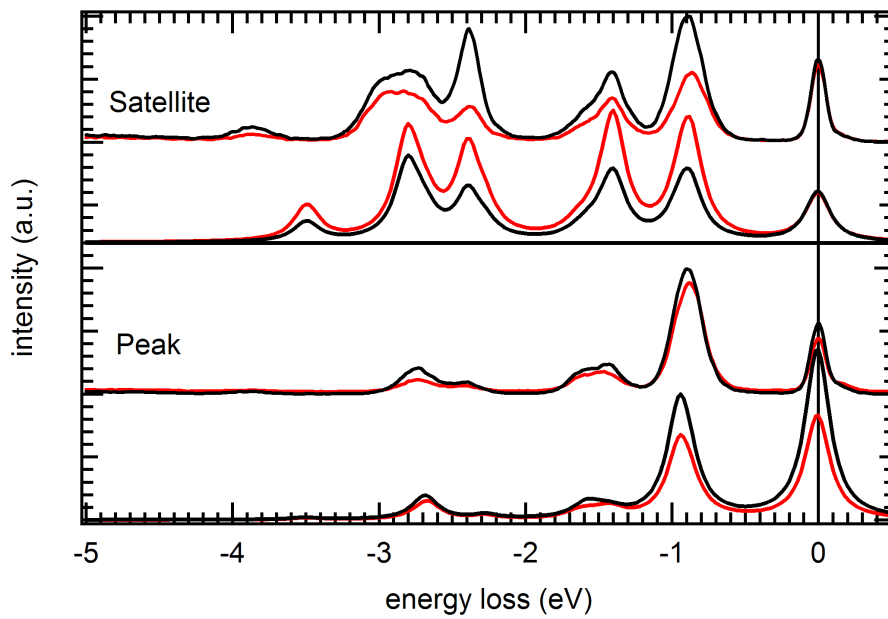
3.1.3 Crystal field model calculations

The interpretation of the experimental data was made using single ion simulation within a crystal field model [49], considering only the $3d^8$ configuration. The $3d^8 \rightarrow 2p^5 3d^9 \rightarrow 3d^8$ transition was processed for an undistorted octahedral site, neglecting the charge transfer excitations. The addition of an external exchange field lowers the local symmetry from O_h to C_{4h} . The same scattering setting used in the experiment was reproduced in the calculation. To simulate in a simple way the multi-domain nature of the sample, a set of three independent orientations of the incident radiation along the three axes have been considered, with polarization perpendicular or in the scattering plane. In addition, since no polarization analysis is performed on the scattered beam in the experiment, a sum of the calculated spectra over the two orthogonal polarizations was performed in correspondence of a 90° scattering angle. The spectra shown in Figure 3.6 were calculated by introducing Lorentzian lifetime broadening in the intermediate and final states equal to 200 and 100 meV, respectively. The calculations well reproduce the manifold of dd excitations experimentally observed in the region between 0 and 4 eV. Of course, they cannot account for the charge-transfer excitations at higher energy, which could on the contrary be well described by an Anderson impurity model calculation [47].

Clearly the spin flip features appear for excitation energy in correspondence of the absorption spin flip satellite, and their position is at $\sim J$ and $\sim 2J$. Whereas, for L_3 peak excitation energy the spin flip components are weaker. As expected, no spin flip features are observed in NiCl_2 . The optimal $10Dq$ parameter was determined from the position of the first energy loss. The effective values of the Slater Integrals calculated with the Hartree-Fock method are satisfactory only for isolated atoms. In the case of solids, in fact, the hybridization with the neighboring atoms originates a non-integer $3d$ population and hence reduced values of Slater Integrals. An estimation of the Slater Integral values was determined from the position of the 3 eV energy loss feature. From the direct comparison between



(a) NiO



(b) NiCl₂

Figure 3.6: Comparison between the calculated ionic model results and the experiment in the dd excitation region, for NiO(a) and NiCl₂(b). In each panel the experimental results are given by the upper curves.

experimental and calculated spectra, for both NiO and NiCl₂, the optimal $10Dq$ parameters were respectively set to 1.085 eV and 0.91 eV, and the Slater Integrals were reduced to 61% and 59% of their atomic values. An exchange field (H_{exch}) equal to 125 meV and 13 meV was added respectively for NiO and NiCl₂.

3.1.4 Angle dependence

We also explore the dependence of the spin flip excitations on the scattering angle, by rotating SAXES spectrometer in the horizontal plane around the sample position, which translates into different values of the transferred momentum, q . The momentum dependence should highlight the dispersion of the magnetic excitations which I have so far assumed to be local, for simplicity and to allow a direct comparison with the theory. The results are displayed in Figure 3.7 for these scattering angles, 50°, 90° and 130°, corresponding to transferred momenta equal to $q=0.36 \text{ \AA}^{-1}$, $q=0.61 \text{ \AA}^{-1}$, and $q=0.78 \text{ \AA}^{-1}$. The spectra have been normalized to the first energy loss. Essentially there is no difference in the near elastic excitations except for the fact that the elastic peak is stronger in the forward scattering geometry, where an accurate determination of the satellite position is very difficult. Nevertheless, the magnetic excitations do not appear to disperse. Unfortunately the $q=0.61 \text{ \AA}^{-1}$, and $q=0.78 \text{ \AA}^{-1}$ values for which the satellite position can be accurately determined are almost symmetrically located around the zone boundary, and the corresponding magnon energies are anyway very similar [53].

At this stage, however, one cannot exclude the possibility that the RIXS transition is accompanied by the creation of phonons which would randomize the momentum transferred to the magnons. In this case, only a q -averaged density of magnon states, with a peak energy corresponding to the flat part of the magnon dispersion near the zone boundary, at around 110 meV, and a replica at twice that energy would be observed in the RIXS spectra. More accurate data are clearly necessary to clarify this point.

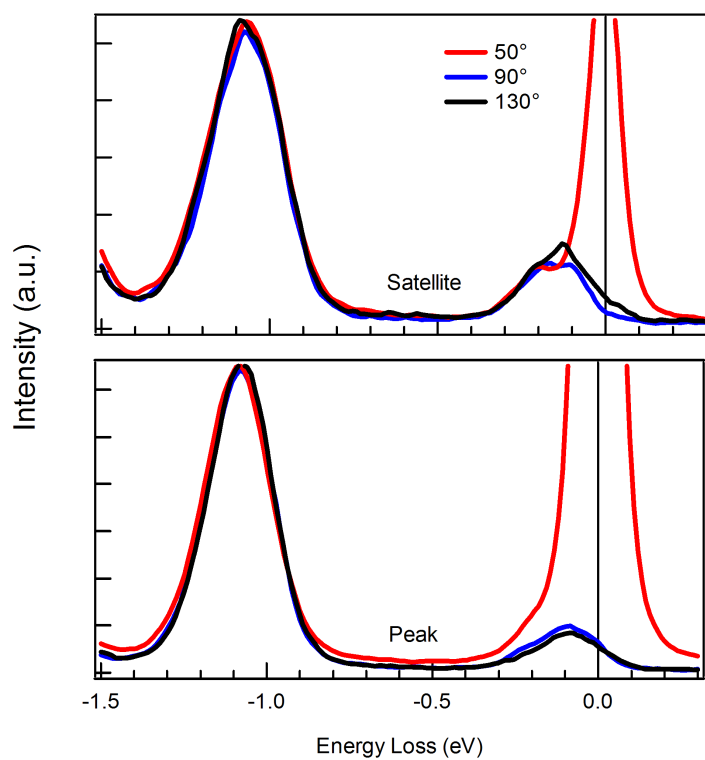


Figure 3.7: Scattering angle dependent RIXS of NiO measured with LH polarized light at peak (bottom) and satellite (top) excitations.

3.2 O K edge

At the oxygen K edge, narrower linewidth can be more easily achieved compared to L_3 edge due to the smaller (530 eV) energy. It was first demonstrated in cuprate systems, where it was possible to separately identify the dd excitations, a Zhang-Rice singlet excitation in addition to charge transfer excitations [54]. The first application to NiO was performed by Anisimov [55] where O K RIXS gave accurate information about the valence band structure. Recently Duda *et al* [56] observed rich features of charge transfer and dd excitations with higher resolution.

Our O K RIXS results are summarized in Figure 3.8. The O $1s$ absorption spectrum measured in the total electron yield mode is shown in Figure 3.8a. The excitation energy labeled A corresponds to the peak of the sharp edge feature, while B and C are ~ 1 eV below and above the maximum respectively. The RIXS spectra collected for these 3 excitation energies with LH and LV polarized light, are displayed in Figure 3.8b. The spectra above 4 eV resemble previous data, and are dominated by the charge transfer excitations. The feature at 4.1 eV energy loss was assigned to non-local charge transfer excitation, which involves two Ni sites.

However in the 2 to 0 eV region, with a magnified view in Figure 3.9, the features have been resolved much better thanks to our instrument improvements. Two groups of features at 1 eV and 1.6 eV are identified, and their positions are consistent with their counterparts in Ni L_3 edge, see Figure 3.1. Therefore, they are naturally assigned to dd excitations as pointed out by Hufner [57]. Although this does not exclude that a double singlet creation can [56] coincide at the same energy, its intensity contribution needs to be verified by further studies.

Moreover we observed low energy excitations near the elastic peak. Due to the low statistics, the peak positions are not well defined. Nevertheless the feature within 200 meV loss can be safely assigned to the local spin-flip excitation. The other weak feature at 300 meV shows as a broader tail in the low energy side whose existence needs to be confirmed with better statistics, marked by black arrows in Figure 3.9.

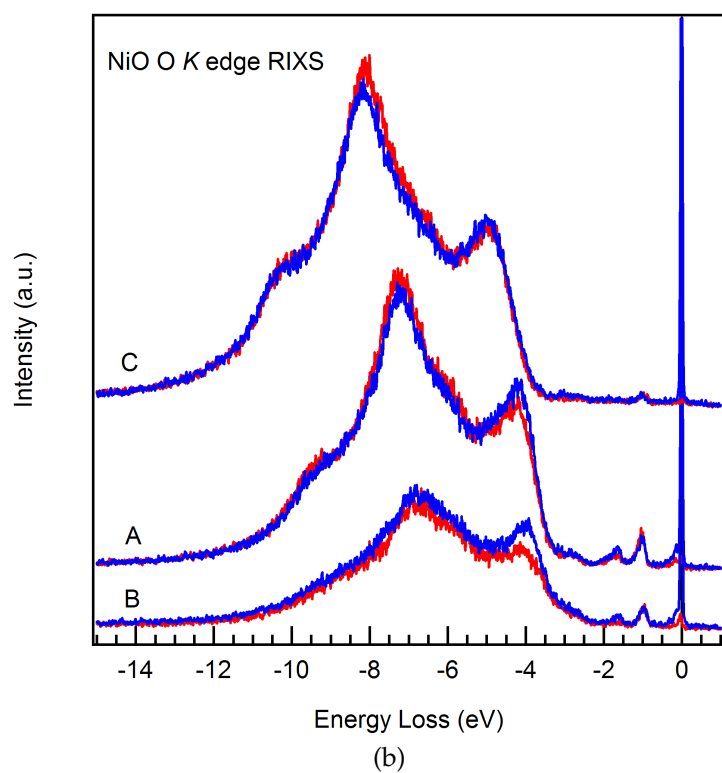
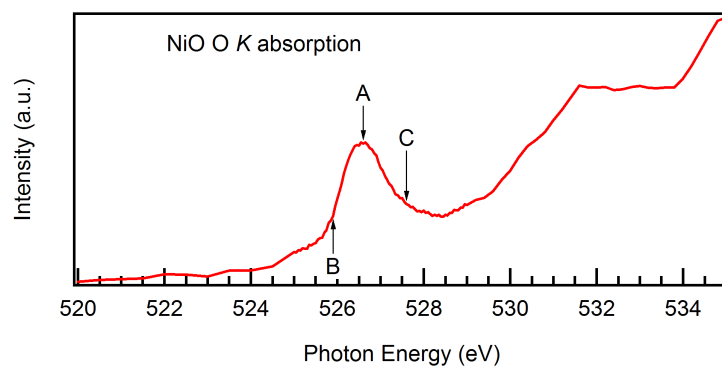


Figure 3.8: (a) O *K* XAS spectra with excitation energies labeled. (a) O *K* RIXS measured at the absorption resonance (A) and $\sim 1\text{eV}$ below (B) and above (C).

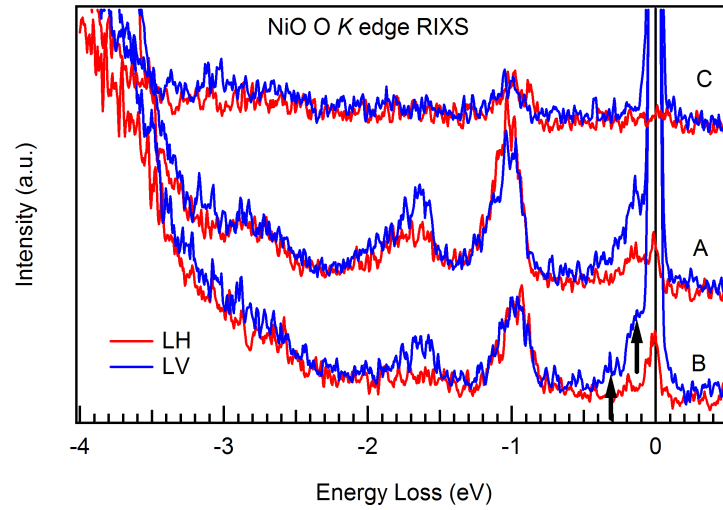


Figure 3.9: O K RIXS spectra magnified in the dd excitation region.

3.3 Ni $M_{2,3}$ edge

Before the commissioning of SAXES, the energy resolution which could be obtained with grating monochromators operating in the extreme VUV was considerably better than the corresponding resolution available at the L edge. To take advantage of this, we performed a RIXS experiment on NiO at Ni $M_{2,3}$ edge ($3p \rightarrow 3d$; $h\nu=65$ eV). The energy positions of the dd transitions measured with this method are consistent with those found with RIXS at the L_3 edge. But the dominating contribution of the recombination peak (elastic scattering) and thus the low signal-to-noise ratio obscures most of the dd excitations below 0.5 eV. Therefore the information of the local spin flip excitation is retrieved by analyzing the shape change of the ${}^3T_{2g}$ state. Nevertheless this experiment, for the first time, provides an unambiguous identification of the dd excitations of NiO by means of RIXS.

Localized Electronic Excitations in NiO Studied with Resonant Inelastic X-Ray Scattering at the Ni M Threshold: Evidence of Spin Flip

S. G. Chiuzbăian,^{1,*} G. Ghiringhelli,² C. Dallera,² M. Grioni,³ P. Amann,^{1,†} X. Wang,³ L. Braicovich,² and L. Patthey¹

¹Paul Scherrer Institut, CH-5232 Villigen PSI, Switzerland

²INFN-Dipartimento di Fisica, Politecnico di Milano, p. Leonardo da Vinci 32, 20133 Milano, Italy

³IPN, Ecole Polytechnique Fédérale, CH-1015 Lausanne, Switzerland

(Received 24 February 2005; published 31 October 2005)

We studied the neutral electronic excitations of NiO localized at the Ni sites by measuring the resonant inelastic x-ray scattering (RIXS) spectra at the Ni $M_{2,3}$ edges. The good energy resolution allows an unambiguous identification of several spectral features due to dd excitations. The dependence of the RIXS spectra on the excitation energy gives evidence of local spin flip and yields a value of 125 ± 15 meV for the antiferromagnetic exchange interaction. Accurate crystal field parameters are also obtained.

DOI: [10.1103/PhysRevLett.95.197402](https://doi.org/10.1103/PhysRevLett.95.197402)

PACS numbers: 78.70.Ck, 71.27.+a, 75.30.Et, 78.70.Dm

Determining the nature of the electronic states in strongly correlated materials is a prerequisite to understanding their rich and intriguing physical properties, including magnetism and high T_c superconductivity. Photoemission (inverse photoemission) can directly probe the electron removal (addition) spectral function, but *neutral* excitations like the dd excitations in the $3d$ transition metal ($3d$ TM) oxides and related materials require a different approach. Such atomlike excitations, which correspond to a local rearrangement of the $3d$ electrons, play a crucial role in many properties of these materials, and carry important information on magnetic interactions. They were traditionally the domain of optical absorption and electron energy loss experiments. More recently, however, it was shown that resonant inelastic x-ray scattering (RIXS) [1] also probes dd excitations, with the distinctive advantages of a resonant spectroscopy although the resolution has been a limiting factor. Here we present RIXS data having good resolution and measured at the Ni M edge ($3p$) of the benchmark compound NiO, and identify magnetic excitations probed with RIXS in an independent and complementary way to neutron studies. In RIXS, the resonant absorption of a photon by a core electron leads to a radiative deexcitation which leaves the system either in its ground or in a neutral excited state [1,2]. Thus dd excitations—including excitations of magnetic interest—yield characteristic spectral losses dispersing with incident photon energy (Raman regime) and information is projected on the cation site [3,4]. In RIXS studies the L edges have been more commonly employed mainly because the scattering cross section is much higher and the $2p$ spin-orbit splitting is larger than at M edges. However, the instrumental linewidth is much broader at L edges. Only recently Ghiringhelli *et al.* [5,6] have effectively used L_3 RIXS to study dd excitations with an instrumental bandwidth considerably smaller than 1 eV. In contrast, M RIXS, despite the first impressive demonstration by Kuiper *et al.* [7], was seldom used in recent years, and then only at the Cu edge to the authors' knowledge [8].

We have thus exploited an energy resolution down to 130 meV in the range 65–72 eV (RIXS at the M edge of Ni) to study the neutral local electronic excitations of NiO. The interest of the study is not only in the paradigmatic importance of this compound and in the precise location of the spectral features allowed by the increased resolution, but in more fundamental aspects. In fact, we were able to address the local spin-flip excitations at the Ni-site in the final state of RIXS. By spin-flip excitations we refer here to transitions involving a change in the orientation of the local spin moment on Ni cation sites with respect to the orientation of spin moments on neighboring sites [9]. This idea, put forward by de Groot *et al.* [10] with a theoretical estimate for the L edge, has never been implemented experimentally to the authors' knowledge, probably due to the difficulty of the experiment. We note that: (i) the spin-flip transitions cannot be observed in direct optical absorption within the $3d$ -manifold in the infrared and in the visible [11] where these transitions are strongly suppressed; (ii) the spin-flip transitions can indeed be seen in electron energy loss spectroscopy [12], basically in a surface sensitive mode; RIXS, even at low energies, is much more bulk sensitive so that it adds new relevant information; (iii) up to now, this information has been obtained indirectly by modelling the dispersion of spin waves [13]; the present paper gives a complementary approach to neutron spectroscopy.

Another result of the present work is the accurate determination of the crystal field parameters needed to describe the Ni-atom site. This is much easier in these accurate measurements than in cases having larger energy linewidths at the L edges as in Refs. [14–16]. In the following, the crystal field parameters are the best values in a single ion model having octahedral symmetry without hybridization to the ligand and with a single configuration ($3d^8$ in this case). This is the traditional way of defining the parameters in the crystal field approach, as found commonly in the literature on $3d$ TM compounds. Thus, our values are directly comparable to the literature without the

need of renormalizing for interaction with the surroundings of the ion. NiO has been considered to be prototypical among the strongly correlated systems for the difficulties involved in the understanding the nature of its gap [17,18]. Below $T_N = 523$ K, NiO exhibits antiferromagnetic ordering with the spin moments along the $\langle 11\bar{2} \rangle$ directions. The sample was a single crystal NiO(100) cleaved in air and oriented in a vertical plane at 25° grazing incidence. The scattered photons were detected at 90° from the incident beam. The measurements were carried out at the SIS beamline (Swiss Light Source) [19,20] at room temperature and 2×10^{-10} mbar base pressure, using linearly polarized light, with the polarization in the horizontal plane (resolving power $E/\Delta E \cong 3000$ for an exit slit opening of $200 \mu\text{m}$). The scattered light was recorded with a Rowland-circle grazing incidence spectrograph [21] with a 300 lines/mm grating (3 m Rowland radius) and entrance slit set to $30 \mu\text{m}$. It took about 20–30 min or several hours to record a RIXS spectrum with the first and second diffraction order of the grating, respectively.

The soft x-ray absorption spectrum (XAS) at the M threshold (Fig. 1) was recorded by monitoring the sample drain current and by normalizing to the reference current taken from a gold mesh. The measured XAS is in good agreement with the previously reported data [22,23]. The two main features with maxima around 66.7 and 70.0 eV are atomic multiplet rather than spin-orbit split peaks [24].

The RIXS spectra measured with several excitation energies at the Ni M edge (shown by bars in Fig. 1) are presented in Fig. 2 versus the energy transferred to the sample $h\nu_{\text{in}} - h\nu_{\text{out}}$ (combined resolution 200 meV) while Fig. 3 gives two spectra with higher resolution (130 meV), obtained with the second order of the spectrograph past the sample. Before any interpretation the results deserve the following comments: (i) The spectra are dominated by the elastic peak (feature A) (see Figs. 2 and 3) and the inelastic features (B–D) are seen only by drastically expanding the spectra. This is analogous to what was seen by Kuiper *et al.* in $\text{Sr}_2\text{CuO}_2\text{Cl}_2$ [7] and shows the need for a high-resolution and flux beamline. (ii) All inelastic peaks disperse with the

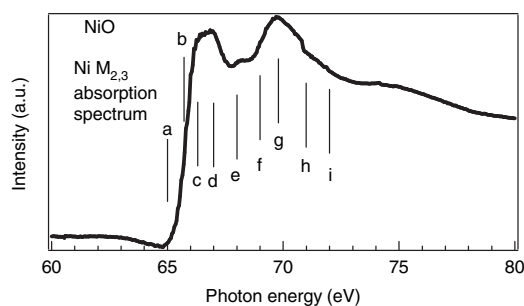


FIG. 1. Total electron yield XAS spectrum recorded across the M threshold of Ni in NiO. The excitation energies used for the RIXS spectra are indicated with lines and denoted with small letters.

excitation energy also well above the threshold. This is at variance with the behavior at the L edge where RIXS shows also fluorescence and charge-transfer excitations when exciting a few eV above the threshold [14,15]. Thus, the extensive Raman behavior makes M RIXS very useful to study localized excitations. (iii) The evolution of the relative spectral weights with the incident energy across the resonance shows that feature B dominates at lower energies while across the resonance the intensity of feature C becomes sizable. (iv) Fig. 2 shows that the center of gravity of feature B is slightly dependent on the excitation energy across the resonance; the maximum shift (about 60 meV) is reached with 66.3 eV photons. (v) In the higher resolution measurements of Fig. 3, the feature C in the spectrum at 68.2 eV is clearly not a single peak. In the expanded view of peak C in the inset of Fig. 3, this feature (red dots) is well fitted by two components with a separation of 170 meV (the line shape is taken from the elastic peak, giving the instrumental response with a further Lorentzian broadening of 50 meV). The double nature of the peak appears at resonance and is not found below resonance, as shown by the spectrum with excitation (b) (blue triangles).

As anticipated above, the spectral features are assigned with the use of a crystal field approach. The transferred energy corresponds to the excitation of the system in the final state. Thus the assignments simply require the comparison with the low energy excitations of the system. The positions of all peaks are well explained by the dd excita-

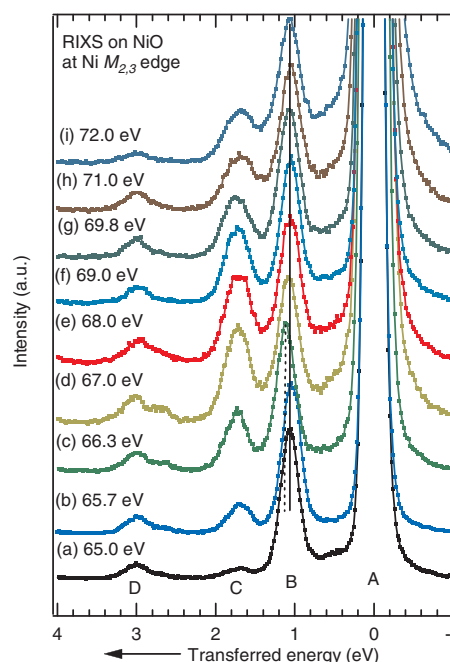


FIG. 2 (color). Energy-dependent RIXS spectra measured at the Ni $M_{2,3}$ resonances in NiO. All spectra are normalized to the intensity of the first loss.

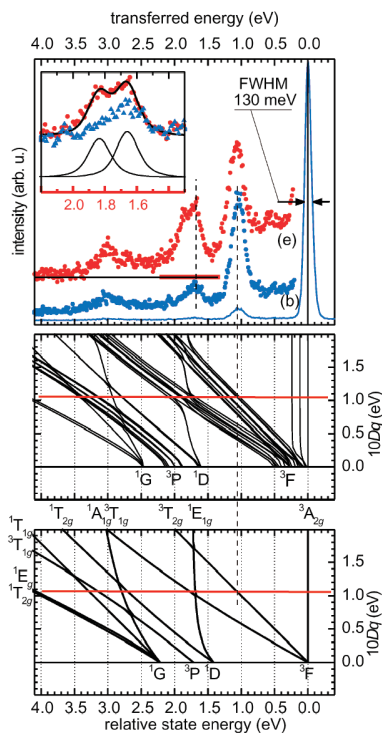


FIG. 3 (color). Upper panel: High energy resolution spectra taken with the second order of the spectrometer at the excitation energies (b) and (e) (see Fig. 1). The inset gives an expansion of the spectra in the region marked by the red horizontal bar [(e) in red dots and (b) blue triangles]. The spectrum (e) is decomposed in two components whose sum is the heavy black line. The two lower panels give the Sugano-Tanabe diagrams versus crystal field $10Dq$ (see text).

tions, confirming that we do not see charge-transfer excitations. We optimized $10Dq$ (which measures the energy distance between e_g and t_{2g} states in octahedral symmetry) in the calculation of the dd neutral excitations (final states in the scattering) with the COWAN code [25] plus a crystal field with a rescaling to 70% of the Slater integrals to account for intra-atomic correlation beyond the Hartree-Fock scheme. The results are collected versus $10Dq$ in the bottom of Fig. 3 (Sugano-Tanabe diagrams [26]) without (lower panel) and with spin-orbit and exchange (120 meV, a reasonable value as shown below). The figures also give the symmetry labels. The optimal value obtained by comparing with the values without exchange is $10Dq = 1.05$ eV. This is particularly clear from the first loss B corresponding to the dd transition ${}^3A_{2g} \rightarrow {}^3T_{2g}$, at energy $10Dq$. With exchange the Sugano-Tanabe diagrams give a manifold of lines (see central panel of Fig. 3) in place of a single line, so that the spectra have a detailed structure giving information on the exchange. The spectral intensities of these components are determined by the selection rules in the scattering, by the transition matrix elements, and by the interference between scattering paths. The

discussion of the detailed structure requires calculations of the spectral functions with the Kramers-Heisenberg formula [27].

An illuminating set of theoretical spectra at various excitation energies is given in Fig. 4 obtained with the above parameters and with an exchange of 120 meV, with lifetime broadening in the intermediate state of 1 eV [28] and 50 meV in the final state (without including the instrumental broadening, for clarity). The magnetization and the photon incidence are along the octahedral axis (C_{4h} symmetry). The scattering geometry and the incident photon polarization are as in the experiment. The figure is the M edge analogous to calculations by de Groot *et al.* for the L_3 edge [10]. The spectral functions are calculated either not including (red lines) or including (heavy black lines) the interatomic exchange interaction, in order to highlight the new structures related to the spin-flip excitations. These are satellites (marked by arrows in Fig. 4) at higher transferred energy due to the energy cost of local spin flip on the cation site. The satellites resonate at certain incident energies so that their effect is expected to be seen in the experiment as a modification of the spectra at increasing energy across the resonance. This is due to the fact that distinct incident energies select different intermediate states thus leading to different weights in the final states. The region A near the elastic peak (and looking very promising from Fig. 4) cannot be used because in the experiment this region is submerged by the tail of the huge elastic (Rayleigh) peak. A reliable decomposition of the measured spectra seems unrealistic. On the other hand, there are two pieces of evidence for spin flip discussed here in order of increasing importance: (i) In region B at resonance there is a clear spin-flip satellite basically separated by one exchange from the main peak. A simulation of the experiment, taking into account the instrumental linewidth, is shown in the inset of Fig. 4 giving

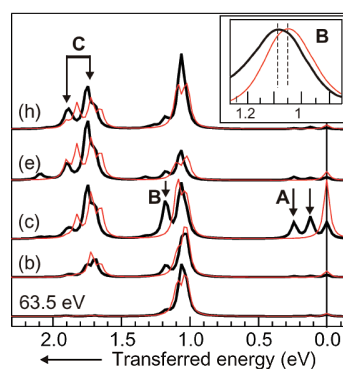


FIG. 4 (color). Theoretical RIXS spectra excited at the energies 63.5 eV, (b), (c), (e) and (h) (see Fig. 1). The spectra without exchange interaction are given by the red line and those with exchange by the heavy black line. The inset gives the expected shape of feature B in case (c) by accounting for the experimental band-pass.

an expanded view of region B. Although the resolving power is not sufficient to see the satellite, a clear shift of the peak at resonance is the consequence of the spin flip as is indeed the case in the experimental results. As stressed above, the experiment shows a shift across resonance (see Fig. 2), which is qualitative evidence for local spin flip, compatible with an exchange between about 80 and 150 meV. In the inset, the simulation takes approximately into account the multidomain structure of the sample with an average of spectra with different orientations between the x rays and the magnetization. (ii) More quantitative is the analysis of region C at resonance and above. In the theoretical spectra there are basically two main features whose separation is greater than the exchange and increases with the magnitude of the considered exchange. Thus it is easier to resolve experimentally the two peaks in region C than in the region B. This is indeed the case and we have already shown that feature C in the high-resolution spectra has two components separated by 170 meV (inset of Fig. 3). This separation is accurately fitted in the high-resolution spectrum with excitation e . With the constraint of keeping the $10Dq$ value already obtained from the positions of the spectral features we derive an exchange of 125 ± 15 meV (the 120 meV used in all preceding figures can hardly be distinguished from this value). The result is a rather direct measurement based on RIXS. Strong support for this analysis comes from the fact that in the experiment the satellite resonates and is basically suppressed below resonance, as shown by the inset of Fig. 3. This trend is also found in our calculations.

The exchange has been obtained in a scheme based on a pure crystal field without hybridization with the ligand band. The renormalization of the exchange due to this effect should be very small, making our estimate very reliable. In fact we use a separation between two nearby spectral features that would be renormalized basically in the same way, because both spins are present almost with the same weight in the ligand band. The present value compares well with the value of 114 meV obtained from spin-wave analysis [13]. This demonstrates the consistency between the two approaches and shows that future high-resolution RIXS will be very useful in the study of exchange effects. Note that this is a local probe not requiring macroscopic magnetization and also working in antiferromagnetic systems as in our case.

In conclusion, we have presented RIXS measurements at the M edge of Ni in NiO, which shows that high quality data can now be obtained despite the very low cross section. This not only allows a precise location of the spectral features and the accurate tuning of the parameters in theoretical models, but also gives direct experimental access to exchange effects. The present approach gives a cross fertilization with the work based on neutron scattering.

The work was performed at the Swiss Light Source, Paul Scherrer Institut, Villigen, Switzerland. The technical support provided by J. Krempaski and F. Dubi is gratefully acknowledged. L.B., C.D., and G.G. are grateful to R. Gusmeroli and to F. Fracassi for the help with the computational part.

*Electronic address: gheorghe.chiuzbaian@psi.ch

†Currently at Institut für Experimentalphysik, Leopold Franzens Universität, 6020-Innsbruck, Austria.

- [1] A. Kotani and S. Shin, *Rev. Mod. Phys.* **73**, 203 (2001).
- [2] J.-E. Rubensson *et al.*, *Appl. Phys. A* **65**, 91 (1997).
- [3] S. Tanaka and A. Kotani, *J. Phys. Soc. Jpn.* **62**, 464 (1993).
- [4] S. M. Butorin *et al.*, *Phys. Rev. B* **54**, 4405 (1996).
- [5] G. Ghiringhelli *et al.*, *Phys. Rev. Lett.* **92**, 117406 (2004).
- [6] See also the report of a study at Mn L edges with 0.3–0.35 eV combined experimental linewidth, at URL <http://www.esrf.fr/NewsAndEvents/Spotlight/spotlight9SoftRIXS>.
- [7] P. Kuiper *et al.*, *Phys. Rev. Lett.* **80**, 5204 (1998).
- [8] L.-C. Duda *et al.*, *Surf. Rev. Lett.* **9**, 1103 (2002).
- [9] To be distinguished from intra-atomic spin-flip transitions which account for the flip of a single electron spin and imply a change in multiplicity (see for example J.-J. Gallet *et al.*, *Phys. Rev. B* **54**, R14238 (1996).)
- [10] F. M. F. de Groot *et al.*, *Phys. Rev. B* **57**, 14 584 (1998).
- [11] M. Fiebig *et al.*, *Phys. Rev. Lett.* **87**, 137202 (2001).
- [12] B. Fromme, *d-d Excitations in Transition Metal Oxides* (Springer Verlag, Berlin, 2001), and the references therein.
- [13] M. Hutchings and E. Samuelsen, *Phys. Rev. B* **6**, 3447 (1972).
- [14] H. Ishii *et al.*, *J. Phys. Soc. Jpn.* **70**, 1813 (2001).
- [15] M. Magnuson *et al.*, *J. Phys. Condens. Matter* **14**, 3669 (2002).
- [16] G. Ghiringhelli *et al.* (unpublished).
- [17] G. Ghiringhelli *et al.*, *J. Phys. Condens. Matter* **17**, 5397 (2005).
- [18] O. Tjernberg *et al.*, *Phys. Rev. B* **53**, 10 372 (1996).
- [19] T. Schmidt *et al.*, *Nucl. Instrum. Methods Phys. Res., Sect. A* **467**, 126 (2001).
- [20] U. Flechsig *et al.*, *Nucl. Instrum. Methods Phys. Res., Sect. A* **467**, 479 (2001).
- [21] J. Nordgren and R. Nyholm, *Nucl. Instrum. Methods Phys. Res., Sect. A* **246**, 242 (1986); we used the commercial model XES-350 produced by Gammadata (Sweden).
- [22] F. Brown *et al.*, *Solid State Commun.* **9**, 487 (1971).
- [23] M. R. Thuler *et al.*, *Phys. Rev. B* **27**, 2082 (1983).
- [24] G. van der Laan, *J. Phys. Condens. Matter* **3**, 7443 (1991).
- [25] R. Cowan, *The Theory of Atomic Structure and Spectra* (University of California Press, Berkeley, 1981).
- [26] S. Sugano *et al.*, *Multiplets of Transition Metal Ions in Crystals* (Academic Press, New York and London, 1970).
- [27] J. Sakurai, *Advanced Quantum Mechanics* (Addison-Wesley, Reading, MA, 1967).
- [28] O. Keski-Rahkonen and M. O. Krause, *At. Data Nucl. Data Tables* **14**, 139 (1974).

Chapter 4

Mn and Cu compounds

4.1 MnO

Like NiO, the electronic structure of MnO has been a subject of investigation for many years through various techniques. It has a formal configuration of $\text{Mn}^{2+}, 3d^5$, exhibiting a rich spectral structure due to the local electronic excitations. In the commissioning phase of SAXES, it was chosen for similar reasons as stated in [58], to push ahead the accuracy limit of the electronic excitations thus demonstrating the instrument resolving power, and at this new accuracy level to evaluate the existing theoretical interpretations.

The sample is a MnO single crystal, cleaved in air before introducing into the vacuum chamber, kept at room temperature during the measurements.

Figure 4.1 inset shows the $L_{2,3}$ absorption spectrum, measured in total electron yield, where the chosen excitation energies are labeled to be consistent with [58, 59]. The RIXS spectra are plotted by the energy loss scale in Figure 4.1. Each spectrum is corresponding to an acquisition time of 2 hours. The photon energy is varied across the $L_{2,3}$ edge for two linear polarizations, LH (in the scattering plane) and LV (perpendicular to the scattering plane). The elastic peak is not shown. The broad feature above 6 eV is from the charge transfer excitations. It develops and become more

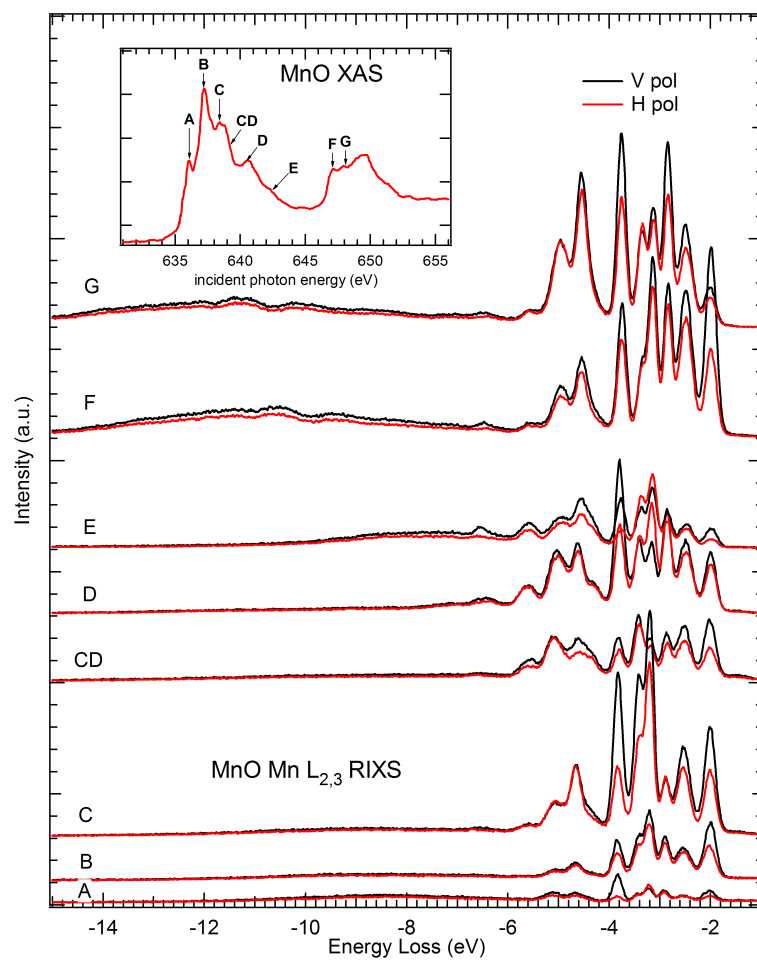


Figure 4.1: MnO Mn L_3 RIXS spectra across $L_{2,3}$ edge with LH and LV polarized light, ordered by excitation energies from bottom up. Inset: XAS at Mn $L_{2,3}$ edge labeled with selected excitation energies.

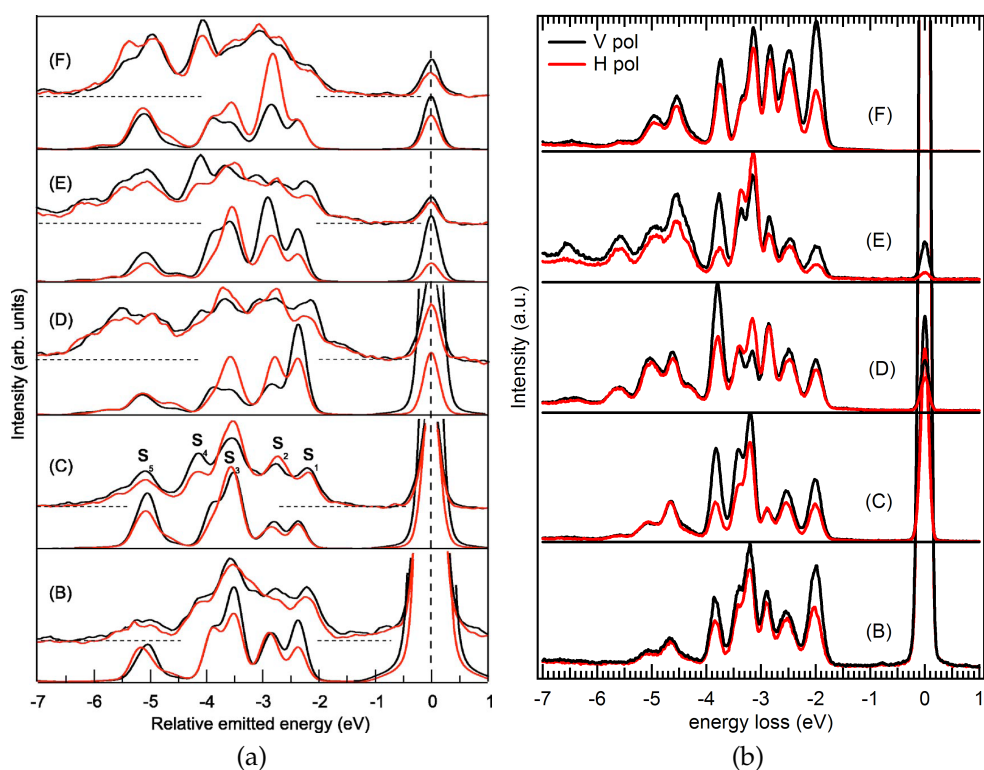


Figure 4.2: Comparison of MnO Mn L_3 RIXS spectra in the dd excitation region, between results in Reference [58](a) and ours ((b)). (a): Comparison between the calculated Anderson model results and the experiment. In each panel the experimental results are given by the upper curves. (b): High resolution spectra taken at SAXES.

visible with increasing excitation energy above threshold. At the highest excitation energies (F, G) it is significantly masked by the overlapping contribution from the normal fluorescence.

The rich features in the 1 to 6 eV region are due to the dd excitation origin. In general these features are much sharper than in previously published data and new peaks can be identified thanks to the much better resolution of SAXES (180 meV), compared to the previous value of 320 meV in [58], shown side by side in Figure 4.2. These high resolution data show a visible discrepancy with the theoretical calculation performed (Figure 4.2a, lower curves in each panel), in the aspect of feature position, rel-

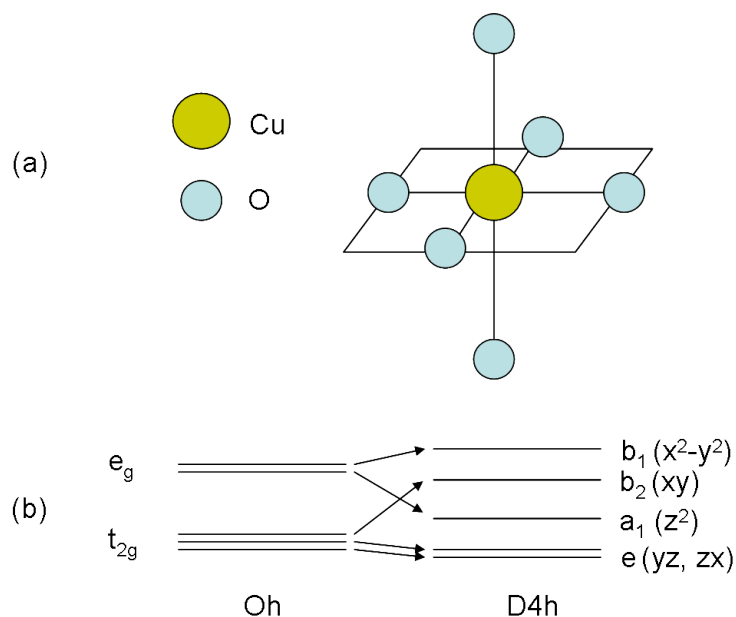


Figure 4.3: (a) D_{4h} symmetry representation. (b) Cu 3d orbitals energy level diagram in O_h and D_{4h} symmetries.

ative intensity and polarization dependence. These differences challenge the accuracy of the existing impurity model calculation. The fine tuning of the parameters, including full multiplet effects, could provide more understanding of the strong correlation nature.

4.2 CuO and malachite

The CuO sample was prepared by compressing CuO powder onto an indium foil and it has a macroscopically smooth surface. The malachite sample is a natural mineral ($\text{CuCO}_3\text{Cu}(\text{OH})_2$) with a shiny surface. The experimental setup (grazing incidence), was optimized to minimize the self-absorption, which strongly reduces the elastic peak of the spectra excited at the peak of the L_3 absorption.

In these two samples, the Cu atom is known to have formal divalent configuration $3d^9$, meaning only one hole in the $3d$ shell. The local symmetry is assumed to be D_{4h} (tetragonally distorted octahedron) as shown

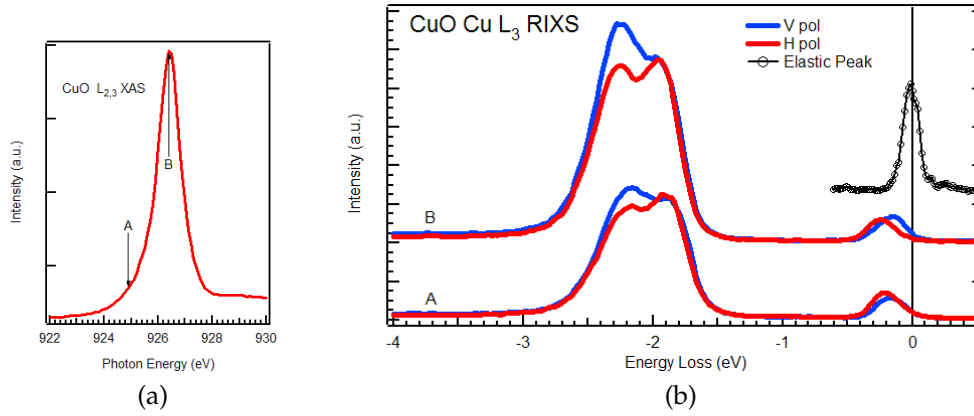


Figure 4.4: (a): X-ray absorption spectrum of CuO at L_3 edge. A and B mark the chosen excitation energies. (b): RIXS spectrum taken at excitation points A and B with LH and LV polarized light, compared with elastic scattering reference (black open circles).

in Figure 4.3(a). This results in the ordering of Cu $3d$ crystal field orbitals as shown in Figure 4.3(b). The in-plane oxygens are the Cu nearest neighbors, forcing the $3d$ hole to have the $x^2 - y^2$ symmetry in the ground state. For CuO, there are no apical oxygen atoms, which reduces the energy of orbital z^2 relative to xy .

Figure 4.4a shows the $L_{2,3}$ absorption spectrum measured in total electron yield. It has one strong peak as common to divalent (Cu^{2+}) [60], which is well understood: one electron from $2p_{3/2}$ is excited to fill the only $3d$ hole. In Figure 4.4b the RIXS spectra for two selected excitation energies are presented. The main peak around 2 eV can be assigned to the dd excitations. It clearly shows two components which could not be resolved before. By referring to the energy level diagram of Figure 4.3, the features at 1.9 eV are corresponding to final state in b_{2g} and the one at 2.2 eV has the origin from a_{1g} and e_g final states. The polarization dependence for these two features is remarkably different, the one at 2.2 eV shows a big polarization dependence while the other at 1.9 eV remains the same for both polarization.

The broad feature around 200 meV was assigned to the elastic peak

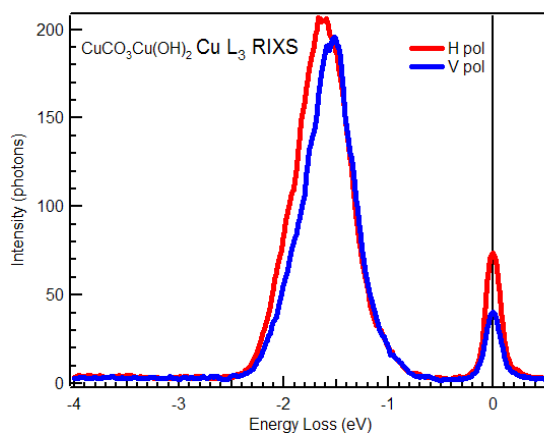


Figure 4.5: RIXS spectrum of Malachite measured with LH and LV polarized light excited at Cu L_3 absorption resonance.

in previous studies [61] due to limited resolution. We have now very carefully measured the elastic scattering from a carbon tape glued next to the sample and plot it together with the RIXS spectra (black curve in Figure 4.4b). This purely elastic spectrum gives the instrument resolving power without ambiguity. In this case the FWHM of the real elastic peak is 143 meV, which is significantly narrower than that of the low-energy feature in CuO. It also provides a convenient and nearly reliable energy reference and allows us to compensate possible time-dependent energy drifts of the primary beam. By alternately measuring elastic scattering and RIXS spectrum, we can precisely define the zero energy loss position in the RIXS spectrum. The comparison reveals the fact that the broad feature is due to some low energy excitations. We assign this loss to an excitation of magnetic nature as found in NiO sample (see Chapter 2). Its position also shows similar polarization dependence.

For comparison, the RIXS spectra from the malachite sample is shown in Figure 4.5. The dd excitation position has a ~ 0.5 eV shift towards high energy, reflecting its small crystal field splitting. The different final states are not as well resolved as in CuO. The most important difference is that the elastic peak is as narrow as elastic scattering from carbon tape, which means the absence of local spin flip excitation.

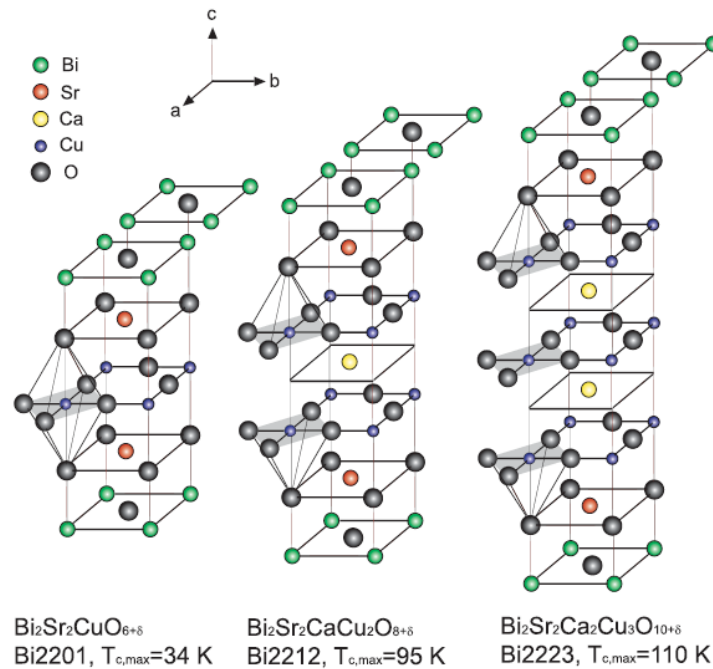


Figure 4.6: Crystal structure of BSCCO families and their critical temperatures.[62]

4.3 BSCCO

BSCCO is a family of high-temperature superconductors having the generalized chemical formula $\text{Bi}_2\text{Sr}_2\text{Ca}_n\text{Cu}_{n+1}\text{O}_{2n+6}$, where $n=0,1,2$, see Figure 4.6. Bi2201 has a critical temperature of 34 K, whereas Bi2212 and Bi2223 has T_c 95 K and 107 K respectively. The latter two critical temperatures are above the temperature of liquid nitrogen. Bi2212 is the first high-temperature superconductor to be used for making conducting wires. Needless to say, systematic measurements of the dd excitations and of any other low-energy neutral excitations (possibly related to magnetic correlations) are of great interest for a better understanding of these superconducting materials. Indeed there are pioneering experimental works to study high T_c cuprates by RIXS at the Oxygen K edge and Cu K , L_3 and $M_{2,3}$ edges [63, 64, 65, 61]. At the L_3 and $M_{2,3}$ edges, the RIXS processes involve direct transitions from and to the $3d$ states providing clear information on the

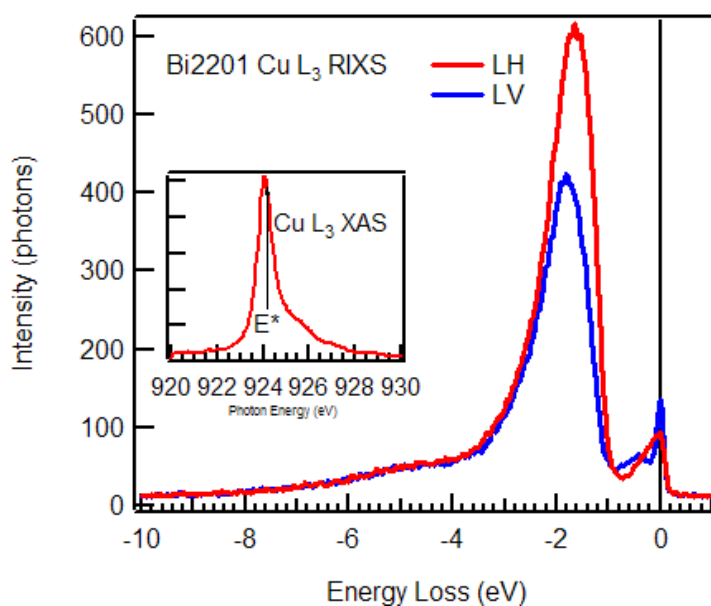


Figure 4.7: Bi2201 Cu L_3 RIXS spectra. The sample is kept at room temperature with surface near normal to the incidence beam. Inset: Cu L_3 absorption spectrum with excitation energy indicated.

charge transfer-, the dd -, and the magnetic excitations. L_3 edge RIXS could be more useful because of the large $2p$ spin-orbital splitting and high cross section. However due to limited instrumental resolution, this possibility has seldom be exploited.

In our measurements, the scattering angle between incident beam and spectrometer is fixed at 90° . The samples could be rotated around a vertical axis to have the c axis 20° from the incident beam (near normal incidence or NI) or 70° away from it (grazing incidence or GI). The linear polarization of incident photons can be set either perpendicular (LV) or parallel (LH) to the scattering plane.

4.3.1 Cu L_3 edge

Figure 4.7 presents the Cu L_3 RIXS spectra measured on the optimally doped Bi2201 sample. Each spectrum is an accumulation of 2.5 hours measurements. The spectra bear a great similarity with CuO: the energy loss

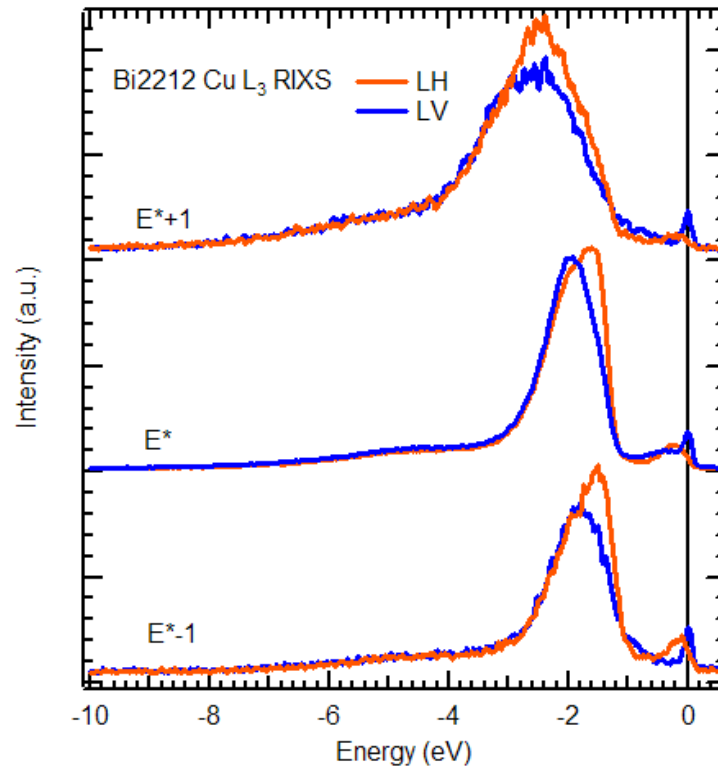


Figure 4.8: Bi2212 Cu L_3 RIXS spectra measured at three excitation energies, on resonance (middle, E^*), 1 eV below and above resonance.

around 2 eV is assigned to dd excitations and the broad low energy tail, extending down to 7 eV, is given by the charge transfer excitations. However dd excitations are clearly appearing at different energy scale compared with CuO. The reason is that the apical oxygen atoms are present in Bi2201 and induce different crystal field strength and ordering of $3d$ orbitals. On the other hand, the low energy excitation at ~ 250 meV is defined without ambiguity thanks to the visible elastic peak.

Figure 4.8 shows the RIXS spectra of Bi2212 measured at the L_3 absorption peak and ± 1 eV detuned from the resonance. It can be seen that the spectra below the resonance keep the same shape with respect to those on resonance. By contrast, 1 eV above the maximum of L_3 XAS peak, the spectra get considerably broader and the peak positions are clearly shifted away from the elastic peak. This shift signals the onset of non-Raman (flu-

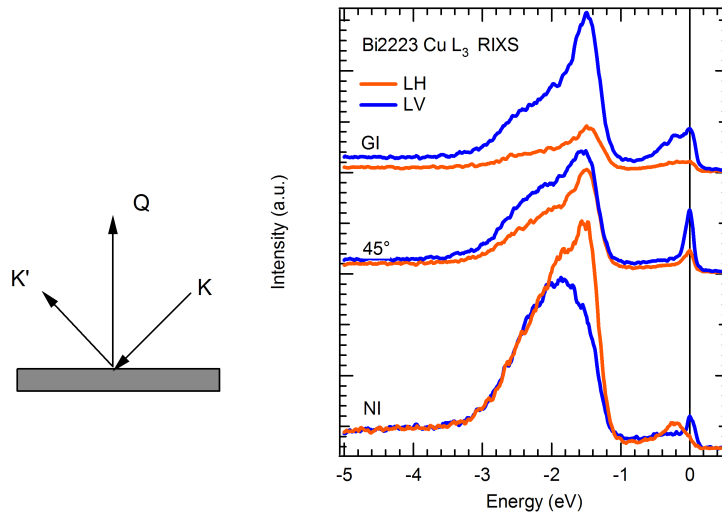


Figure 4.9: Left panel: the scattering geometry, i.e. momentum transfer diagram. Sample are rotated with scattering angle fixed. Right panel: Bi2223 Cu L_3 RIXS spectra measured at three different incidence angles: 20° grazing, 45° specular and 20° normal.

orescent) behavior. Also as expected the charge transfer region becomes more pronounced.

Figure 4.9 shows spectra of the Bi2223 sample for three different incidence angles, i.e. NI, 45° and GI. The acquisition time is the same for each spectrum so the intensity difference reflects the difference in their scattering cross sections. The dd excitation region shows a shape change with incidence angle. The peak at 1.5 eV is stronger closer to either grazing incidence for LV polarization or normal incidence for LH polarization. Therefore it is polarized in the Cu-O plane and assigned to xy orbital. The xz and yz orbitals cannot be resolved clearly but it should be on the high energy loss side of xy , which means the features around 2 eV. These observations, in terms of polarization and angle dependence, agrees very well with theoretical calculations done by van Veenendaal based on scattering operators approach [66].

Very interesting information is gained from the low energy excitation at ~ 250 meV. It has the same energy scale as what we have observed in

CuO, see §4.2. However the peak position and intensity shows a big angle dependence. The peak is pronounced and stays in the same position for NI and GI geometry. Near specular geometry, the peak position is very close the elastic peak therefore merges into the elastic peak as a small tail. It is tempting to interpret this angular dependence effect in terms of two magnon excitations, following the recent experimental and theoretical works in Cu K, L edge RIXS [67, 68, 69]. It must however be stressed that the theory developed for insulators Cannot be directly applied to the harder case of the doped metallic compounds.

From Figure 4.9, at 45° specular scattering, the effective Q transferred to the cuprate plane is essentially zero and the spectral weight nearly vanishes. Whereas at NI and GI geometry, there is a finite momentum transferred and the feature becomes visible. Notice that at L_3 edge, the excitation energy 930 eV smaller than at the K edge 8992.5 eV, but the Brilluoin zone of the cuprates could almost completely be sampled with the angular range available at SAXES, i.e. between 30° and 130° scattering angle ($Q_{max} \sim 0.9 \text{ \AA}^{-1}$). Further measurements over an extended angular range are in progress at the time of writing.

We have also performed measurements in the superconducting state, but we failed to identify any change in the spectra. For instance, Figure 4.10 shows the Bi2223 RIXS spectra measured at room temperature and 46 K. The spectra resemble each other for given polarization.

To summarize in Figure 4.11, the Cu L_3 RIXS spectra of these three samples are quite similar in terms of dd excitation structure and the low energy excitation. The somewhat larger width of the dd manifold in Bi2223 reflects the presence of inequivalent sites in the three-layer compound.

4.3.2 O K edge

The O $2p$ electrons are much less correlated than the Cu $3d$ electrons, and have essentially itinerant character forming a wide valence band. Nevertheless, in core level spectra they also exhibit typical features of strong correlation, due to bonding to the central Cu atom and thus hybridization

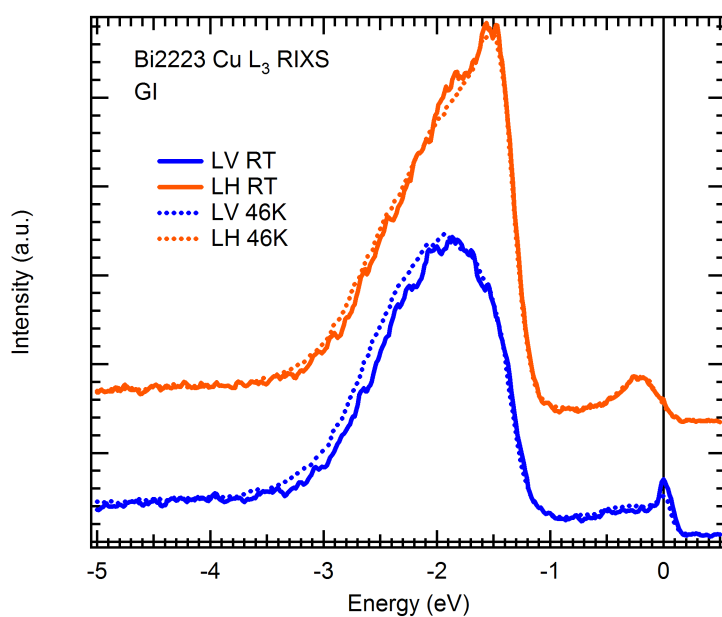


Figure 4.10: Cu L_3 RIXS spectra of Bi2223 at temperatures below and above T_c with LH and LV polarized light.

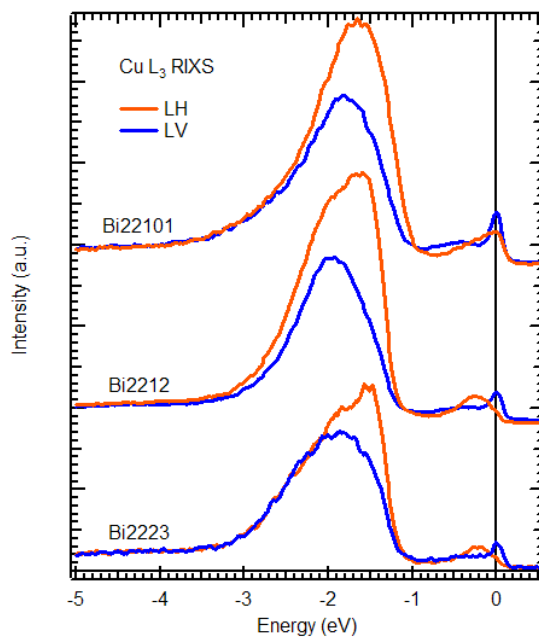


Figure 4.11: Cu L_3 RIXS spectra of Bi22101, Bi2212, Bi2223 at normal incidence.

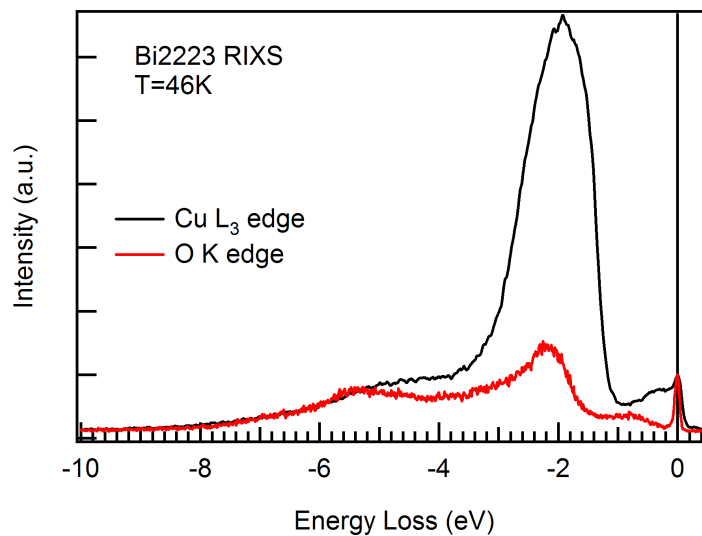


Figure 4.12: Comparison of RIXS spectra of Bi2223 at Cu L_3 and O K edges.

with $3d$ electrons. The possibility of using O K edge RIXS to investigate the many body electronic states was demonstrated by Okada and Kotani [54]. They showed that due to the strong Cu-O hybridization, the O K edge RIXS can detect the Cu dd excitations and the Zhang-Rice singlet (ZRS) state [70].

Figure 4.12 shows the RIXS spectra measured at the Cu L_3 and O K edges, with linear vertical polarized light at grazing incidence. Simply judging from this comparison, the 2 eV feature would be assigned to dd excitations and the 4-6 eV feature fits in the charge transfer region. But this is brought into doubt as we vary the excitation energy across O $1s$ absorption edge, as seen in Figure 4.13. Three excitation energies are chosen across the O $1s$ absorption edge: point B is on the resonance, and A and C are 0.6 eV detuned below and above the resonance respectively. The features from 1 to 6 eV have constant emission energy, which drifts away as shown in energy loss scale. This is remarkably different from measurements done in the insulating phase [71, 72], where it is possible to identify the dd excitations. This should not be related to the superconducting phase because we observe similar behavior in the normal state Bi2201 sample.

We investigate the low energy excitation at 0.8 eV in the following.

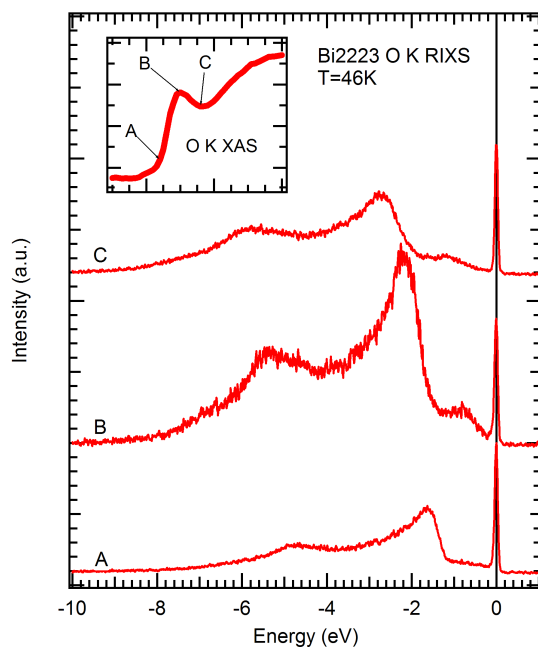


Figure 4.13: RIXS spectra of Bi2223 at O K edge below T_c . Inset: O K XAS spectrum labeled with selected excitation energies.

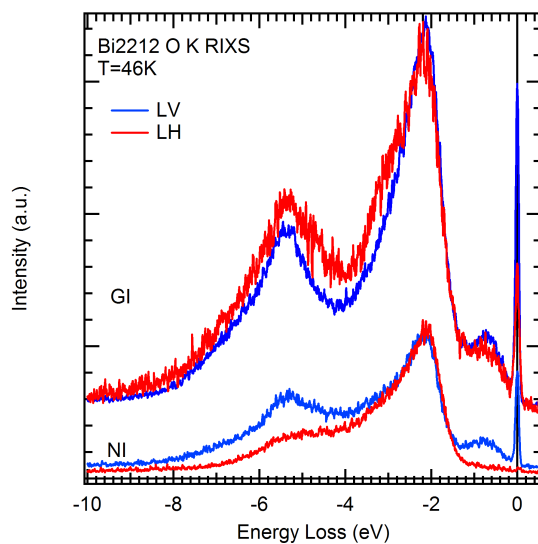


Figure 4.14: O K edge RIXS spectra of Bi2212 at normal and grazing incidence geometries with LH and LV polarized light.

Figure 4.14 shows the RIXS spectra excited at the O $1s$ absorption edge. It is clear that, under normal incidence configuration, both the elastic peak and 0.8 eV feature show a strong polarization dependence. In fact, for linear horizontal polarization, the 0.8 eV feature is completely off. This is consistent with $\text{Sr}_2\text{CuO}_2\text{Cl}_2$ measurements performed by Harada *et al* [71] where it was assigned to the two magnon excitation. By comparison with the Cu L_3 edge spectrum, this feature is essentially broadened and shifted towards high energy loss. This discrepancy probably comes from the itinerate nature of the $2p$ electrons in the metallic phase.

Chapter 5

RIPES study of CeX_9Si_4 ($X=\text{Ni},\text{Co}$)

We have used core level and valence band x-ray photoelectron spectroscopy, and resonant inverse photoemission at the Ce M_5 edge ($3d_{5/2} \rightarrow 4f$), to study the Ce $4f$ states in the isostructural metallic compounds CeCo_9Si_4 and CeNi_9Si_4 .

The spectroscopic data reveal the intermediate-valence nature of these materials. A comparison with other typical Ce-based IV materials shows that CeNi_9Si_4 is a moderately hybridized Kondo system. The $4f$ -band hybridization is larger in CeCo_9Si_4 as a result of a larger d density of states at the Fermi level, and of the reduced $4f$ binding energy. From Anderson impurity model relations we estimate a corresponding increase of the characteristic Kondo temperature T_K by a factor $\sim 4-5$ which explains, at least qualitatively, the remarkable differences of the $4f$ -related properties in the two compounds.

This provides a qualitative explanation for the remarkable differences in the magnetic, transport, and thermodynamic properties of the two materials.

Probing the nature of the Ce $4f$ states in CeX_9Si_4 ($X=\text{Ni}, \text{Co}$) by high-energy electron spectroscopies

X. Wang,¹ H. Michor,² and M. Grioni¹¹*IPN, Ecole Polytechnique Fédérale (EPFL), CH-1015 Lausanne, Switzerland*²*Institut für Festkörperphysik, TU Wien, Wiedner Hauptstrasse 8-10, A-1040 Wien, Austria*

(Received 18 October 2006; published 29 January 2007)

We have used x-ray photoelectron spectroscopy, and resonant inverse photoemission at the $\text{Ce}M_5(3d_{5/2} \rightarrow 4f)$ edge, to study the Ce $4f$ states in the isostructural metallic compounds CeCo_9Si_4 and CeNi_9Si_4 . The spectroscopic data reveal the intermediate-valence nature of these materials. They also suggest that a larger density of states at the Fermi level, and a reduced $4f$ energy, are the origin of an enhanced $4f$ -conduction band hybridization in the Co compound. This provides an explanation for the remarkable differences in the magnetic, transport, and thermodynamic properties of the two materials.

DOI: [10.1103/PhysRevB.75.035127](https://doi.org/10.1103/PhysRevB.75.035127)

PACS number(s): 71.28.+d, 78.70.En, 78.70.Dm, 79.60.-i

I. INTRODUCTION

Metallic Ce compounds are of great interest for the intriguing physical properties associated with the $4f$ electrons. Due to the competition of Coulomb interaction and hybridization with the conduction band, these states are intermediate between local spin and extended band states.¹ The $4f$ occupation number n_f is neither integer nor constant, and the local magnetic moments observed at high temperature are screened and compensated at sufficiently low temperature. The strongly correlated, partially localized $4f$ states yield anomalous contributions to most physical properties, including the magnetic susceptibility, the electronic specific heat, and the thermal and electrical resistivities. The main features of this intermediate-valence (IV) or “Kondo” behavior are often well described in terms of isolated Ce impurities in a metallic matrix. In the simple Anderson impurity model (AIM), but also in more general Anderson lattice models (ALMs), the anomalous quantities exhibit an approximate scaling as a function of the single parameter (T/T_K). The material-dependent Kondo temperature T_K represents the energy gained in the formation of the nonmagnetic ground state, and grows exponentially with the $4f$ -band hybridization strength.^{2,3}

In this paper we analyze the Ce valence and hybridization strength of two isostructural cerium Kondo-lattice compounds CeNi_9Si_4 and CeCo_9Si_4 with almost equal unit cell volumes ($\Delta V/V=5.56 \times 10^{-3}$) but remarkably different degrees of hybridization. CeNi_9Si_4 is an archetypal Kondo-lattice system. It exhibits thermodynamic properties that are very well described by the integer-valent limit of the AIM, the Coqblin-Schrieffer model, for a fully degenerate Ce^{3+} ($J=5/2$) ion, with a characteristic temperature $T_0 \approx 180$ K. The Wilson ratio $R \approx 1.25$ is also in close agreement with the theoretical value for a six-fold degenerate Ce^{3+} state.⁴ Remarkable agreement with ALM results by Cox and Grewe⁵ was also observed for transport properties. In particular, the analysis of the thermoelectric power yields a Kondo temperature $T_K \sim 80$ K in agreement with the above T_0 , according to the theoretical ratio $T_K/T_0 \approx 0.43$ for $J=5/2$ by Schlottmann.⁶

Replacing Ni by Co in the isostructural compound CeCo_9Si_4 leads to remarkably different physics originating

from the different features of the Ni and Co $3d$ bands, and to more strongly hybridized $4f$ states.⁷ The isostructural reference systems LaNi_9Si_4 and LaCo_9Si_4 reveal for the Ni $3d$ bands simple Pauli paramagnetic behavior with moderate Stoner-enhancement $S \leq 2$ but strongly correlated nearly magnetic Co $3d$ bands with large Stoner enhancement $S \sim 20$ and itinerant electron metamagnetism at rather low fields of about 3–6 T.^{4,8} While it proved to be straightforward to extract the $4f$ Kondo contribution to the specific heat and magnetic susceptibility of CeNi_9Si_4 by subtracting the LaNi_9Si_4 reference data as background, it would clearly be misleading to use LaCo_9Si_4 as a background reference for CeCo_9Si_4 . Both the low-temperature electronic specific heat coefficient $\gamma \approx 190$ mJ/mol K² and the magnetic susceptibility $\chi_0 \approx 30 \times 10^{-3}$ emu/mol (Refs. 7 and 9) are in fact smaller than $\gamma \approx 200$ mJ/mol K² and $\chi_0 \approx 51 \times 10^{-3}$ emu/mol of LaCo_9Si_4 (see Refs. 4, 7, and 8). Simply using γ and χ_0 to estimate T_K and the degree of hybridization of the $4f$ states in CeCo_9Si_4 is questionable, and yields values that are inconsistent with structural data. The latter suggest a rather strong hybridization, since the reduction of the unit cell volume of CeCo_9Si_4 as compared to LaCo_9Si_4 , $\Delta V/V = -12.0 \times 10^{-3}$, is significantly larger than is the case of CeNi_9Si_4 and LaNi_9Si_4 , $\Delta V/V = -9.1 \times 10^{-3}$. It is also much larger than $\Delta V/V \sim -7 \times 10^{-3}$, the value expected from the trend due to the lanthanide contraction in $\text{R}^{3+}\text{Co}_9\text{Si}_4$, with $\text{R}^{3+} = \text{La}, \text{Pr}, \text{Nd}, \dots$, for hypothetical $\text{Ce}^{3+}\text{Co}_9\text{Si}_4$.

High-energy electron spectroscopies, namely photoemission (PES) and inverse photoemission (IPES), provide a view of the Ce electronic configuration that is complementary to low-energy magnetic, transport, or thermodynamic probes.^{10,11} The PES and IPES spectra directly probe the $4f$ spectral function, namely, the characteristic many-body Kondo resonance (KR). They also yield quantitative information on configuration mixing in the IV ground state, and on the density of states (DOS) at the Fermi level, which plays a key role in determining the $4f$ -band hybridization strength. Comparing the PES and IPES spectral response of CeCo_9Si_4 and CeNi_9Si_4 can therefore reveal and clarify differences in the nature of the $4f$ states in the two compounds. Here we report core level and valence band PES as well as resonant IPES (RIPES) measurements. Both compounds ex-

hibit the spectroscopic signatures of IV materials. A comparison of the valence band PES spectra reveals a higher density of conduction states at the Fermi level and a lower $4f$ binding energy in CeCo_9Si_4 . Within a Kondo scenario, these differences are the likely origin of the stronger $4f$ -band hybridization in CeCo_9Si_4 , and ultimately of the differences in the electronic properties of the two materials.

II. EXPERIMENT

Polycrystalline CeCo_9Si_4 was prepared by high-frequency induction melting under protective Ar (99.9999%) atmosphere. The starting materials are cerium ingots (99.98% purity, Ames Materials Preparation Center, USA), cobalt ingots (99.995%, Alpha Aesar, Ward Hill, MA, USA), and silicon pieces (99.9999%, Alpha Aesar) melted together in a two-step procedure. Initially, Co and Si were melted together and remelted four times. In a second step Ce was melted together with the precursor Co_9Si_4 alloy. To ensure homogeneity and phase purity, the buttons were broken, flipped over, and remelted another five times and finally sealed in an evacuated quartz tube and annealed at 1050 °C for 10 days. The polycrystalline CeNi_9Si_4 material used in the present investigation is identical with that characterized earlier in Ref. 4.

We performed PES and RIPES measurements at Lausanne. The specimens were mounted on a flow cryostat, and clean surfaces were prepared in vacuum by repeatedly scraping with a diamond file, at a base pressure in the low 10^{-10} mbar range. For the PES measurements we used a Scienta ESCA300 spectrometer, equipped with a monochromatized Al $K\alpha$ ($h\nu=1486$ eV) source, and a hemispherical electrostatic analyzer. The overall energy resolution was $\Delta E=0.4$ eV. The RIPES spectrometer is based on a slitless crystal spectrograph in a dispersive Bragg geometry, described in Ref. 12. For measurements at the $\text{Ce}M_5$ edge (~ 881 eV) we used a beryl (1010) crystal, with an overall resolution of ~ 1 eV.

III. RESULTS AND DISCUSSION

Figure 1 illustrates the Ce $3d$ core level PES spectra of CeNi_9Si_4 , CeCo_9Si_4 , and of selected reference Ce materials, from the literature.^{13,14} The Ce $3d$ PES line shape of IV Ce systems is complex. First of all, the spectrum is split by the large (~ 20 eV) $3d$ spin-orbit interaction into two partially overlapping $j=5/2$ and $j=3/2$ manifolds. Each spin-orbit partner is further split into three features corresponding to PES final states with (mainly) 0, one, or two $4f$ electrons. The order of the $4f$ configurations in the final state (f^2 , f^1 , and f^0) is different from that of the neutral initial state (f^1 , f^0 , and f^2) as a result of the large attractive Coulomb interaction (~ 8 eV per $4f$ electron) with the $3d$ core hole. The relative intensities of the PES features are determined by their coupling with the mixed ground state. The f^0 peak, in particular, corresponds to an almost pure f^0 final state, and its intensity is an excellent indicator of the quantity $(1-n_f)$ in the ground state, and therefore of the Ce valence $v=3+(1-n_f)$.^{13,15} It is very small in materials like, e.g., Ce_7Ni_3 [Fig. 1(a)], where

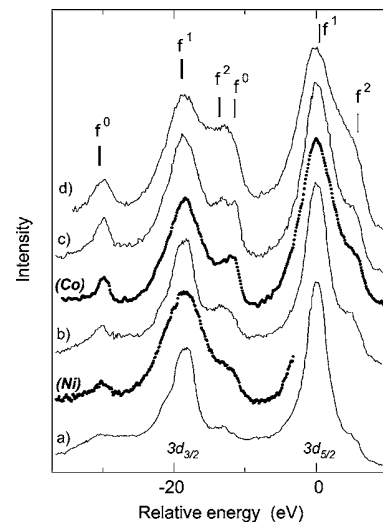


FIG. 1. PES spectra of the Ce $3d$ core levels of CeNi_9Si_4 , CeCo_9Si_4 , and of selected IV Ce compounds. (a) Ce_7Ni_3 , (Ni), CeNi_9Si_4 ; (b) CeNi; (Co), CeCo_9Si_4 ; (c) CeNi_2 ; (d) CeRh_3 . Vertical ticks mark the various final states (thick $3d_{3/2}$; thin $3d_{5/2}$).

the $4f$ -band hybridization is small, and large in strongly hybridized materials like CeRh_3 [Fig. 1(d)].

These qualitative considerations can be put on a quantitative basis within the framework of the AIM,¹⁶ and a very satisfactory agreement with experiment has been achieved by adopting configuration-dependent parameters.^{17,18} Determining the absolute n_f values from PES requires a rather elaborate analysis to separate contributions from the (less hybridized) surface Ce ions. Figure 1 illustrates a more qualitative approach, based on a comparison with reference compounds, spanning a wide range of hybridization strengths. The energy reference is set at the peak position of the $j=5/2$ (f^1) feature (the actual binding energy is $E_B=881$ eV), and the spectrum of CeNi_9Si_4 is truncated on the high-energy side, where it overlaps with a very strong Ni $2p$ core feature. The larger intensity of the (f^0) feature indicates an increasing configuration mixing from CeNi_9Si_4 to CeCo_9Si_4 . The spectrum of CeNi_9Si_4 is intermediate between those of Ce_7Ni_3 —an antiferromagnet, with $T_K \sim 2$ K,¹⁹ $n_f \sim 1$ —and of CeNi, with estimated $T_K \sim 100$ – 140 K and $n_f > 0.9$.^{20,21} The spectrum of CeCo_9Si_4 is similar to that of CeNi_2 , a compound that is near the limit of validity of the AIM, with estimated $T_K > 1000$ K (Ref. 22) and $n_f \sim 0.83$.¹⁰ The $3d$ core level results show that CeNi_9Si_4 to CeCo_9Si_4 are IV compounds, and indicate a strong enhancement of the $4f$ -band hybridization in the latter, consistent with a much higher T_K .

The origin of the larger hybridization in CeCo_9Si_4 is clarified by the PES valence band (VB) spectra, shown in Fig. 2 after the usual subtraction of an inelastic Shirley background. They reflect the momentum-integrated density of states, and are dominated by the Ni and Co $3d$ bands at and just below the Fermi level E_F . Additional structures in the 4–7 eV range can be assigned to Si sp hybrid states. A shoulder at ~ 2.3 eV in CeNi_9Si_4 is the signature of the Ce $4f$ states. It corresponds to the “ionization” (f^0) final state. This signal is weak due to the low Ce concentration, and also to the unfa-

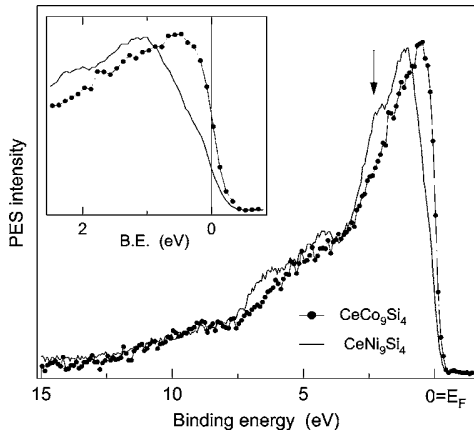


FIG. 2. Valence band PES spectra of CeNi_9Si_4 and CeCo_9Si_4 measured at 300 K ($h\nu=1486$ eV). The arrow marks the “ionization” (f^0) final state in CeNi_9Si_4 . The inset shows a closeup of the spectra near the Fermi level.

favorable cross section at this large photon energy.²³ The absence of a similar discernible feature in the Co compound is consistent with the expected transfer of spectral weight from the ionization peak to the KR feature above E_F as the hybridization increases. The main difference between the data is a ~ 0.5 eV rigid shift toward higher binding energy of the CeNi_9Si_4 line shape, reflecting the addition of one extra $3d$ electron in the Ni $3d$ band. In the inset of Fig. 2 the peak of the Co $3d$ band at $E \sim 0.5$ eV is barely distinguishable from the onset of the metallic Fermi edge. By contrast, the maximum of the Ni $3d$ band at 1 eV is well separated from the metallic Fermi step at E_F . The data show that the $3d$ DOS at E_F is larger in CeCo_9Si_4 than in CeNi_9Si_4 by a factor of 2. We notice that specific heat data and band structure calculations indicate a similar increase in the corresponding La compounds, from ~ 10 states/eV (LaNi_9Si_4) (Refs. 4 and 24) to 19 states/eV (LaCo_9Si_4).⁸

The twofold increase of the $3d$ DOS at E_F in CeCo_9Si_4 has a large impact on the electronic properties. Within the AIM, $T_K \approx D \exp(-\pi\varepsilon_f/MT)$, where D is the bandwidth, ε_f is the bare $4f$ binding energy, and N is the degeneracy of the $4f$ states.² The “hybridization width” $\Gamma = \pi\rho(E_F)V^2$ is proportional to the conduction band DOS at E_F , $\rho(E_F)$, and to the square of a $4f$ -band hopping matrix element. The parameters D , N , and V should have similar values in the two isostructural compounds. On the other hand, in a rigid band scenario, the bare energy of the $4f$ states is probably tied to the centroid of the conduction band, and ε_f is therefore reduced from ~ 2.3 eV in CeCo_9Si_4 , to ~ 1.8 eV in CeNi_9Si_4 . These simple considerations suggest that T_K should increase by a factor $\sim 4-5$ between CeNi_9Si_4 and CeCo_9Si_4 as a result of the combined changes in $\rho(E_F)$ and ε_f .

In Ce-based materials the valence band PES spectrum contains only the occupied tail of the many-body KR, whose maximum is located above E_F . This signal is too weak to be distinguished from the strong $3d$ band in Fig. 2. The KR can be probed by IPES, which is sensitive to the electron-addition, “unoccupied” part of the many-body spectral function $A(\omega)$.¹¹ Since the Ce concentration is low in our com-

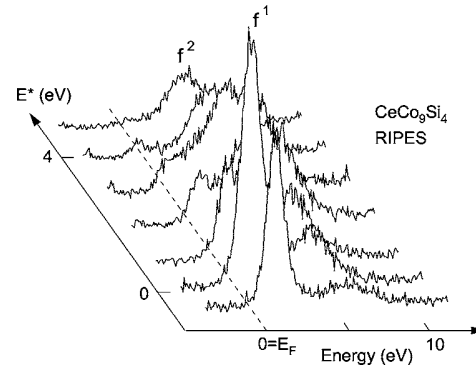


FIG. 3. RIPES of CeCo_9Si_4 near the $\text{Ce}3d_{5/2}$ (M_5) threshold. Spectra measured at increasing incident energy $E_{in}=E^*+881$ eV have been vertically offset for clarity.

pounds, the measured KR intensity is also weak, but the Ce $4f$ spectral function can be strongly enhanced by an appropriate choice of the excitation energy. In a resonant IPES experiment, the energy E_{in} of the exciting electron beam is chosen to coincide with the binding energy of a Ce $3d$ or $4d$ core level.²⁵⁻²⁷ As for the more common resonant PES, the resonant enhancement in RIPES is due to the interference of two transition channels sharing the same initial and final states. In RIPES the normal IPES channel $4f^N+e \rightarrow 4f^{N+1}+h\nu$ interferes with the indirect channel $4f^N+e \rightarrow 3d^9 4f^{N+2} \rightarrow 4f^{N+1}+h\nu$. Due to the localized nature of the $3d$ core hole, and to dipole selection rules, RIPES mainly reflects the $4f$ part of the addition spectrum, projected on the Ce site. RIPES is a second-order coherent process, and specific aspects of the spectral weight distribution depend not only on the ground state, but also on the intermediate state, which contains a core hole. Detailed calculations can be performed in the framework of the AIM,²⁸ but a direct comparison of the spectra already gives important indications on the nature of the $4f$ electrons.

Figure 3 shows typical RIPES results for CeCo_9Si_4 . Each curve represents the energy distribution of the emitted photons, for a fixed incident electron energy E_{in} . The horizontal axis measures, as in conventional IPES, the final state excitation energy $E=[h\nu_{out}(\text{max})-h\nu_{out}]$, and the high emitted photon energy limit $h\nu_{out}(\text{max})$ coincides with E_F . Different spectra correspond to different incident energies ($E_{in}=881$ eV + E^*) around the $\text{Ce}3d_{5/2}$ (M_5) threshold, and the curves have been vertically offset for clarity. The (f^1) final state feature (the KR) exhibits a sharp maximum at $E^*=0$, while the intensity of the broader (f^2) multiplet has a delayed maximum at $E^* \sim 2-3$ eV, in agreement with RIPES data on other Ce IV materials.²⁶

The large spectral changes that occur as a function of the incident energy in the resonance region are clearly illustrated in Fig. 4(a), which compares the $E^*=0$ and $E^*=3$ eV spectra of CeNi_9Si_4 . At $E^*=0$ the KR near E_F dominates the IPES line shape, but its intensity decreases by roughly one order of magnitude at $E^*=3$, where the broad (f^2) multiplet is in its turn enhanced. Relative changes in the KR intensity as a function of external parameters like temperature or stoichiometry are therefore best studied at $E^*=0$. Figure 4(b) shows

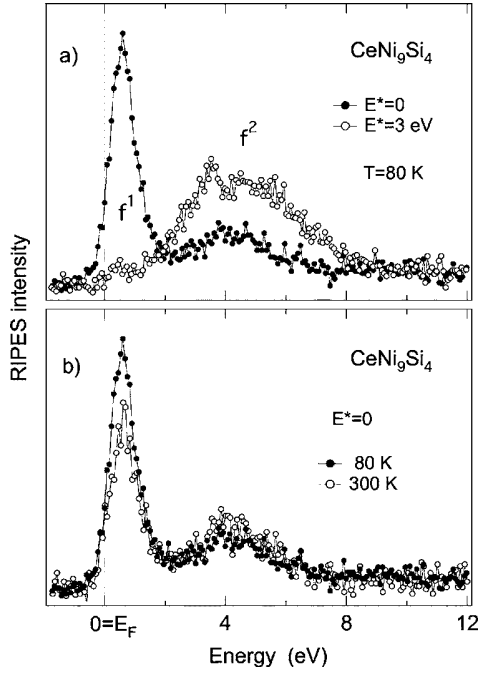


FIG. 4. (a): RIPES spectra of CeNi_9Si_4 measured at 80 K at the maxima of the f^1 ($E^*=0$) and f^2 ($E^*=3$ eV) resonances. (b) Comparison of the $E^*=0$ spectra at 80 and 300 K.

the temperature evolution between 80 and 300 K under these conditions. The intensity of the KR decreases at the higher temperature, as low-lying magnetic (f^1) excited states become thermally populated.^{2,11} It should be noticed that the intensity lost by the KR is only partly compensated by an increase of the f^2 intensity: the total spectral weight is not conserved at resonance, since the intensity enhancement is different for different final states. Therefore the simple f^1/f^2 intensity ratio does not entirely determine the initial state Ce configuration.

The Ce valence state can still be estimated from a comparison of the separate f^1 and f^2 resonance intensity profiles, as discussed in Ref. 26. The constant final state (CFS) curves of Fig. 5 represent the integrated f^1 and f^2 IPES intensities, measured within two separate energy windows, while varying the incident energy across the Ce M_5 threshold. They illustrate the sharp enhancement of the f^1 emission at E^* , and the broader f^2 maximum around $E^*=2-3$ eV. For each compound, CFS curves collected at 300 and 80 K are shown, arbitrarily normalized to the same f^2 peak intensity. The ratio R of the maxima of the f^1 and f^2 CFS profiles in different Ce-based IV materials grows with the weight of the f^0 configuration in the initial state. From Fig. 5 we find $R \sim 1$ for CeCo_9Si_4 at 80 K, which is somewhat smaller than the corresponding values for strongly hybridized systems like CeFe_2 ($R=1.2$) and CeNi_2 ($R=1.37$).²⁶ The smaller $R \sim 0.56$ for CeNi_9Si_4 at 80 K is typical for moderately hybridized Kondo systems like, e.g., CePd_3 ($T_K \sim 240$ K).²⁶ This is consistent with the conclusions drawn from the PES data of Fig. 1. The results of Fig. 5 also show that R decreases from 80 to 300 K, as already suggested by the data of Fig. 4, in agreement with the characteristic Kondo tempera-

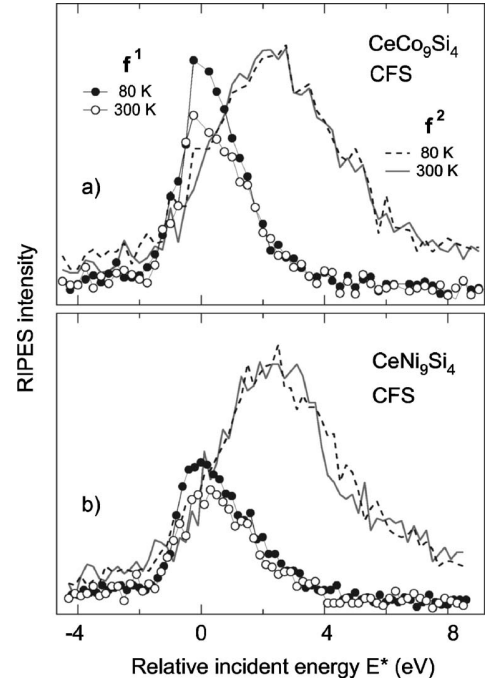


FIG. 5. Constant final state (CFS) curves of (a) CeCo_9Si_4 and (b) CeNi_9Si_4 showing the separate f^1 and f^2 resonance profiles. CFS curves measured at 80 and 300 K have been arbitrarily normalized to the maximum of the f^2 resonance.

ture dependence of n_f . It is interesting that the temperature change is visible for both compounds despite the considerably different T_K values. According to the AIM the temperature-driven change Δn_f occurs almost entirely between $T \sim (T_K/3)$ and $T \sim 3T_K$.² For CeNi_9Si_4 ($T_K \sim 80$ K) the measurement covers a substantial part of the temperature range of interest, from T_K to $\sim 4T_K$. On the other hand, the observation of a clear temperature dependence sets a rough upper limit $T_K < (2-3) \times 300$ K for CeCo_9Si_4 . This, again, is compatible with the T_K enhancement between CeNi_9Si_4 and CeCo_9Si_4 expected from the VB PES data of Fig. 2.

IV. SUMMARY

We have studied by core level and valence band x-ray photoelectron spectroscopy, and by resonant inverse photoemission, the electronic configuration of the two isostructural Ce compounds CeNi_9Si_4 and CeCo_9Si_4 . A comparison with other typical Ce-based IV materials shows that CeNi_9Si_4 is a moderately hybridized Kondo system. The $4f$ -band hybridization is larger in CeCo_9Si_4 as a result of a larger d density of states at the Fermi level, and of the reduced $4f$ binding energy. For $\rho(E_F)$ we observe the same twofold increase previously determined for the corresponding La compounds. From AIM relations we estimate a corresponding increase of the characteristic Kondo temperature T_K by a factor $\sim 4-5$ which explains, at least qualitatively, the remarkable differences of the $4f$ -related properties in the two compounds. This value should be considered as a lower limit for the ratio of the two T_K 's. In fact, the $4f$ -band hybridization is often

reduced in the near-surface region probed by electron spectroscopies, and the effect is proportionally larger in large T_K materials.^{29,30} A complementary investigation by photon-in-photon-out spectroscopies like high-resolution x-ray absorption or resonant inelastic x-ray scattering,^{31,32} which are less sensitive to the surface layer, could yield a more accurate quantitative estimation of the bulk T_K 's. Nevertheless, we anticipate that such quantitative refinement will not influence the main qualitative results of the present study, which confirms the interest of combining traditional “low-energy” and

“high energy” spectroscopic data for a deeper understanding of IV materials.

ACKNOWLEDGMENTS

We gratefully acknowledge very useful correspondence with D. Malterre and N. Witkowski. The work in Lausanne is supported by the Swiss National Science Foundation and by the NCCR MaNEP.

-
- ¹P. A. Lee, T. M. Rice, J. W. Serene, L. S. Sham, and J. W. Wilkins, *Comments Condens. Matter Phys.* **12**, 99 (1986).
²N. E. Bickers, D. L. Cox, and J. W. Wilkins, *Phys. Rev. B* **36**, 2036 (1987).
³A. C. Hewson, *The Kondo Problem to Heavy Fermions* (Cambridge University Press, Cambridge, U.K., 1993).
⁴H. Michor, St. Berger, M. El-Hagary, C. Paul, E. Bauer, G. Hilscher, P. Rogl, and G. Giester, *Phys. Rev. B* **67**, 224428 (2003).
⁵D. L. Cox and N. Grewe, *Z. Phys. B: Condens. Matter* **71**, 321 (1988).
⁶P. Schlottmann, *Z. Phys. B: Condens. Matter* **51**, 223 (1983).
⁷M. El-Hagary, H. Michor, E. Bauer, R. Grössinger, P. Kersch, D. Eckert, K.-H. Müller, P. Rogl, G. Giester, and G. Hilscher, *Physica B* **359-361**, 311 (2005).
⁸H. Michor, M. El-Hagary, M. D. Mea, M. W. Pieper, M. Reissner, G. Hilscher, S. Khmelevskiy, P. Mohn, G. Schneider, G. Giester, and P. Rogl, *Phys. Rev. B* **69**, 081404(R) (2004).
⁹More recent results yield $\chi_0 \sim 17 \times 10^{-3}$ emu/mol. The discrepancy is due to a ferromagnetic impurity phase in the sample used in Ref. 7; H. Michor and M. Giovannini (unpublished).
¹⁰J. W. Allen, S.-J. Oh, O. Gunnarsson, K. Schönhammer, M. B. Maple, M. S. Torikachvili, and I. Lindau, *Adv. Phys.* **35**, 275 (1986).
¹¹D. Malterre, M. Grioni, and Y. Baer, *Adv. Phys.* **45**, 299 (1986).
¹²P. Weibel, M. Grioni, C. Heche, and Y. Baer, *Rev. Sci. Instrum.* **66**, 3755 (1995).
¹³J. C. Fuggle, F. U. Hillebrecht, Z. Zolnierok, R. Lässer, Ch. Freiburg, O. Gunnarsson, and K. Schönhammer, *Phys. Rev. B* **27**, 7330 (1983).
¹⁴L. Duó, P. Vavassori, L. Braicovich, N. Witkowski, D. Malterre, M. Grioni, Y. Baer, and G. Olcese, *Z. Phys. B: Condens. Matter* **103**, 63 (1997).
¹⁵J. Krill, J.-P. Kappler, A. Meyer, L. Abadli, and M. F. Ravet, *J. Phys. F: Met. Phys.* **11**, 1713 (1981).
¹⁶O. Gunnarsson and K. Schönhammer, *Phys. Rev. B* **28**, 4315 (1983).
¹⁷O. Gunnarsson and O. Jepsen, *Phys. Rev. B* **38**, 3568 (1988).
¹⁸N. Witkowski, F. Bertran, and D. Malterre, *Phys. Rev. B* **56**, 15040 (1997).
¹⁹K. Umeo, H. Kadomatsu, and T. Takabatake, *Phys. Rev. B* **54**, 1194 (1996).
²⁰D. Gignoux, F. Givord, and R. Lemaire, *J. Less-Common Met.* **94**, 165 (1983).
²¹J. I. Espeso, J. C. Gomez Sal, and J. Chaboy, *Phys. Rev. B* **63**, 014416 (2000).
²²A. P. Murani and R. S. Eccleston, *Phys. Rev. B* **53**, 48 (1997).
²³J. J. Yeh and I. Lindau, *At. Data Nucl. Data Tables* **32**, 1 (1985).
²⁴S. Khmelevskiy (private communication).
²⁵P. Weibel, M. Grioni, D. Malterre, B. Dardel, and Y. Baer, *Phys. Rev. Lett.* **72**, 1252 (1994).
²⁶M. Grioni, P. Weibel, D. Malterre, Y. Baer, and L. Duó, *Phys. Rev. B* **55**, 2056 (1997).
²⁷K. Kanai, T. Terashima, A. Kotani, T. Uozumi, G. Schmerber, J. P. Kappler, J. C. Parlebas, and S. Shin, *Phys. Rev. B* **63**, 033106 (2001).
²⁸A. Tanaka and T. Jo, *J. Phys. Soc. Jpn.* **65**, 615 (1996).
²⁹E. Weschke, C. Laubschat, T. Simmons, M. Domke, O. Strel, and G. Kaindl, *Phys. Rev. B* **44**, 8304 (1991).
³⁰A. Sekiyama, T. Iwasaki, K. Matsuda, Y. Saitoh, Y. Onuki, and S. Suga, *Nature (London)* **403**, 396 (2000).
³¹C. Dallera, M. Grioni, A. Shukla, G. Vanko, J. L. Sarrao, J. P. Rueff, and D. L. Cox, *Phys. Rev. Lett.* **88**, 196403 (2002).
³²A. Kotani, *Eur. Phys. J. B* **47**, 3 (2005).

Chapter 6

Conclusion

This thesis presents spectroscopic investigations of the electronic properties of materials that belong to two important classes of strongly correlated systems: transition metal oxides including the high T_c superconducting cuprates, and intermediate valence Kondo systems. In this work I have utilized two advanced spectroscopic techniques: resonant inelastic soft x-ray scattering (RIXS) and resonant inverse photoemission spectroscopy (RIPES).

The high resolution RIXS experiments were carried out with the SAXES spectrometer at the ADDRESS beamline of the Swiss Light Source (SLS). The construction, commissioning and fine-tuning of these two very sophisticated instruments constitute the main part of this thesis. The design goal of reaching a world-record resolution better than 100 meV below 1000 eV has been successfully achieved. This very high resolving power was exploited in various experiments, revealing unprecedented details of the electronic structure of selected materials.

NiO, a paradigmatic strongly correlated antiferromagnetic material, was chosen as a benchmark test of the high resolution apparatus. The data confirm and considerably extend previous results from the literature. In particular, it shows well defined dd excitation peaks, in agreement with the data collected at much lower excitation energies, at the Ni $M_{2,3}$ edge. More interestingly, the present results yield entirely new low energy losses

below 200 meV, which we assign to magnetic excitations. These features can be qualitatively reproduced described by introducing the exchange field into a simple atomic model, but our observations raise new interesting questions. In the q -dependent measurements, these energy losses do not display momentum dependence, in stark contrast to what we found later on in the two-dimensional high T_c cuprates. This observation requires more realistic modeling to account for the momentum dependence of magnetic excitations. Data measured at the O K edge provide a complementary view of the spin excitations. Further dedicated measurements would certainly help to clarify the local (spin-flip) or collective (magnon or bi-magnon) nature of these excitations.

The high T_c superconducting cuprates are a subject of enduring interest, and their electronic structure is an outstanding problem in solid state physics. Our RIXS experiments on three different members of the BSCCO family have revealed a ~ 200 meV excitation which disperses with transferred momentum. This reveals a similarity with magnetic excitations probed in other cuprates by inelastic neutron scattering, and especially with signatures of bi-magnon losses recently observed in the hard x-ray domain by Cu K edge RIXS. Here again the O K edge data provide complementary information on these excitations, as seen from the ligand site. Interestingly, the signatures of the magnetic losses are less intense than at the Cu edge, while the spectral function is dominated by charge transfer features. A thorough comparison of these complementary information can reveal important aspects of the local and collective electron dynamics in the CuO_2 planes.

The power of resonant spectroscopy was also confirmed in our RIPES experiments. In the isostructural metallic compounds CeCo_9Si_4 and CeNi_9Si_4 , the spectroscopic data reveal the intermediate-valence nature of these materials, determined by the characteristic Kondo temperature T_K . This provides a qualitative explanation for the remarkable differences in the magnetic, transport, and thermodynamic properties of the two materials.

In summary, the low energy excitations, in terms of charge and spin fluctuations, have been detected and investigated. Thanks to the very

high resolution of our instrument, the new results reveal unambiguous details about the magnetic excitations in NiO and in selected cuprates. Part of this information was previously attainable by well-established spectroscopic techniques like neutron and raman scattering. RIXS offers new very attractive features like the chemical selectivity and the possibility of measuring samples of very small volume. High resolution RIXS is becoming a new probe of strong electronic correlations, and this thesis is just the start.

Bibliography

- [1] N. Mott and H. Jones, *The Theory of the Properties of Metals and Alloys* (Oxford University Press, Oxford, 1936).
- [2] N. W. Ashcroft and D. N. Mermin, *Solid State Physics* (Thomson Learning, Toronto, 1976).
- [3] *Solid State Physics*, edited by D. Turnbull and H. Ehrenreich (Academic, New York, 1976), Vol. 24.
- [4] D. Pines and P. Nozières, *The Theory of Quantum Liquids* (W.A. Benjamin, New York, 1966).
- [5] G. Mahan, *Many-Particle Physics*, 3rd ed. (Plenum, New York, 1986).
- [6] P. Hohenberg and W. Kohn, *Phys. Rev.* **136**, B864 (1964).
- [7] N. F. Mott, *Metal-Insulator Transitions* (Taylor and Francis, London, 1974).
- [8] P. Cox, *Transition Metal Oxides* (Clarendon, Oxford, 1992).
- [9] M. Imada, A. Fujimori, and Y. Tokura, *Reviews of Modern Physics* **70**, 1039 (1998).
- [10] P. Fulde, *Electron Correlations in Molecules and Solids* (SpringerVerlag, Berlin, 1991).
- [11] J. Zaanen, G. A. Sawatzky, and J. W. Allen, *Physical Review Letter* **55**, 418 (1985).

Bibliography

- [12] For a recent review: Strongly Correlated Systems, special issue of the J. Electr. Spectr. 117-118, M. Grioni Editor (2001).
- [13] E. Wuilloud, H. R. Moser, W. D. Schneider, and Y. Baer, Phys. Rev. B **28**, 7354 (1983).
- [14] C. Gu, X. Wu, C. G. Olson, and D. W. Lynch, Phys. Rev. Lett. **67**, 1622 (1991).
- [15] D. Wieliczka, J. H. Weaver, D. W. Lynch, and C. G. Olson, Phys. Rev. B **26**, 7056 (1982).
- [16] D. Malterre, M. Grioni, and Y. Baer, Advances in Physics **45**, 299 (1996).
- [17] Y. Tezuka and S. Shin, Journal of Electron Spectroscopy and Related Phenomena **136**, 151 (2004).
- [18] R. J. Liefeld, A. F. Burr, and M. B. Chamberlain, Phys. Rev. A **9**, 316 (1974).
- [19] M. B. Chamberlain, A. F. Burr, and R. J. Liefeld, Phys. Rev. A **9**, 663 (1974).
- [20] F. Riehle, Ph.D. thesis, Karlsruhe Universität, 1977.
- [21] P. Weibel, M. Grioni, C. Heche, and Y. Baer, Review Of Scientific Instruments **66**, 3755 (1995).
- [22] M. Grioni, P. Weibel, D. Malterre, Y. Baer, and L. Duo, Physical Review B **55**, 2056 (1997).
- [23] K. Kanai, T. Terashima, A. Kotani, T. Uozumi, G. Schmerber, J. P. Kappler, J. C. Parlebas, and S. Shin, Physical Review B **63**, 033106 (2001).
- [24] S. Shin, A. Agui, M. Fujisawa, Y. Tezuka, T. Ishii, and H. N., Review Of Scientific Instruments **66**, 1584 (1995).

- [25] Visual programming platform from National Instruments: <http://www.ni.com/labview>.
- [26] P. W. Anderson, *Phys. Rev.* **124**, 41 (1961).
- [27] A. Kotani and Y. Toyozawa, *Journal of the Physical Society of Japan* **37**, 912 (1974).
- [28] O. Gunnarsson and K. Schönhammer, *Physical Review B* **28**, 4315 (1983).
- [29] J. Zaanen, G. A. Sawatzky, J. Fink, W. Speier, and J. C. Fuggle, *Physical Review B* **32**, 4905 (1985).
- [30] G. Ghiringhelli, A. Piazzalunga, C. Dallera, G. Trezzi, L. Braicovich, T. Schmitt, V. N. Strocov, R. Betemps, L. Patthey, X. Wang, and M. Grioni, *Review Of Scientific Instruments* **77**, 113108 (2006).
- [31] Graphical interface for SHADOW, <http://www.esrf.eu/computing/scientific/xop2.1/>.
- [32] J. Schweppe, R. Deslattes, T. Mooney, and P. C.J., *Journal of Electron Spectroscopy and Related Phenomena* **67**, 463 (1994).
- [33] J. Jackson, *Classical Electrodynamics*, 2nd ed. (Wiley, New York, 1975).
- [34] K. Wille, *The Physics of Particle Accelerators* (Oxford University Press, Oxford, 2005).
- [35] R. Carr, *Nuclear Instruments & Methods In Physics Research Section A-Accelerators Spectrometers Detectors And Associated Equipment* **306**, 391 (1991).
- [36] T. Schmidt, W. Bulgheroni, G. Ingold, A. Imhof, B. Jakob, S. Speckert, C. Vollenweider, and Z. D., in *PSI Scientific Report* (PSI, Villigen, 2004), Vol. VII.

Bibliography

- [37] S. I. Fedoseenko, D. V. Vyalikh, I. E. Iossifov, R. Follath, S. A. Gorovikov, R. Puttner, J. S. Schmidt, S. L. Molodtsov, V. K. Adamchuk, W. Gudat, and G. Kaindl, Nuclear Instruments and Methods in Physics Research Section A: Accelerators, Spectrometers, Detectors and Associated Equipment **505**, 718 (2003).
- [38] C. T. Chen and F. Sette, INTERNATIONAL CONFERENCE ON SYNCHROTRON RADIATION INSTRUMENTATION **60**, 1616 (1989).
- [39] Experimental Physics and Industrial Control System: <http://www.aps.anl.gov/epics/>.
- [40] <ftp://ftp.roperscientific.com/Public/Software/Official/WinX32/>.
- [41] synApps <http://www.aps.anl.gov/bcda/synApps/index.php>.
- [42] Python language website <http://www.python.org>.
- [43] EPICS Python binding CaPython and CaChannel http://www-d0online.fnal.gov/www/groups/ctl/epics/epics_python.html.
- [44] Qt Toolkits <http://trolltech.com/products/qt> and its python binding PyQt <http://www.riverbankcomputing.co.uk/pyqt>.
- [45] Scientific Tools for Python <http://www.scipy.org>.
- [46] PyQwt for scientific and engineering plot <http://pyqwt.sourceforge.net>.
- [47] G. Ghiringhelli, M. Matsubara, C. Dallera, F. Fracassi, R. Gusmeroli, A. Piazzalunga, A. Tagliaferri, N. B. Brookes, A. Kotani, and L. Braicovich, Journal Of Physics-Condensed Matter **17**, 5397 (2005).

- [48] H. Ishii, Y. Ishiwata, R. Eguchi, Y. Harada, M. Watanabe, A. Chainani, and S. Shin, *Journal Of The Physical Society Of Japan* **70**, 1813 (2001).
- [49] R. Cowan, *The Theory of Atomic Structure and Spectra* (University of California Press, Berkeley, CA, 1981).
- [50] F. M. F. de Groot, P. Kuiper, and G. A. Sawatzky, *Physical Review B* **57**, 14584 (1998).
- [51] C. Dallera (unpublished).
- [52] P. A. Lindgard, R. J. Birgeneau, J. Alsnielsen, and H. J. Guggenheim, *Journal Of Physics C-Solid State Physics* **8**, 1059 (1975).
- [53] M. T. Hutchings and E. J. Samuelsen, *Phys. Rev. B* **6**, 3447 (1972).
- [54] K. Okada and A. Kotani, *Phys. Rev. B* **65**, 144530 (2002).
- [55] V. I. Anisimov, P. Kuiper, and J. Nordgren, *Phys. Rev. B* **50**, 8257 (1994).
- [56] L.-C. Duda, T. Schmitt, M. Magnuson, J. Forsberg, A. Olsson, J. Nordgren, K. Okada, and A. Kotani, *Physical Review Letters* **96**, 067402 (2006).
- [57] S. Hufner, S. Schmidt, and F. Müller, *Physical Review Letters* **97**, 269701 (2006).
- [58] G. Ghiringhelli, M. Matsubara, C. Dallera, F. Fracassi, A. Tagliaferri, N. B. Brookes, A. Kotani, and L. Braicovich, *Physical Review B* **73**, 035111 (2006).
- [59] S. M. Butorin, J.-H. Guo, M. Magnuson, P. Kuiper, and N. J., *Physical Review B* **54**, 4405 (1996).
- [60] M. Grioni, J. B. Goedkoop, R. Schoorl, F. M. F. de Groot, J. C. Fuggle, F. Schäfers, E. E. Koch, G. Rossi, J.-M. Esteva, and R. C. Karnatak, *Physical Review B* **39**, 1541 (1989).

Bibliography

- [61] G. Ghiringhelli, N. B. Brookes, E. Annese, H. Berger, C. Dallera, M. Grioni, L. Perfetti, A. Tagliaferri, and L. Braicovich, *Physical Review Letters* **92**, 117406 (2004).
- [62] K. Tanaka, Ph.D. thesis, University of Tokyo, 2004.
- [63] J.-H. Guo, S. M. Butorin, N. Wassdahl, J. Nordgren, P. Berastegut, and L.-G. Johansson, *Phys. Rev. B* **61**, 9140 (2000).
- [64] J. P. Hill, C.-C. Kao, W. A. L. Caliebe, M. Matsubara, A. Kotani, J. L. Peng, and R. L. Greene, *Physical Review Letter* **80**, 4967 (1998).
- [65] P. Kuiper, J.-H. Guo, C. S  the, L.-C. Duda, J. Nordgren, J. J. M. Pothuizen, F. M. F. de Groot, and G. A. Sawatzky, *Physical Review Letter* **80**, 5204 (1998).
- [66] M. van Veenendaal, *Physical Review Letters* **96**, 117404 (2006).
- [67] L. Braicovich, G. Ghiringhelli, and J. van den Brink (unpublished).
- [68] J. P. Hill, G. Blumberg, Y.-J. Kim, D. S. Ellis, S. Wakimoto, R. J. Birgeneau, S. Komiya, Y. Ando, B. Liang, R. L. Greene, D. Casa, and T. Gog, *Physical Review Letters* **100**, 097001 (2008).
- [69] J. van den Brink, *Europhysics Letters* **80**, 47003 (2007).
- [70] F. C. Zhang and T. M. Rice, *Phys. Rev. B* **37**, 3759 (1988).
- [71] Y. Harada, K. Okada, R. Eguchi, A. Kotani, H. Takagi, T. Takeuchi, and S. Shin, *Physical Review B* **66**, 165104 (2002).
- [72] L.-C. Duda, J. Downes, C. McGuinness, T. Schmitt, A. Augustsson, K. E. Smith, G. Dhalenne, and A. Revcolevschi, *Physical Review B* **61**, 4186 (2000).

Curriculum Vitae

Personal data

- Name: Xiaoqiang Wang (王晓强)
- Date of Birth: Jun 2, 1977
- Nationality: China
- Marital status: Married, one child

Education

- Ph.D. Physics, Ecole Polytechnique Fédérale de Lausanne, Switzerland, 2008 (Expected)
Thesis title: Resonant Spectroscopies on Strongly Correlated Materials
Supervisor: Marco Grioni
- M.Eng. Electronics and Electrical Engineering, National University of Singapore, Singapore, 2003
Thesis title: Quantum modeling of magnetic tunnel junction
Supervisor: Mansoor bin Abudul Jalil
- B.Eng. Electrical Engineering, Tsinghua University, China, 2000

Schools and conferences

- Swiss Physical Society Annual Meeting, Geneva, March 26-27, 2008. (talk *Spectroscopic Signature of Magnetic Exchange with High Resolution RIXS*)
- Swiss Light Source Symposium: Correlated Oxide Systems, Villigen, March 4, 2008. (talk *High resolution RIXS: a tool to probe low energy excitations in strongly correlated system*)

Curriculum Vitae

- Workshop on X-ray Spectroscopies: theory and experiment, Lausanne, January 30 - February 1, 2008.
- Swiss Physical Society - MaNEP Workshop, Les Diablerets, September 28-30, 2007. (poster *Spectroscopic Signature of Magnetic Exchange with High Resolution RIXS*)
- The 6th PSI Summer School on Condensed Matter Research: Correlated Electron Materials, Zuoz, July 13-19, 2007.
- Neutron and Synchrotron X-ray Diffraction Techniques for Magnetism, Lecture of Troisiem Cycle de la Physique en Suisse Romande held by Luigi Paolasini, Lausanne, 2006.
- Swiss Physical Society - MaNEP Workshop, Les Diablerets, September 26-28, 2005. (poster *High-resolution Soft X-ray and UV RIXS of NiO*)
- The 4th PSI Summer School on Condensed Matter Research: Spectroscopy and Microscopy, Zuoz, August 14-21, 2005. (poster *High-resolution Soft X-ray and UV RIXS of NiO*)

Publications

- "Probing the nature of the Ce 4*f* states in CeX₉Si₄ (X = Ni,Co) by high-energy electron spectroscopies", **X. Wang**, H. Michor, and M. Grioni, Physical Review B 75, 035127 (2007).
- "SAXES, a high resolution spectrometer for resonant x-ray emission in the 400 eV to 1600 eV energy range", G. Ghiringhelli, A. Piazzalunga, C. Dallera, G. Trezzi, L. Braicovich, T. Schmitt, V. N. Strocov, R. Betemps, L. Patthey, **X. Wang**, and M. Grioni, Review of Scientific Instruments 77, 113108 (2006).
- "Localized electronic excitation in NiO studied with resonant inelastic x-ray scattering at the Ni M threshold: evidence of spin flip", S.G. Chiuzbajian, G. Ghiringhelli, C. Dallera, M. Grioni, P. Amann, **X. Wang**, L. Braicovich, and L. Patthey, Physical Review Letters 95, 197402 (2005).
- "Coherent and stochastic charge tunneling in ferromagnetic single electron transistors", M. B. A. Jalil and **X. Wang**, Journal of Applied Physics 95, 1878 (2004).
- "Two-band model of spin-polarized tunneling incorporating discrete charging energy", **X. Wang** and M. B. A. Jalil, Journal of Applied Physics 93, 8056 (2003).

Computing

- Operation System: GNU/Linux (primarily Debian), Mac OS X, MS-Windows
- Language: Assembly, C++, Python, BASH Shell, Labview
- Toolkit: Qt, Tkinter
- Scientific Software: L^AT_EX, Mathematica, Igor Pro, SHADOW

Honors and Awards

- Chinese Government Award for Outstanding Self-financed Students Abroad, 2008.
- Graduate Scholarship, Ecole Polytechnique Federale de Lausanne, 2004-2008.
- Graduate Scholarship, National University of Singapore, 2001-2003.
- Excellent Freshman Award, Tsinghua University, 1996.
- Silver Medal, National Olympic Physics Contest, Hebei Province, 1995.